Characterizing the Microvascular Branching Geometry of the Dual Blood Supply to the Liver with Micro-CT

A DISSERTATION
SUBMITTED TO THE FACULTY OF THE GRADUATE SCHOOL
OF THE UNIVERSITY OF MINNESOTA
BY

Timothy Lee Kline

IN PARTIAL FULFILLMENT OF THE REQUIREMENTS
FOR THE DEGREE OF
Doctor of Philosophy

Erik Leo Ritman, Claudia Neuhauser

July, 2013

Acknowledgements

Foremost, I would like to express my sincerest gratitude to my Advisor, Dr. Erik Ritman who provided guidance and support throughout my PhD study. He gave me the freedom to tackle new questions as they developed and gave me the tools I will need for a life in research. I could not imagine having a better advisor.

I would also like to thank my committee members, Dr. Claudia Neuhauser, Dr. Armando Manduca, Dr. Guillermo Sapiro, and Dr. Emad Ebbini for helping develop my research abilities and focus this project into a solid body of work. Taking the time for discussions and critiquing my work has been very helpful and is greatly appreciated.

My colleagues in the Physiological Imaging Research Lab are some of the most helpful people a person could ever hope for. To Andrew Vercnocke, a great man to discuss video games, movies, and image analysis tools, thanks for all you do. In particular, Andrew helped with performing image reconstructions. To Jill Anderson for being such an understanding supervisor, who I always feel comfortable discussing anything on my mind with, a big warm thank you. Jill helped with specimen preparations. To Steve Jorgenson for always stepping up to the plate to get things done as best as possible, thank you so much. Steve performed scanning of specimens both utilizing the in-house micro-CT scanners he setup himself, and took specimens to the National Synchrotron Light Source at Brookhaven National Labs. Also, to Delories Darling for helping get the research into the hands of the world, and being a friendly face to discuss both work and outside work events with, I am truly grateful.

In addition, Dr. Mair Zamir for his great contributions and discussions regarding studying the geometry of microvasculature. I hope we can work together in the future. Also, Bruce Knudsen who helped develop the dual-injection specimen preparation method for the liver, I thank you a great deal.

To my Mother and Father, Rosemary and Robert Kline for giving me the confidence to pursue any challenge that I see. They instilled in me the belief that I can do anything. Truly, this is the attribute about myself that I am the most proud of. And to my siblings, Tara and Tiffany for being the greatest people to grow up with - who are always there when I need them. Love you all!

To Aiden, the best son a father could hope for. Whether we are discussing the cosmos or video games, playing catch or going fishing, watching Monty Python or The Simpsons - I sincerely enjoy every second with you.

Finally, to the brave animals who contributed to this dissertation, and to the trees who lent the surface upon which I laid my pen, thank you for being meritorious helpers in humanities pursuit for deeper understanding.

Dedication

This Dissertation is dedicated to my wife, Aimee Rose Kline. She is the most supportive person in this world, pushing me to pursue anything that I express interest in. I have taken graduate courses for the past 7 years, requiring countless hours of travel, study, and stress. You are a truly wonderful and completely understanding person. So this work is for you Aimee - I am looking forward to spending all my days with you. I love you.

Abstract

Microvascular branching geometries determine the efficacy of the transport of nutrients and metabolic products to and from tissues in large-bodied organisms. The general 'plan' is that an artery supplies oxygen, nutrients, and hormones to the tissue and a vein removes metabolic products from that tissue. The blood flow to the organ is controlled by the metabolic demand of the organ by a feedback mechanism controlling the arterial lumen diameter. The liver differs from other organs by having two vascular systems delivering its blood - the hepatic artery and the portal vein. The hepatic artery supplies the oxygen needed by liver cells, and the portal vein delivers the molecules absorbed by the gut which need to be processed by the liver tissue for use by other organs in the body. However, how the hepatic artery and portal vein interact is not fully understood in terms of how their relative flows are adjusted, either passively and/or actively, to meet the needs of the liver tissue. This dissertation explores the hypothesis that the hepatic artery's blood mixes with the portal vein's proximal to the hepatic sinusoids (where their mixing is traditionally thought to occur). This is performed utilizing micro-CT to image rat liver lobes injected with a contrast polymer. During the process of exploring this hypothesis, a number of image analysis tools needed to be developed. For one, understanding the level of accuracy by which geometrical measurements can be made by micro-CT is very important because vascular resistance to flow is proportional to the interbranch segment length, as well as inversely proportional to the fourth power of the lumen diameter. Moreover, a single vessel tree contained in a micro-CT image has hundreds, if not thousands of individual interbranch segments and knowledge of the interconnectivity relationship between the segments is important for modeling such properties as pressure distributions and relative blood flow rates. For these reasons, the development of automated measurement methods to measure the length and diameter of interbranch segments and extract the hierarchical structure of vascular trees was performed. These methods were then compared to a gold-standard measurement (obtained by measuring the lengths and diameters of interbranch segments of a microvascular cast by 'hand' under a microscope) to understand the level of accuracy obtainable by micro-CT. Having successfully developed accurate automated

measurement algorithms (thereby replacing the time-consuming gold standard measurement method), the algorithms were then used to compare and validate other algorithmic approaches, particularly those that quickly extract geometrical information regarding a vascular bed composed of many vessel trees within a micro-CT image. Because the hepatic artery and portal vein are in close proximity to one another as they distribute throughout the liver, the development of a special segmentation method was needed to allow separation of these concomitant vessel systems that may have 'false' connections resulting from blurring of the micro-CT image. Finally, an anatomic study of the vasculature of the liver was performed which offered insight into the interaction between the hepatic artery and portal vein. In the case of specimens where only the portal vein was injected with contrast, only the portal vein was opacified, whereas in hepatic artery injections, both the hepatic artery and portal vein were opacified. Also, when different contrast agents were injected into the hepatic artery and the portal vein, the hepatic artery's contrast agent was observed to be mixed in with the different contrast injected into the portal vein. In addition, in high-resolution scans (5μm cubic voxels) anatomic evidence for hepatic arteriolo-portal venular shunts occurring between the hepatic artery and portal vein branches were found. Simulations were performed in order to rule out the possibility of the observed shunts being artifacts caused by image blurring. Thus, mixing of the hepatic artery and portal vein can occur proximal to the sinusoidal level, and hepatic arteriolo-portal venular shunts may function as a one-way valve-like mechanism, allowing flow only from the hepatic artery to the portal vein (and not the other way around).

Contents

Acknowledgements **i**

Dedication **iii**

Abstract **iv**

List of Tables **x**

List of Figures **xi**

1 Introduction **1**

2 Vascular Physiology of the Liver **6**

2.1 OVERVIEW 6

2.2 SHUNTS 7

3 Studying Microcirculation with Micro-CT **13**

3.1 INTRODUCTION 13

3.2 MICRO-COMPUTED TOMOGRAPHY 14

3.2.1 History 14

3.2.2 Theory 17

3.2.3 Conventional Micro-CT System 17

3.2.4 Image Reconstruction 22

3.2.5 Image Quality 22

3.2.6 Multi-Modality Imaging 24

3.3 SPECIMEN/ANIMAL PREPARATION 24

3.3.1 Ex Vivo - Casting . . . 25
3.3.2 In Situ - Contrast Agent Enhancement . . . 26
3.3.3 In Vivo . . . 27
3.4 IMAGE ANALYSIS . . . 28
3.4.1 Segmentation . . . 29
3.4.2 Centerline Extraction . . . 31
3.4.3 Measurements . . . 31
3.4.4 Erode/dilate analysis . . . 32
3.4.5 Modeling . . . 34

4 Accuracy of Microvascular Measurements Obtained from Micro-CT Images 35
4.1 INTRODUCTION . . . 35
4.2 METHODS . . . 38
4.2.1 Gold-Standard . . . 38
4.2.2 Micro-CT Imaging . . . 40
4.2.3 Segmentation . . . 42
4.2.4 Centerline Extraction . . . 42
4.2.5 Vessel Branch Measurements . . . 46
4.2.6 Compensating for Micro-CT MTF . . . 48
4.3 RESULTS . . . 51
4.4 DISCUSSION . . . 59
4.5 CONCLUSIONS . . . 63

5 Comparison of Measurement Strategies for Vascular Characterization 65
5.1 INTRODUCTION . . . 65
5.2 METHODS . . . 66
5.2.1 Sample preparation and micro-CT scanning . . . 66
5.2.2 Erode/dilate analysis . . . 67
5.2.3 Model vascular tree . . . 68
5.2.4 Individual tree segmentation . . . 71
5.2.5 Direct measurements . . . 72
5.3 RESULTS . . . 74

5.4 CONCLUSIONS 77

6 Relating Function to Branching Geometry: A Micro-CT Study of the Hepatic Artery, Portal Vein, and Biliary Tree 78

6.1 INTRODUCTION 78
6.2 METHODS 80
6.2.1 Specimens 80
6.2.2 Micro-CT Imaging 81
6.2.3 Segmentation 81
6.2.4 Vascular Tree Measurements 82
6.2.5 Characterization of Branching Geometry 82
6.3 RESULTS 84
6.4 DISCUSSION 89

7 Automated Segmentation Method for Separating Concomitant Arteries from Veins in 3D Micro-CT Images 95

7.1 INTRODUCTION 95
7.2 BACKGROUND 96
7.3 METHODS 97
7.3.1 Specimen preparation 97
7.3.2 Micro-CT Imaging 97
7.3.3 Segmentation method 98
7.4 RESULTS 104
7.5 DISCUSSION 108
7.6 CONCLUSIONS 110

8 Anatomy of Hepatic Arteriolo-Portal Venular Shunts Evaluated by 3D Micro-CT Imaging 111

8.1 INTRODUCTION 111
8.2 METHODS 112
8.2.1 Specimen preparation 112
8.2.2 Micro-CT Imaging 113
8.2.3 Blurring Simulation 115

8.3 RESULTS 117
8.4 DISCUSSION 124
8.5 CONCLUSION 125

9 Conclusion **126**

References **129**

Appendix A. Permissions **144**

List of Tables

5.1 Least-squares fitting results for erode/dilate measurement method validation 75

List of Figures

2.1 Illustration of vasculature of the liver 8
2.2 Dissection of rat 9
2.3 Illustration of liver lobules 10
2.4 Prior experimental evidence for hepatic arteriolo-portal venular shunts . 11
3.1 Illustration of the scales needed to image different sized specimens . . . 15
3.2 Graphical illustration of yearly rise in micro-CT related publications . . 16
3.3 Illustration and photograph of a micro-CT imaging system with a rotating specimen geometry 19
3.4 Maximum intensity projection of the micro-CT data from the portal vein of a rat 20
3.5 Illustration and photograph of a micro-CT imaging system with a rotating gantry geometry 21
3.6 Vascular cast of a whole rabbit kidney imaged by micro-CT 26
3.7 Micro-CT image data of the vascular bed of a rat heart, which was filled with a contrast agent and imaged in situ 27
3.8 Micro-CT image data of a corrosion cast of a human coronary artery . . 30
4.1 Microscope digital photograph and micro-CT image of human coronary artery cast 40
4.2 J,K notation used for labeling the vessel segments in a tree structure . . 41
4.3 Line profile of varying diameter branch segments illustrating image blurring resulting from non-ideal modulation transfer function of micro-CT scanners 49
4.4 An illustration of the image blurring process 49

4.5 A plot of the theoretical gray scale values' dependence on vessel diameter for three different scanner blurring function widths 50
4.6 Extracted centerline shown superimposed on the volume rendered display of vascular tree, specimen *h61* 52
4.7 Zoomed-in views of the vessel tree displayed semi-transparently, with the corresponding extracted centerline 53
4.8 Extracted centerline shown superimposed on the volume rendered display of vascular tree cast, specimen *r14* 54
4.9 Regression plots for individual branch segments diameter and length measurements of specimen by the micro-CT and optical measurement methods 55
4.10 Regression plots for individual branch segments diameter and length measurements of specimen *r14* 56
4.11 Bland-Altman method comparison analysis for both interbranch segment diameter and length of specimen *h61* 58
4.12 The result of applying morphological thinning as well as mesh contraction methods to *h61* in order to extract vessel centerlines 60
5.1 Computer generated display of a volume rendered 3D micro-CT image of the microvasculature within porcine myocardium 66
5.2 Radius increments of a hypothetical Murray-type tree 69
5.3 The vessel volume distribution calculated for the Murray-type tree, binned according to the erode/dilate analysis method 70
5.4 A schematic representation of the expected impact of the erode/dilate analysis when microsphere embolization blocks a proportion of vessel segments below the microsphere diameter 72
5.5 Volume rendering of 3D image data of centerline as extracted from an example vessel tree 73
5.6 Results for non-embolized sample for erode/dilate measurement method validation 75
5.7 Comparison of embolized to non-embolized specimens for entire biopsy studied by erode/dilate method, individual tree studied by erode/dilate method, and individual tree studied by direct measurements of interbranch segments 76

6.1 Illustration of liver vasculature 79
6.2 Average vessel segment lengths at different generations of the hepatic artery, portal vein, and biliary tree specimens 85
6.3 Non-dimensional diameters of the larger branch segments asymmetry ratio in the tree structure of the hepatic artery, the portal vein, and the biliary tree specimens 86
6.4 Non-dimensional diameters of the smaller branch segments asymmetry ratio in the tree structure of the hepatic artery, the portal vein, and the biliary tree specimens 87
6.5 Area ratios at arterial bifurcations vs. the asymmetry ratios in the tree structures of the hepatic artery, the portal vein, and the biliary tree specimens 88
6.6 Determination of the junction exponent 90
6.7 Theoretical larger branch non-dimensional diameter with imposed 5%, 10% , 20% variability, and 40% variability 91
7.1 Illustration of concomitant vessel blurring 99
7.2 Concomitant vessel segmentation approach 101
7.3 Medialness measure 103
7.4 Illustration of concomitant vessel segmentation in 2D 105
7.5 Image data sets used to compare dimensional analysis of the vascular trees 106
7.6 Plots of the total lumenal volume of all vessel segments within the selected lumen diameter range 107
7.7 Segmentation method applied to micro-CT scans of two portions of different rat lungs and mouse kidneys 109
8.1 Overview of specimen preparation and subsequent scanning leading to identification of hepatic arteriolo-portal venular shunts 113
8.2 High-resolution scan of sub-volume of rat liver caudate lobe. 114
8.3 Illustration of vessel blurring for 5μm cubic voxels 116
8.4 Observation of potential one-way valve-like mechanism of hepatic arteriolo-portal venular shunts 117
8.5 Microfil injected into the hepatic artery showing up in the portal vein . 118

8.6 Illustration of one-way valve-like mechanism of hepatic arteriolo-portal venular shunts 119
8.7 Examples of common spacing between the contrast enhanced vessel lumens of the hepatic artery and portal vein 119
8.8 Examples of hepatic arteriolo-portal venular shunts 120
8.9 Volume rendering of hepatic arteriolo-portal venular shunts 121
8.10 Comparison of simulated hepatic artery line profile with measured profiles near shunt location 121
8.11 Simulation of varying spacing between hepatic artery and portal vein compared to measured result for observed shunt 122
8.12 Comparison of the line profile generated across an observed shunt, with a simulation for the case that the hepatic artery and portal vein lumens are connected by a shunt 123
A.1 Permission to reproduce *Microcirculation Imaging* book chapter 145
A.2 Permission to reproduce *Annals of Biomedical Engineering* manuscript . 146
A.3 Permission to reproduce *SPIE* manuscript 147
A.4 Permission to reproduce *Cells Tissues Organs* manuscript 148

Chapter 1

Introduction

The exploration of a functioning complex system, a system which has distributed structure in which each component potentially impacts the function of all other components, motivates this dissertation. A vascular tree is a complex structure in which each interbranching segment has a potential effect on the function (i.e., blood flow) throughout the rest of the tree. The effect can be both downstream, via the serial vascular resistance pathway (where the total resistance is the sum of the serial resistances), as well as on other branches via the parallel vascular resistance (where the reciprocal of the total resistance is the sum of the reciprocal parallel resistances). Perhaps one of the most interesting examples, in terms of studying vascular structure-to-function relationships, is offered by the dual blood supply of the liver (delivered by both the hepatic artery and the portal vein). To this end, there still exist many unanswered questions regarding how the hepatic artery and portal vein not only regulate themselves, but also respond to changes in their parallel concomitant vessel system. This dissertation proposes to study the microvasculature geometry of the liver, in particular, the question of how the dual blood supplies of the liver interact functionally.

In general, questions related to vasculature have been studied for hundreds of years [1, 2]. Understanding the design rules of nature that vasculature follows is an area of basic physiological research which has found heightened interest in the last century. Many models have been developed [3, 4] and many experimental procedures have been used [5, 6, 7] to measure various properties of vascular geometry, such as interbranch segment lengths and diameters, the angle at which the vessel system bifurcates, and

the interconnectivity relationship of vascular beds. Although the overall structure-to-function relationship of vascular trees has been explored by many investigators in the past century [8, 9, 10], they did not have the full 3D structural data needed to be sure that their model was universally valid, hence most extrapolated from dimensional data obtained from microscope images of vasculature in membranes or on surfaces of organs or resorted to modeling to extend the 2D data to explore the 3D implications.

Early studies involved two-dimensional analysis by use of vessels present at the surface of a tissue or those present in histological sections (which could be sectioned down to a few micrometers thick). With the advent of vascular casting methods in the 1970's, surrounding tissue could be dissolved while retaining the vasculature. This allowed analysis to be performed in three-dimensions using high powered optical microscopes [11] and other variants such as scanning electron microscopes [12]. However, such methods as serial section histology, confocal microscopy, and scanning electron microscopy all are very limited in providing the 3D anatomy of an entire intact vascular tree within an organ. Thus, early attempts assumed that the terminal vasculature was identical throughout the organ [9] - something that made their subsequent analysis of entire vascular trees tractable. Micro-Computed Tomography (micro-CT) has emerged as a powerful modality for vascular exploration in intact small animals [13, 14, 15, 16, 17, 18] and in corrosion casts and/or biopsies of large animal specimens [19, 20, 21, 22]. This is due to the fact that micro-CT provides high resolution 3D volumetric data of relatively large tissue samples, and in the case of intact organs, contrast agents (such as polymers which set in the vascular lumens after filling the entire vascular tree) can be used to distinguish vessels from the surrounding tissue. Those data are suitable for analysis, quantification, validation and visualization of vasculature.

The hierarchical structure and branching geometry of vessel segments greater than 20 μm in diameter, called distributive vasculature, has been well studied [9, 6, 11, 23, 24]. In addition, micro-CT imaging systems have been used to study distributing vessel systems within organs such as the liver [25], kidney [26], and heart [19]. However, problems still exist with regard to image analysis measurement strategies and studies are possible regarding vascular geometry in various states of health and disease, as well as the structure-to-function relationship of vasculature. Finally, exchange vasculature at the terminal arteriolar (15 μm), capillary (5 μm), and venular level (15 μm) has yet to

be characterized to the same extent in terms of its branching geometry and geometric interrelationships between these vessel segments. Information about geometrical dimensions and the interconnectivity relationships for arterioles, capillaries and venules is available for only a limited volume and limited number of tissues [5, 27]. In these previous studies, the use of projection data or surface renditions obtained by scanning electron microscopy rather than 3D images makes the representative nature of the derived vascular dimensions questionable. Therefore, our knowledge of microvasculature is based (to a large extent) on theoretical models which involve simplifying assumptions [28, 29].

The geometry of exchange vasculature is important for understanding arteriolar/ venular communication possibilities such as (i) the role of counter-current exchange between terminal arterioles and venules [30], (ii) the effect that electrical conduction may play via the microvascular endothelium [31], and (iii) whether fluid dynamic "switching" occurs when two vascular trees feed into a single capillary bed - such as might occur when the portal vein and hepatic artery feed into the same hepatic sinusoids.

Thus, a method to characterize the exchange vasculature requires high spatial resolution three-dimensional information within a large tissue volume, which is used in conjunction with a highly accurate measurement method. With voxel resolutions down to 1-2 μm, modern day X-ray imaging systems, such as synchrotron-based micro-computed tomography (micro-CT), offer an excellent opportunity to study intact biological tissues, in three-dimensions, at very fine scales [14]. Moreover, being in digital form, micro-CT is also directly accessible to automated analysis of the anatomic information, a factor that gets around the logistic roadblock of other methods. However, the barriers to performing such an analysis have been the need for accurate measurement strategies, and tools for exploring the complex microvascular geometry. Another limitation is that micro-CT scanners generate images that are blurred to some extent, and this has an incremental impact the smaller the diameter of the vascular branch segment. Hence, this problem has to be addressed because the vascular resistance is affected by the reciprocal of the fourth power of the lumen diameter (Poiseuille's law [32]) and the impact of the blurring is preferential in the most distal segments. As the mechanism of blurring is fairly well characterized by the modulation transfer function (MTF) of the micro-CT system, this blurring can by largely overcome, as illustrated in **Chapter 4**.

The liver differs from other organs by having two vessel systems which deliver blood to it [33]. The classic hypothesis is that the blood from the portal vein and hepatic artery mix as they enter the hepatic sinusoids (capillaries). Early studies of the liver's dual blood supply proposed two different and contrasting hypotheses: (i) the hepatic artery and portal vein's flows do not influence each other [34], or (ii) that a reciprocal and compensatory relation exists between changes in their flow [35]. In 1965, a definite interrelationship between the two was identified by observing that the hepatic arterial flow increased when portal vein flow was decreased [36]. This mechanism was later termed the hepatic arterial buffer response [37].

More recently, a study by Richter et al. [38] offered not only further support for the hepatic arterial buffer response, but also evidence for the existence of shunts between the hepatic artery and portal vein. This was supported by noting that if portal vein flow was reduced to $\sim$10% its normal flow immediately downstream of the tourniquet, the blood flow in the terminal venules had returned to nearly 70% of their normal value. Thus, these shunts would need to occur upstream (proximal) to the hepatic lobule's sinusoids allowing flow from the hepatic artery into the portal vein. An implication is that these hepatic arteriolo-portal venular shunts could offer a means of communication between the two vessel systems where reduction in portal vein flow is compensated for (and 'felt') by the hepatic artery.

Nevertheless, the existence of hepatic shunts between the portal vein and hepatic artery is still debated in the current literature. Knowledge of intrahepatic shunts (shunts between the portal vein and hepatic vein) have been the focus of a number of studies, where their existence has been both confirmed at diameters up to 80-90μm [39], as well as ruled out for $>$15μm diameter shunts [40] in rat liver specimens. No evidence for shunts between the hepatic artery and hepatic vein have been published. In addition, hepatic arteriolo-portal venular shunts (shunts between the hepatic artery and portal vein - those studied in this dissertation) have been both supported [41], and rejected [42].

This dissertation begins with a discussion of the physiology of the liver (**Chapter 2**), including its function, and current understanding of both its vascular and microvascular geometry. Prior literature related to hepatic arteriolo-portal venular shunts is highlighted. Then, an overview of utilizing micro-CT to quantitatively characterize

geometry of microvasculature is given in **Chapter 3**. This includes an overview of specimen preparation methods and analysis techniques. Next, the accuracy by which geometrical measurements can be made by micro-CT is presented (**Chapter 4**), which includes the development of automated measurement methods to accurately measure the length and diameter of interbranch segments and extract the hierarchical structure of the vasculature tree. In **Chapter 5** these methods are then used to compare and validate other measurement strategies, particularly those that can quickly extract measurements for many vessel trees contained in a single micro-CT image. In addition, how the data generated by the automated methods can be used to investigate the geometric properties of vascular structures, in particular with regard to the model derived by Murray[8] is given in **Chapter 6**. Here, the vascular branching geometry of the hepatic artery, portal vein (as well as the biliary tree) are explored. In **Chapter 7**, a specimen preparation method that allows all of the vasculature of the liver to be filled with contrast is discussed. In addition, the development of a segmentation method to not only separate the vessels from the surrounding tissue, but also separate the concomitant vessel systems from one another (which was necessary for these images) is presented in the same chapter. Finally, a high-resolution 3D anatomic study of liver vasculature was performed (**Chapter 8**) which offers insight into the anatomic aspects of hemodynamic interaction between the hepatic artery and portal vein. This dissertation supports the existence of hepatic arteriolo-portal venous shunts in normal rat liver specimens. A concluding chapter (**Chapter 9**) discusses the implications of this dissertation, including its limitations, and offers insights into directions for possible future research investigations.

Chapter 2

Vascular Physiology of the Liver

2.1 OVERVIEW

The liver, a wedge-shaped organ, is the largest gland in the body[43]. It is ∼4% of an adult rat's total body weight (∼300g), receiving around 12 mL of blood per minute[44]. As a reference, an average human's liver is around 2.5% of their total body weight and hepatic blood flow is around 1500 mL/min[33]. The liver has two surfaces, the 'diaphragmatic surface' and the 'visceral surface'. The diaphragmatic surface is convex and is moulded to the undersurface of the diaphragm. The porta hepatis, a deep fissure on the visceral surface, is where the hepatic artery and portal vein enter, and the biliary tree exits the liver.

Shown in Figure 6.1 is a diagram of the relevant liver vasculature for this study. Oxygenated blood to the liver is provided by the hepatic artery which is a branch off of the coeliac artery, which in turn is a direct branch off of the aorta. Upon entering the liver at the porta hepatis, the hepatic artery divides into right and left branches. The hepatic artery supplies ∼25% of the liver's total blood flow, while the remaining ∼75% is supplied by the portal vein. The portal vein is the upward continuation of the superior mesenteric vein. The portal vein carries venous blood to the liver; blood which contains the products of digestion which have been absorbed from the alimentary canal and are to be metabolized by liver cells. Like the hepatic artery, the portal vein also divides into right and left branches within the porta hepatis. Shown in Figure 2.2 is a

dissection of one of the rats, showing relevant anatomy.

The hepatic artery and portal vein follow essentially the same anatomical paths within the liver. The structural unit of the liver is the hepatic lobule. The hepatic lobules are a roughly hexagonal arrangement of hepatocyte plates, which are separated by intervening sinusoids (small blood vessels similar to capillaries but with a fenestrated endothelium) which radiate outward from a central hepatic vein. The portal triads (hepatic artery, portal vein, and biliary tree) are located at the vertices of each hexagon. A schematic depiction is given in Figure 2.3. A central hepatic vein branch drains each lobule, which is carried away from the liver to the inferior vena cava. This traditional view of the hepatic lobule proposes the blood of the hepatic artery and portal vein first mix at the sinusoidal level. However, the existance of hepatic arteriolo-portal venular shunts would alter this traditional view of the hepatic lobule, that the hepatic artery's and portal vein's blood mixes proximal to the sinusoidal level.

The liver is a relatively homogeneous organ possessing fewer anatomical constraints on vascular branching than, for instance, the constraints imposed on the coronary arteries and veins, with their different epicardial and intramyocardial environments, as well as on the pulmonary arteries and veins which are constrained by the bronchi. In addition, heart and lungs cyclically deform, meaning that their shape drastically changes within a short amount of time. Thus, vascular image 'snapshots' may not represent the underlying vascular geometry accurately. Therefore, liver vasculature offers an excellent opportunity to study the relationship between branching geometry and the functional roles of vasculature. In particular, the hepatic artery and portal vein which are in close proximity to one another, and follow essentially the same branching paths.

2.2 SHUNTS

The existance of hepatic arteriolo-portal venular shunts would partially answer the question of how the dual blood supply of the liver (delivered by the hepatic artery and portal vein) interact. Early studies of the liver's dual blood supply proposed two different and contrasting hypotheses: (i) the hepatic artery and portal vein's flows do not influence each other [34], or (ii) that a reciprocal and compensatory relation exists

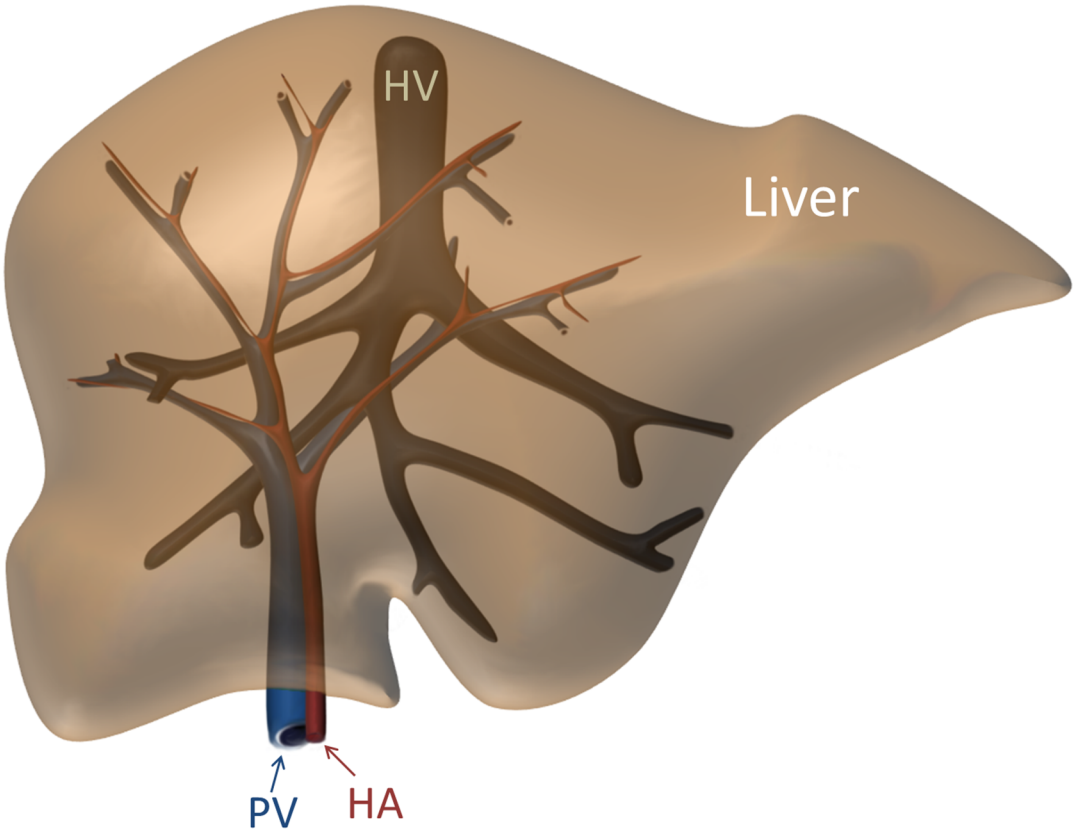

Figure 2.1: Illustration of the vasculature of the liver. The hepatic artery (HA) and portal vein (PV) follow roughly the same anatomical paths throughout the liver, entering the liver through the porta hepatis. The blood pressure in the hepatic artery is approximately ten times that of the portal vein upon entering the liver. In addition, the hepatic artery has a much smaller diameter than that of the portal vein when comparing concomitant vessel branch segments. The hepatic vein (HV) drains the liver.

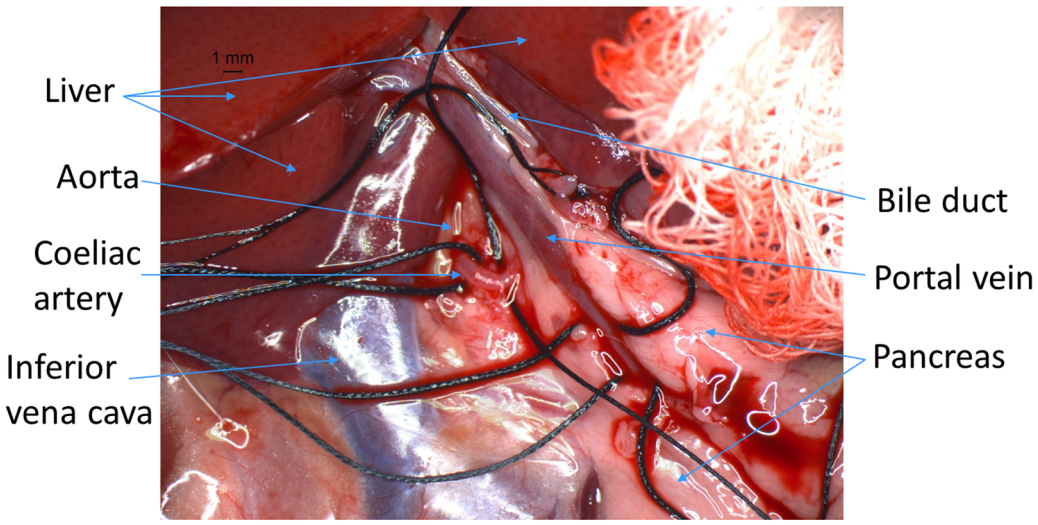

Figure 2.2: Dissection of one of the rat specimens, highlighting relevant anatomical structures.

between changes in their flow [35]. In 1965, a definite interrelationship between the two was identified by observing that the hepatic arterial flow increased when portal vein flow was decreased [36]. This mechanism was later termed the hepatic arterial buffer response [37].

More recently, a study by Richter et al. [38] offered not only further support for the hepatic arterial buffer response, but also evidence for the existance of shunts between the hepatic artery and portal vein as outlined in Figure 2.4. This was supported by noting that if portal vein flow was reduced to ∼10% its normal flow immediately downstream of the tourniquet, the blood flow in the terminal venules had returned to nearly 70% of its normal value. Thus, these shunts would need to occur upstream to the hepatic lobule's sinusoids allowing flow from the hepatic artery into the portal vein. An implication is that these hepatic arteriolo-portal venular shunts could offer a means of communication between the two vessel systems where reduction in portal vein flow is compensated for by the hepatic artery.

Nevertheless, the existance of hepatic shunts between the portal vein and hepatic artery is still debated in the current literature. Knowledge of intrahepatic shunts (shunts between the portal vein and hepatic vein) have been the focus of a number of studies,

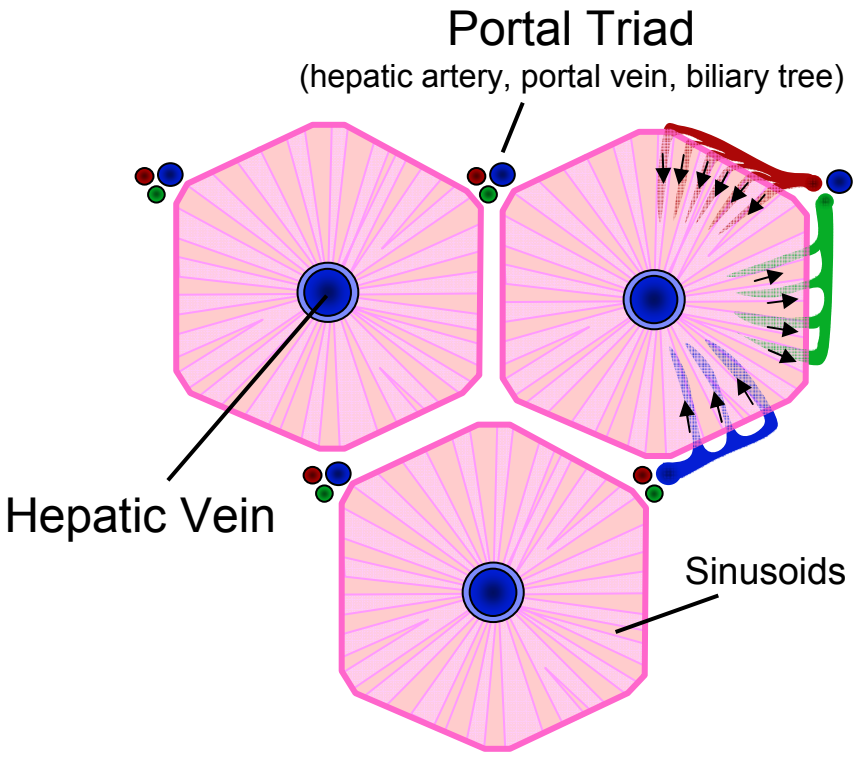

Figure 2.3: The liver lobules are a roughly hexagonal arrangement of hepatocyte plates which are separated by intervening sinusoids (small blood vessels similar to capillaries but with a fenestrated endothelium) which radiate outward from a central vein. The portal triads are located at the vertices of each hexagon. The different functions of the terminal branches of the hepatic artery, portal vein, and biliary tree occur within each lobule. A central vein drains each lobule, which is carried to the hepatic vein away from the liver. From [45].

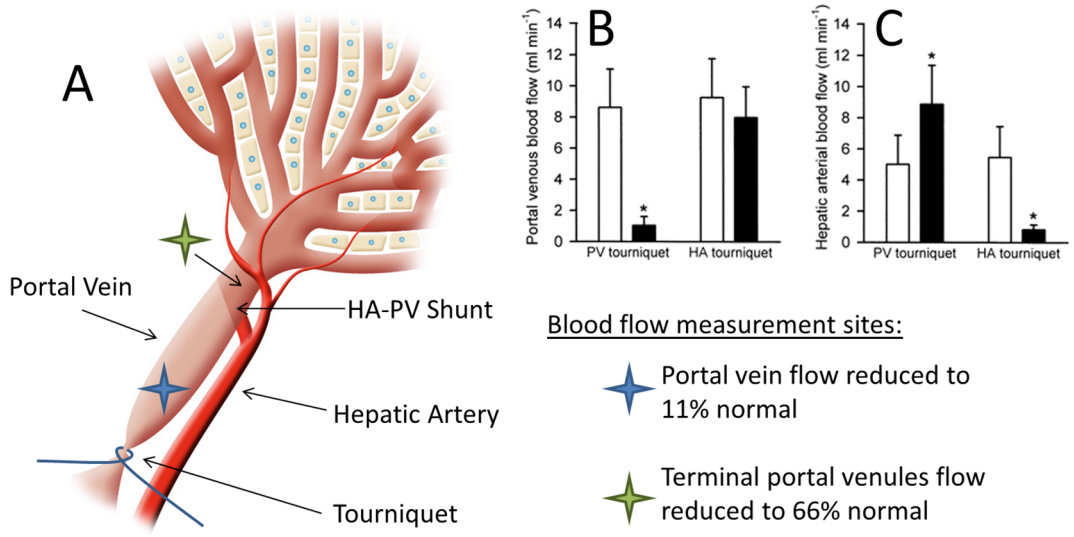

Figure 2.4: Prior experimental evidence for hepatic arteriolo-portal venular shunts. **Panel A:** A tourniquet was placed on either the portal vein or the hepatic artery to restrict blood flow. **Panel B:** Measurement of portal vein flow. **Panel C:** Measurement of hepatic artery flow. Applying a tourniquet to the portal vein resulted in a statistically significant decrease in portal vein flow. Likewise, application of a tourniquet to the hepatic artery resulted in a stastically significant decrease to hepatic arterial flow. The important result is that application of a portal vein tourniquet resulted in a stastically significant increase in hepatic arterial flow (evidence of hepatic artery buffer response). In addition, measurement of portal vein flow right after the tourniquet location showed a reduction to 11% normal value, whereas measurement near terminal portal vein branches showed flow had been restored to 66% normal value. This is evidence for hepatic arteriolo-portal venular shunts as blood from the hepatic artery must be able to mix with the portal vein proximal to the sinusoids (as traditionally thought). This figure was modified from [38].

where their existance has been both confirmed at diameters up to 80-90μm [39], as well as ruled out for >15μm diameter shunts [40] in rat liver specimens. In addition, hepatic arteriolo-portal venular shunts (shunts between the hepatic artery and portal vein - those studied in this dissertation) have been both supported [41], and rejected [42]. Therefore, utilizing micro-CT to obtain 3D anatomic evidence for hepatic arteriolo-portal venular shunts is the overarching goal of this dissertation.

Chapter 3

Studying Microcirculation with Micro-CT

3.1 INTRODUCTION

Micro-Computed Tomography (micro-CT) has emerged as a powerful modality for vascular exploration in intact small animals [14, 15, 18, 16] and in corrosion casts and/or biopsies of larger animal specimens [20, 22]. This is due to the fact that micro-CT provides high resolution 3D volumetric data. The data are suitable for analysis, quantification, validation, and visualization of vasculature. As an example, quantitative 3D imaging studies of induced or implanted disease models can be studied [46, 47], and screening for anatomical abnormalities and detection and quantification of anatomical changes in live animals (or tissue samples) can be characterized [7]. The study of vascular development (such as mechanisms of neovascularization and evaluating pro and anti-angiogenic strategies) requires a complete and accurate characterization of the microvasculature. Thus micro-CT, which is able to quantify anatomical information in three-dimensions, non-destructively, at a very high spatial resolution, nonetheless limited in its ability to convey metabolic and other cellular functions as compared to other

This chapter was modified from the original book chapter: **TL Kline and EL Ritman. Studying microcirculation with micro-CT. In M. Leahy, editor, *Microcirculation Imaging*, chapter 14, pages 313-348. Wiley-VCH, 2012.** and reproduced by permission of the publisher: Wiley-VCH (see **Chapter A**)

methods such as radionuclide imaging. However, such methods suffer from poor spatial resolutions, and thus the information from multiple imaging methods can be used to complete a fully comprehensive analysis.

3.2 MICRO-COMPUTED TOMOGRAPHY

3.2.1 History

Computed tomography (CT) provides three-dimensional images of the internal structure of an object [48]. The mathematical foundation of this imaging technique was published by Johann Radon, who in 1917 proved that an object with n-components can be reconstructed from its (n-1)-dimensional projections [49]. The mathematics for CT image reconstruction was not fully developed until the 1960's when Allan MacLeod Cormack presented the possibilities Radon's mathematical formulation had for radiological applications [50]. Nearly a decade later, Godfrey Newbold Hounsfield patented the concept of a clinically useful CT scanner [51, 52], and soon after, successfully built one [53]. For their work, Cormack and Hounsfield shared the Nobel Prize in Medicine in 1979. CT scanners soon became, and have remained, an important diagnostic tool for non-invasively imaging three-dimensional sections of the human body. Present day multi-slice CT scanners can image vascular trees by virtue of injected contrast agents. The smallest vessels imaged are about 1mm in diameter. In general, the term microvasculature is used to describe vessel segments less than 1mm in diameter, on down to the 5μm diameter capillaries.

Since their clinical inception in 1971, CT scanners quickly became and have remained, an important diagnostic tool for non-invasively imaging three-dimensional sections of the human body. Present day multi-slice CT scanners can image vascular trees by virtue of injected contrast agents. The smallest vessels imaged are about 1 mm in diameter. In general, the term microvasculature is used to describe vessel segments less than 1 mm in diameter, on down to the 5 μm diameter capillaries. Miniaturized versions of clinical scanners are termed mini-CT scanners. These scanners are capable of imaging entire small animal specimens (down to about 50μm on a side cubic voxels). To image on down to the cellular level (i.e., <10μm voxel resolution) is achievable by modern micro-CT scanners. Micro-CT scanners are capable of imaging isolated specimens

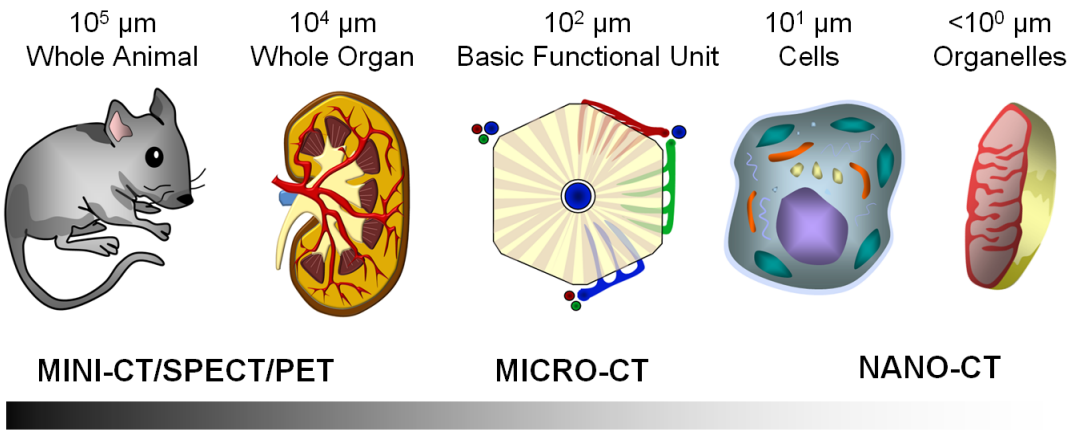

Figure 3.1: Illustration of the scales needed to image different sized specimens along with the corresponding CT tomographic scanners used for studying the orders-of-magnitude difference of specimen size. From left to right the illustrations represent a small animal specimen (mouse), a whole organ specimen (kidney), the basic functional unit of the liver (lobule), a generic cell, and an organelle (mitochondrion). From [54].

down to the cellular level. The highest resolution scanners available today are known as nano-CT scanners and are able to image at and below the cellular level. Figure 3.2 illustrates the types range of scales of specimens imaged by the various scanners.

Improving scanner resolution was initially driven by the bone research field. Bone is naturally well suited to CT imaging due to its large contrast from soft tissue. The first custom-made micro-CT scanners were built in the early 1980's, mainly for evaluating the three-dimensional micro-structure of bone trabeculae [55]. In the early 1990's, the first commercially available micro-CT scanners became available and ever since, the capabilities of micro-CT imaging methods and the range of research investigations, have been steadily growing. Shown in Figure A.4 is the result of a query of the PubMed database for publications related to micro-CT. The number of publications has seen an exponential growth in recent years. However, the study of microvasculature by micro-CT imaging comprises a small portion of the total research investigations (approximately 16%), while bone related research makes up over half (approximately 58%).

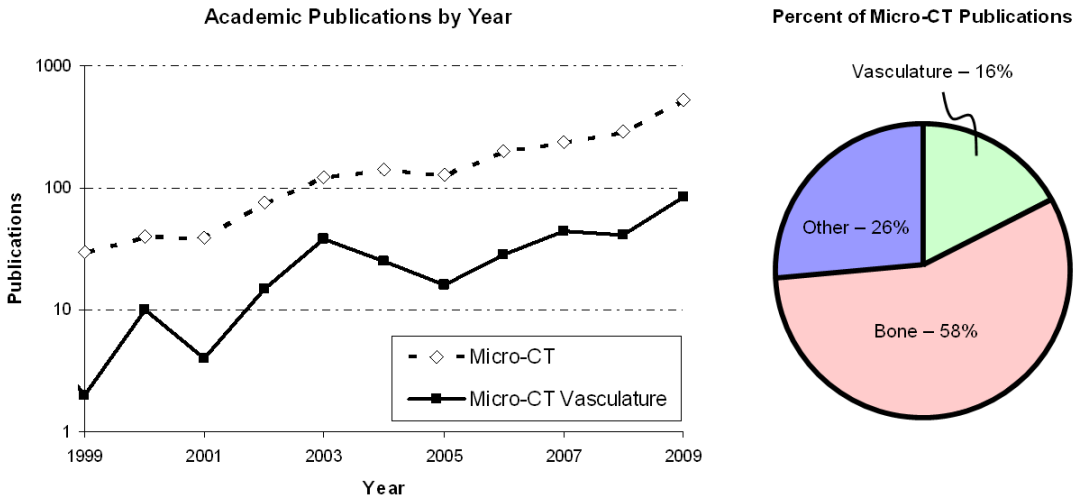

Figure 3.2: The increasing importance of micro-CT scanners is reflected in the rising number of micro-CT based research papers published each year, as displayed here in the left panel. The study of microvasculature, however, comprises a very small portion of micro-CT research investigations as shown on the right. The data were obtained through a query of the public database PubMed (MEDSUM tool). For the micro-CT publications, the mesh terms were: X-ray microtomography OR X-ray AND microtomography OR X-ray microtomography OR micro AND ct OR micro ct. The use of micro-CT for vasculature research had the same micro-CT mesh terms, along with the keywords: vessels OR vasculature OR microcirculation OR circulation OR blood. The micro-CT and bone data had the key terms: bone OR bones (in addition to the micro-CT mesh terms). From [54].

3.2.2 Theory

The basis for any computed tomography technique is that x-ray projection data are collected in an ordered fashion from multiple projection angles [56]. The projection data are a consequence of ionizing radiation's interaction with matter. In the energy range (10 - 50 keV) typically used in micro-CT imaging, the so-called photoelectric-effect is the main interaction mechanism [48]. At these energies, the attenuation of x-ray by the tissue decreases rapidly as photon energy increases. At higher energies (50 - 150 keV), the interaction is predominantly Compton – the attenuation changes very little with photon energy variations. The photoelectric-effect attenuates photons proportional to the third power of the element's order number, and is inversely related to the third power of the photon energy. Thus, the actual attenuation depends on both the material, as well as the energy spectrum of the x-ray source.

As an X-ray penetrates an object, the x-ray is exponentially attenuated by the material along its path. The attenuation law

$$I = I_0 e^{-\mu d}, \tag{3.1}$$

relates the number of photons I reaching the system's detector, to the number of photons I_0 incident on the specimen of thickness d. The energy-dependent material constant, μ, is called the linear attenuation coefficient. It represents the amount of radiation that is attenuated by, for instance, one centimeter of the material. Thus, the final attenuation reflects the product of all of these local linear attenuations along the x-ray beam's path.

To produce a three-dimensional CT image, collection of such two-dimensional projections at multiple angles of view are acquired. The two-dimensional projections can then be used to reconstruct a three-dimensional image. Finally, through the use of calibration phantoms or theoretical methods, the CT gray scale values can be converted into physically meaningful values, such as the Hounsfield Unit in which air has value -1000, and water has value 0.

3.2.3 Conventional Micro-CT System

In the simplest sense, all Micro-CT scanners are composed of three basic elements: (i) the x-ray source, (ii) the x-ray-to-electronic signal-converting imaging array, and (iii) a

method for either rotating the specimen or rotating the scanner around the specimen. Note that, the exact geometric arrangement of these components may vary. To facilitate high spatial resolution, the scanners rely on various approaches. For example, there are systems that utilize a conventional cone beam x-ray geometry [57], or others which have a parallel beam geometry with optical magnification [13]. In addition, commercial scanners are available that are essentially scaled-down versions of their clinical CT scanner counterparts.

Specimen Stage Rotation Geometry

Micro-CT systems which physically rotate the specimen within the field of view of the scanner's x-ray path are the design of choice for *in situ* imaging [16]. The benefits of rotating the specimen (as opposed to the source and detector) is that the design is robust, cost-efficient, and the system is an inherently simple design. Since there must be a high degree of precision in the system's mechanical components in order to allow high spatial resolution, a system with a reduced number of these components is easier to build and maintain. One drawback to the rotating specimen geometry is that the specimens must be fixed to the sample stage in order to prevent motion blurring [58].

The size of a 'rotating specimen' scanner is far smaller than a 'source-detector rotating' scanner. The length of these scanners translates into the diameter of the circular area required for scanner systems which physically rotate around the object. As an example, the custom-made scanner shown in Figure 3.3 would require a circular area 3 m in radius, as opposed to the roughly 1 x 3 m actually required by the 'rotating specimen' geometry [16]. In this figure, the three main components: the x-ray tube, the object on a rotating stage, and the flat panel detector, are shown. Translational stages are used in order to change the magnification found in the subsequent image by varying the distance between source, object, and detector (a feature not commonly found in the source-detector rotation geometry). An example micro-CT image of the portal vein from a rat liver (Microfil contrast agent, 20μm cubic voxels) is shown in Figure 3.4, which was imaged with an in-house micro-CT imaging system [13]. The image is a maximum-intensity-projection (MIP) of the volumetric data. To form a MIP image, 'rays' are cast in the direction of the 3D volume (which will depend on the desired rotation), and each pixel of the image has a brightness corresponding to the maximum

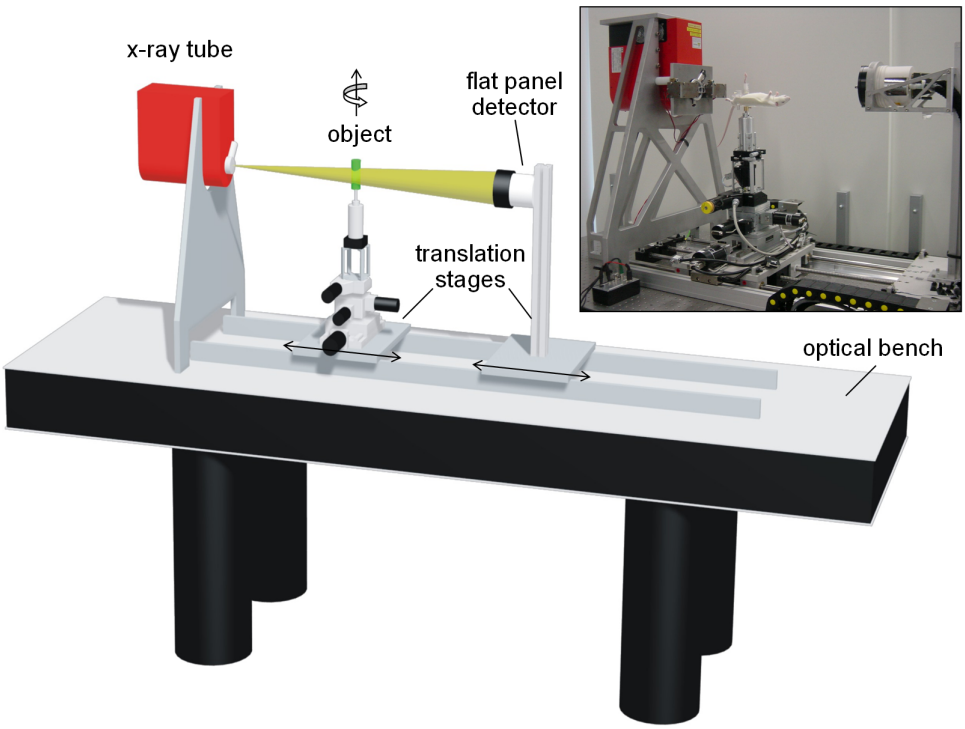

Figure 3.3: Illustration and photograph of a micro-CT imaging system with a rotating specimen geometry in which the object is physically rotated while the tube and the detector are stationary. The use of translation stages allows magnification settings to vary over a wide range. Scanners such as these can achieve very high spatial resolution and are most frequently used for ex vivo and in situ specimens. From [16].

CT value found in the ray's path.

Source-Detector Rotation Geometry

Rotating source-detector systems are more complicated (than rotating specimen scanners) with regard to mechanical setup [16]. However, they provide far more freedom with respect to object placement, and are practically a requirement for performing *in vivo* studies. In *in vivo* studies, it is typically not feasible to rotate the object (though it should be noted that *in vivo*, rotating specimen scanners, have been demonstrated [59]), and thus the specimen is kept stationary while the source and the detector are rotated [56]. An example of an *in vivo* micro-CT imaging system is shown in Figure 3.5.

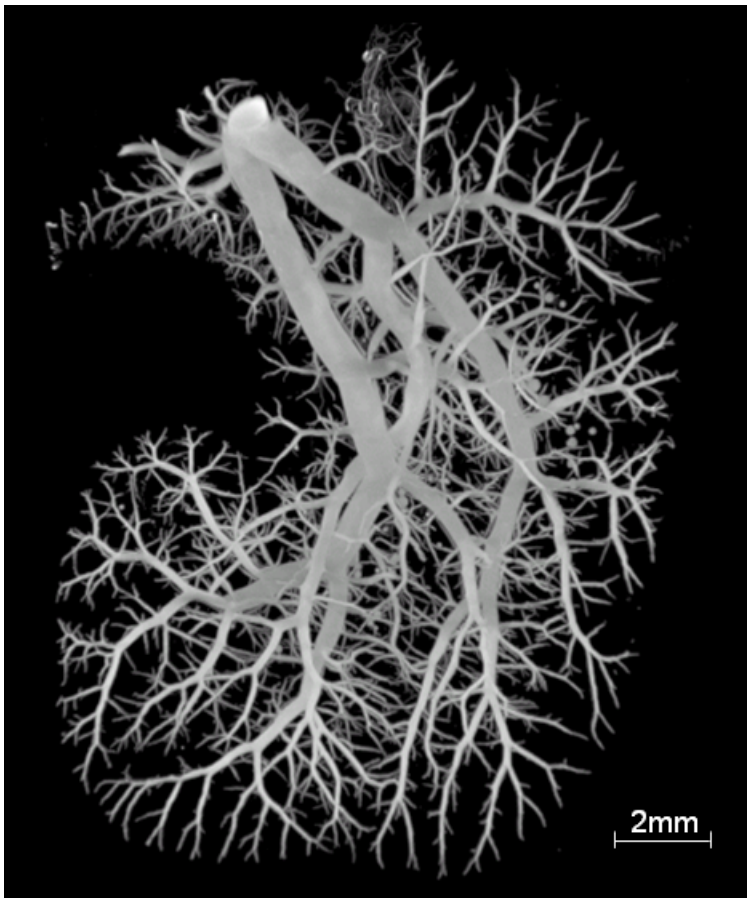

Figure 3.4: Maximum intensity projection of the micro-CT data (20 μm isotropic voxels) from the portal vein of a rat. The vasculature was filled with a contrast agent (Microfil) and was imaged in situ. Data such as this can then be used for measuring the geometry of microvasculature, such as the diameter and length of inter-branch segments. With a resolution down to only a few μm, highly accurate quantitative anatomic information is obtained. This information can therefore be used to infer various physiological functions such as perfusion territories, local shear stresses on the vascular lumen wall, pressure distributions and the magnitude of blood flow through the vascular tree's lumen. From [54].

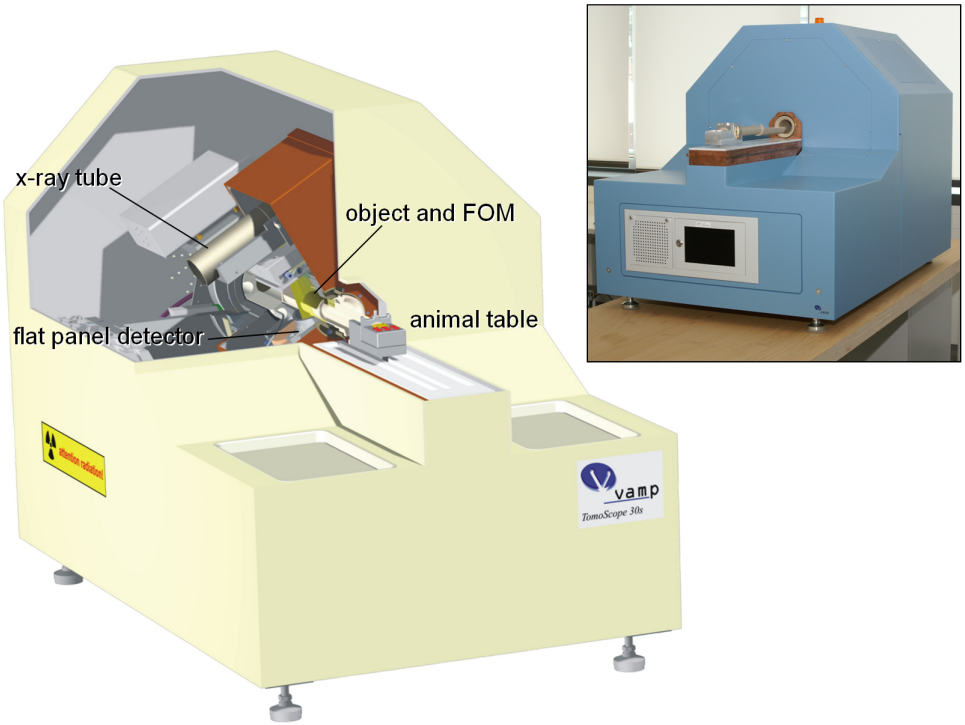

Figure 3.5: Illustration and photograph of a micro-CT imaging system with a rotating gantry geometry in which the X-ray source and detector are physically rotated while the specimen is kept stationary. Scanners such as these are typically used for in vivo scans. Since the X-ray source-to-specimen-to-detector distance is fixed, the degree of magnification in the image is not variable. From [16].

Removing the possibility for magnification is frequently done in such a system, in that the x-ray source, specimen table, and detector are a fixed distance from one another. Therefore, the geometrical resolution depends mainly on the pixel pitch and the matrix size of the detector used, as well as on the focusing mode of the x-ray tube [58]. Special care must be taken such that the varying gravitational forces no not change the rotation speed nor the mechanical alignment of the source and detector relative to each other, as well as relative to the axis-of-rotation.

3.2.4 Image Reconstruction

Cone beam reconstruction [60] is the most common method used to convert the projection data collected by the micro-CT imaging system's detector into the stack of slices used to generate the three-dimensional volume data set [56]. This method of reconstruction is further extended into the method known as filtered back projection. This involves projecting the measured profiles back over the reconstructed image area along rays oriented according to the angles used for the projections. Before performing the reconstruction, filtering methods are applied to remove artifacts and to enhance edges contained in the image (i.e., sharp CT gray scale changes). Other reconstruction methods exist such as iterative analytical and statistical methods. These methods produce superior reconstructed images (compared with filtered back projection), however their computational demand has only recently become feasible with the advent of graphical processing unit (GPU) parallel programming techniques. For instance, utilizing GPU parallel programming techniques, several orders of magnitude speed-ups have been achieved [61], which means that the possibility of improved images, reconstructed in a practical amount of time, is realizable.

3.2.5 Image Quality

X-Ray Dose

Image quality is inherently related to x-ray dose [16], a concern that is relevant for both *in situ* and *in vivo* studies. High spatial resolution requires high doses, and low doses means higher image noise and low image contrast. Therefore, to achieve a certain image quality within a given voxel, a certain number of photons must interact with that voxel.

In the case of *in vivo* studies, the animal may, for one, suffer from the radiation. In addition, issues pertaining to tumor growth (which could conceivably be modified by a micro-CT scan), and changes in cell population behavior (cells may behave differently after being irradiated), must be addressed when performing, in particular, longitudinal studies. Dose is also an issue in *in situ* studies since there exists the potential for radiation damage to the specimen, thereby altering the physiology.

Besides specimen concerns, there also exist technological limitations related to x-ray dose. The x-ray tube has a maximum power which is related to the focal-spot size. High

spatial resolution requires small focal-spot sizes. Thus a reduced x-ray power, which translates into a low x-ray dose, is necessary.

Beam Hardening

The x-ray energy from micro-CT scanners is inherently polychromatic (though synchrotron based radiation scanners (found at highly specialized national laboratories) are able to generate nearly monochromatic x-ray beams (e.g., Brookhaven National Laboratories' beamline). Due to the spectrum of energies, a phenomenon known as beam hardening is an important concern. Lower energy x-rays are attenuated more than higher energy x-rays when passing through an object, and the result is that the beam becomes more 'hard'. This leads to an inaccuracy of the attenuation coefficient of regions within the image, and is particularly evident when the beam passes through a high attenuator (such as bone), and then induces a shift in the attenuation coefficient for the material that the x-ray beam passes through afterward. Streaking artifacts are a consequence, which are observable in the reconstructed image. Post-processing methods can be applied to partially correct this problem, and also x-ray filters (such as plates of aluminum or copper 0.5 - 1.0mm thick) can be incorporated into the scanner system to filter out low energy x-rays before reaching the specimen.

Spatial Resolution

Another important parameter related to image quality is spatial resolution. This refers to the smallest resolvable distance between two structures that can be distinguished in an image. It represents the ability of the scanner to detect physical features, and depends on many factors of the imaging system (i.e., source, detector, scanner geometry). The modulation transfer function (MTF) of an imaging system is a common comparator of micro-CT scanner's spatial resolution (typically 10% MTF) [56]. In any real imaging system, the MTF is non-ideal in that the MTF values drop at higher spatial frequencies. For the case of vascular research, this results in the apparent broadening of small vessel diameters, as well as decreases the CT-value found in opacified small vessel lumens.

3.2.6 Multi-Modality Imaging

No single imaging modality will provide all the necessary information regarding microcirculation. The strength of micro-CT images lyes in their quantitative anatomic information, which thereby allows for inferences regarding physiological function. Combining micro-CT image data with another imaging modality that provides complimentary information provides for an even more comprehensive evaluation of vascular structure-to-function relationships [62].

A necessary component of such multi-modality imaging methods is that spatial and temporal registration of the three-dimensional anatomy must be achieved. Where micro-CT may provide excellent three-dimensional information pertaining to vascular branching geometry (for example), another imaging method may provide information related to perfusion territories, information which may be used to gain additional insight into the microcirculation. To perform image registration, a transformation or deformation field is applied to one volume, thereby allowing alignment with the other volume [18].

3.3 SPECIMEN/ANIMAL PREPARATION

Unfortunately, the blood and vessel wall have little inherent difference in contrast for X-ray imaging. Specimen preparation is therefore an important step in micro-CT microcirculation studies so that the vasculature in the image can be visualized and contrast agents are used to delineate the vasculature. The considerations in specimen/animal preparation and contrast agent usage differ depending on the study. For example, *ex vivo* studies frequently utilize contrast agents in conjunction with casting polymers so that the vasculature produces significant signal in the reconstructed image and the surrounding tissue may be corroded away (thus reducing image noise). *In situ* and *in vivo* studies similarly rely on contrast agents, though the exact composition differs depending on the nature of the study. Since the vasculature does not have sufficiently different contrast from tissue parenchyma and the opacification of the blood (which makes the lumens easily visible by CT) is either transient as it flows through a vessel, or if all blood is opacified for a long time (hours), then the concentration must be kept below

the level that would alter any physiology. One consistency in all cases (e.g., *ex vivo*, *in situ*, or *in vivo*) is that pressure and volume of the infused contrast and solutions, as well as animal positioning and preparation, should be as reproducible as possible [18].

A particular branch of experiments that are well-suited to micro-CT imaging studies are studies utilizing probes to characterize various properties of vasculature. These methods may, for example, involve simulating embolizations by injecting microspheres into different vascular structures. The microspheres block vessel segments of a given lumen diameter [63], or the effect local perfusion defects have on vessel lumen walls [20]. In addition, gene knock-out [64], altered nutrition [19, 23, 65, 66], or disease/syndrome simulation [67] studies are frequently performed utilizing micro-CT.

3.3.1 Ex Vivo - Casting

Using a partially polymerized methylmethacrylate plastic (typically Batson's No. 17 corrosion-casting compound), casts of vascular networks can be created. The details of this standard casting technique was outlined by Gannon [68]. The details of a recent study [69] where the cast of a rabbit's kidney vasculature was made and imaged by micro-CT is next described in order to outline the relevant steps involved.

A 1-year-old female New Zealand white rabbit weighing 2.2kg was euthanized by intravenous injection. Next, the animal's thoracic cavity was exposed by a ventral incision and the renal artery was cannulated. Heparinized saline solution was perfused through the vasculature using a three-way valve. This was performed to prevent blood clots from forming. Note that the perfusion pressure is an important consideration. Here a pressure of 100 mmHg was used and 20-40 mmHg would have been used if performing venous perfusion (to prevent vessel wall rupture).

Once blood was cleared from the tissue, the valve was switched to perfuse a freshly prepared Batson's No. 17 solution. The Batson's solution was allowed to polymerize within the animal's tissue. With the specimen in an ice bath, the polymer took 2-3 hr to cure. The use of an ice bath helps slow down the polymerization process which helps to minimize cast distortion during this exothermic reaction.

Once fully polymerized, the tissue was immersed in a 25% potassium hydroxide solution for 24-48 hr. This solution corrodes away the tissues leaving only the polymerized

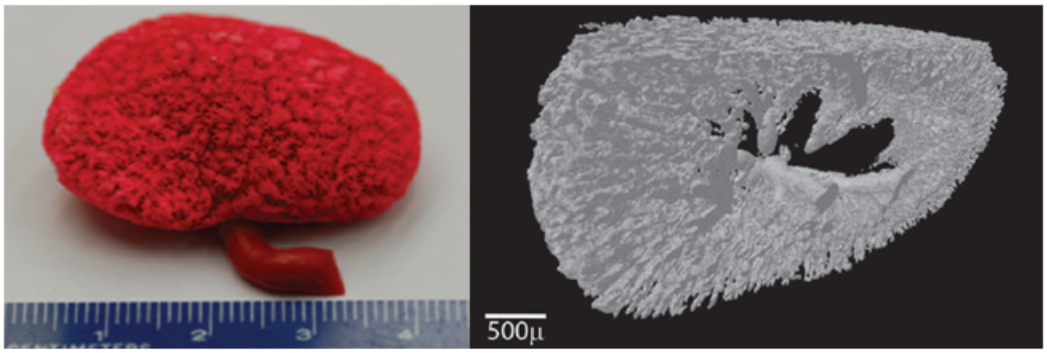

Figure 3.6: Left panel: vascular cast of a whole rabbit kidney (ruler is in centimeters). Right panel: 3D volume rendering of a portion of the vascular cast of a whole rabbit kidney, imaged by micro-CT (35 μm voxel size). Modified from [69].

plastic which represents the vascular tree lumens. The cast may then be imaged by micro-CT. The method of casting is clearly destructive but has the benefit of removing the surrounding tissue, which can cause potentially significant background noise in the subsequent micro-CT image. An image of both the created cast, as well as a representative micro-CT image are depicted in Figure 3.6 [69]. Although casting methods were experimented with for this dissertation, *in situ* methods of vessel enhancement were found to be better suited for the purpose of studying the dual blood supply of the liver.

3.3.2 In Situ - Contrast Agent Enhancement

In order to image intact specimens, a contrast agent such as Microfil is frequently used [13, 57, 69, 70]. The procedure is performed as discussed in the previous subsection, however the Batson's No. 17 corrosion casting compound is replaced by the contrast agent. A contrast agent, such as Microfil (which is laced with $PbCrO_4$), allows for the analysis of intact vasculature due to its high X-ray attenuation (2500-5000 HU) so that the perfused vessel lumen can easily be delineated from surrounding tissue. In contrast, the corrosion casting method (discussed in the previous subsection) has relatively low attenuation (0-1500 HU) and is essentially a means for extracting the vasculature from the surrounding tissue (thus requiring that the surrounding tissue be removed). An

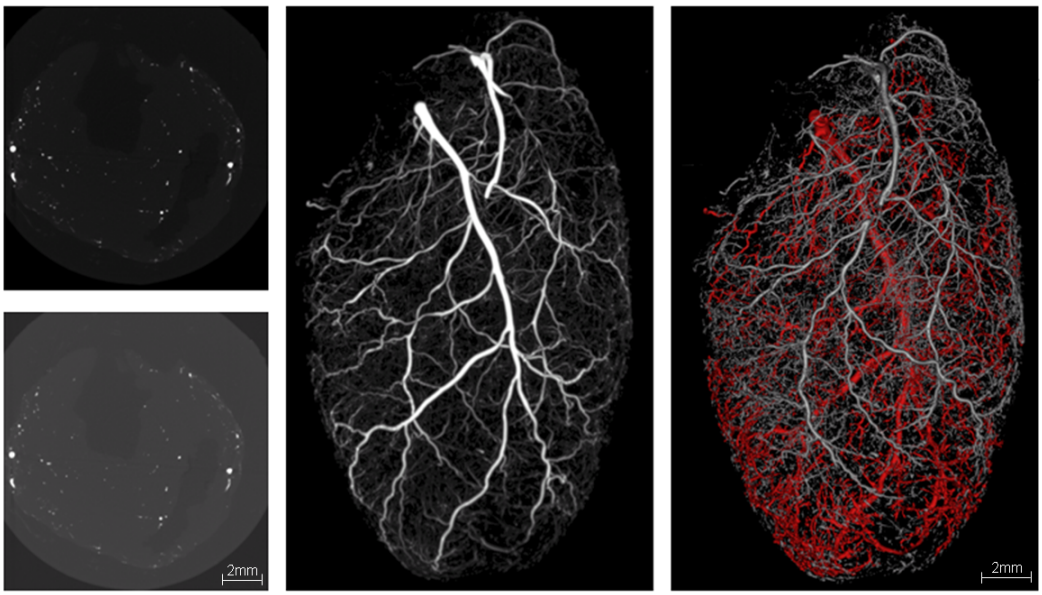

Figure 3.7: Micro-CT image data (20 μm isotropic voxels) of the vascular bed of a rat heart, which was filled with a contrast agent (Microfil) and was imaged in situ, is here displayed by different visualization methods. In the left column, cross-sectional slices are shown for two different gray scale windowing levels. In the middle panel, a maximum intensity projection (MIP) of the micro-CT data of the same vascular bed is displayed. Using a region-growing segmentation method, a fully connected vascular tree can be segmented, here shown in red in the right panel. The vasculature in the image that are displayed as gray are either from the right myocardial arteries, or are disconnected vessel segments due to the segmentation process or low contrast agent concentration. From [54].

example of the vascular bed of a rat heart is displayed in Figure 3.7.

3.3.3 In Vivo

The long scanning times of *in vivo* experiments (between 0.5 to 2hr) requires contrast agents to either circulate, or be continuously infused into the vasculature being imaged [18]. Since contrast agents used for *in vivo* studies can be administered multiple times to the same animal, the possibility for longitudinal micro-CT studies exists.

Using a conventional iodinated vascular contrast agent (which is encapsulated within polyethylene glycol-stabilized liposomes) intravascular space was shown to be suitably

enhanced for more than 3hr [71]. Iodinated triglycerides containing lipophilic cores of oil-in-water lipid emulsions (offered by Fenestra) provide long-lasting visualization of vascular systems with micro-CT [18]. Kong et al. [72] used pluronic F127 and a naturally iodinated compound (Lipiodol) to successfully form radiopaque nanoreservoir structures. For purposes of studying the dual blood supply of the liver at high-resolution, *in vivo* imaging methods would complicate the task by introducing motion issues, as well as imposing limitations on X-ray dose.

3.4 IMAGE ANALYSIS

A great challenge for the researcher studying microcirculation by micro-CT imaging is the post-processing of the reconstructed image data. At the foundation of this challenge exists the overall goal of accurately quantifying the microvascular structures topology (i.e., connectivity or hierarchical nature), and its morphology (i.e., measurement of various properties such as branch segment lengths, diameters, branching angles, vessel surface area, etc). Being able to accurately characterize these properties of the microvasculature, flow patterns may be understood, optimal design principles may be exposed, and model systems may be fabricated.

The image analysis of micro-CT images shares a great deal with other imaging modalities. Many algorithms, theories, and methods designed for different problems have been borrowed from other imaging methods and have seen success in their application to micro-CT images. Of course, the image analysis of micro-CT images continues to improve and contribute to the other imaging methods as well.

Many existing programs exist for performing image analysis including the Analyze software program [73], Skyscan's (Kontich, Belgium) image analysis software, Matlab (Mathworks Inc.), and the software program Mimics by Materialise (Leuven, Belgium). Open source programs such as VTK can be used for visualization of micro-CT image data, also ITK offers a whole host of image analysis algorithms for image registration as well as vascular segmentation, and ImageJ is an excellent tool for performing various measurements of components within an image.

In the following subsections, methods pertaining to vascular segmentation, extraction of vascular centerlines, measurement of various geometrical properties, and modeling principles are discussed.

3.4.1 Segmentation

The task of delineating what is, and what is not vasculature in an image has been studied by many research groups [22, 74, 75]. Typically, in microcirculation imaging studies this is a two-phase problem, in the sense that we are interested in the vasculature, and not interested in anything else (background). Due to the use of contrast agents, the simple method of thresholding is the most common technique [18, 76, 77]. In this sense, the gray scale value of each voxel is considered, and if it is within a certain range, it is set to being a vessel voxel (a one for instance), whereas if the voxel is outside of the specified range it is not a vessel voxel (and set to zero). The process of image segmentation converts a gray scale volume data set into a binary data set, whereby the vasculature is easily represented as one distinct phase. A connected component analysis (region growing) can then be used to distinguish different vascular structures within the image. Shown in Figure 3.8 is an intramyocardial cast from a human, volume rendered at four different CT gray scale thresholds. Clearly significant differences in the vasculature are evident which suggests that threshold choice is an important processing step and must be carefully chosen. Algorithmic approaches have been used to account and alleviate the influence of threshold choice on subsequent vascular measurements [76].

The problem of segmentation is compounded by beam-hardening, aliasing artifacts, partial volume effects, ring artifacts, and the non-ideal modulation transfer function of the imaging system. This causes values of certain tissues (i.e., the lumen of vessel trees) to not be a specific value, but rather take on a range of values. Methods developed to overcome some of these problems include object tracking algorithms [74], local adaptive region growing methods [22], active contours [78], as well as tubularity-measure or Hessian-based filtering techniques [75]. The best approach depends on the quality of the micro-CT data in terms of how well the object stands out from the background, and also just how complex the vascular structure is. For instance, Hessian-based filtering methods (which characterize the degree to which a voxel appears to pertain to

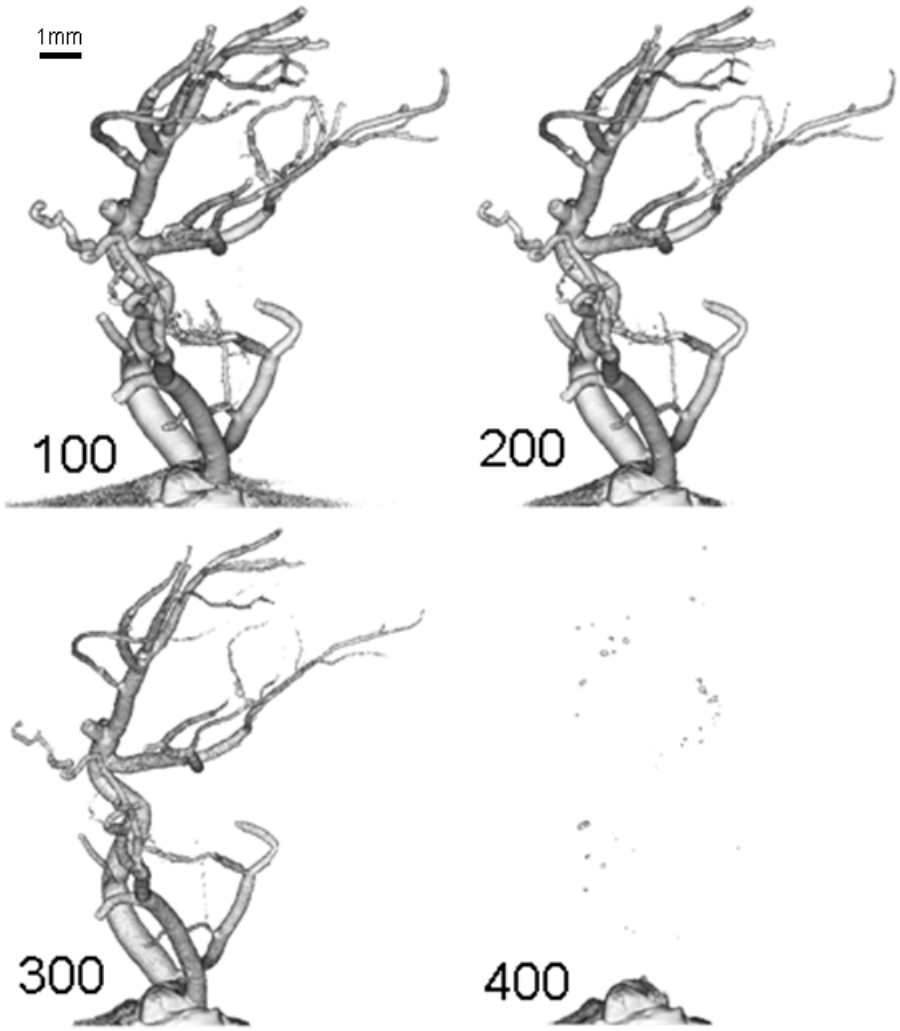

Figure 3.8: Micro-CT image data (20 μm isotropic voxels) of a corrosion cast of a human coronary artery. The material used to fix the specimen is seen at the bottom of each image. Here, volume renderings of the cast are displayed for different CT gray scale threshold choices. This threshold sets any voxel with a CT value greater than the threshold such that it is considered when creating the volume rendering (a rendering of the surface of the vasculature). All voxels with a value below the threshold are thus not visualized. The non-uniform nature of the CT gray scale is seen here, in particular the lower values for branches with smaller diameters (since these are the first branches to be removed upon raising the threshold). Also, it can be seen how all of the branch segments become thinner as the threshold is increased. This results from the partial volume effect (whereby the vessel may only cross through part of a voxel and thus not attain as high of a gray scale value as those voxels which are fully within a vessel), as well as from blurring by the imaging system's modulation transfer function. This blurring has a larger effect on vessel segments with a small diameter than it does on larger diameter vessel segments. From [54].

a cylindrical type structure) have problems at bifurcation points since the vessel tree does not appear tubular in these regions. Also, active contour methods typically rely on user specified parameters such as the number of iterations that the algorithm should run through, as well as various weighting parameters. Thus, a particular method should be chosen for each image analysis study which is reliable and repeatable.

3.4.2 Centerline Extraction

Another pre-processing step for the subsequent characterization of vascular branching geometry is known as centerline extraction. The 3D segmented data set is used as the input for the extraction of the vascular tree's centerline ("skeleton"). The extraction of the vascular tree centerline allows for the simplification of the complex tree structure from which the branch segment location within the tree, and its connection to the other branch segments, is conveyed (essentially the first step in defining the vascular tree topology). Using locations along the centerline within the segmented image, the tree's hierarchical nature, branch lengths, branch diameters, and branching angles can subsequently be determined [76].

There exist many different methods for finding the centerline of vasculature. The three main categories are: (i) iterative thinning [79] (i.e., peeling away surface voxels) (ii) mesh contraction [80] (i.e., shrinking), and (iii) "fast marching" based methods [81, 82]. In [76] it was shown that thinning methods suffer from whiskers and shortening of branch segments (a consequence that is accentuated for thicker branch segments).

3.4.3 Measurements

The measurement of length, diameter, and the connectivity relationship between inter-branch segments lie at the foundation of most vascular geometry research [25, 83]. Other properties such as branching angle, vessel volume, and vessel wall surface area are also relevant parameters of vasculature which can be produced with knowledge of the former. Accurately measuring vascular branching geometry is a task well suited to micro-CT image analysis. Manual-based methods can be performed, such as using a software program to measure cross-sectional widths of vessel tree lumens in two-dimensional slices.

For high throughput experiments, automated methods are desirable in order to generate large amounts of data, in relatively short amounts of time. The data can therefore be reproducible and not constrained to the problems that surface from user subjectivity.

3.4.4 Erode/dilate analysis

Micro-CT offers an excellent framework from which to analyze intact microvascular beds, and a sequential 'erode/dilate' technique [63, 84, 85] which progressively eliminates branches of increasing diameter is one approach that greatly reduces image analysis effort. By this method, the total luminal volume of different diameter branches is calculated. The method operates on a segmented image of the vasculature.

The method uses the morphological operations of erosion and dilation [86, 87] whereby the segmented vascular bed is eroded and then dilated 'n' number of times, where 'n' is the iteration number (which can be related to the diameter of vessel segments lost at each iteration). After each iteration the total vessel volume is measured. The results are then binned according to the vessel volume 'V' that is lost (i.e., $V(n-1)-V(n)$) by removing individual branches $2nh$ in diameter ('h' is the voxel size). This method has the benefit of being able to easily deal with highly complex structures, as well as images where multiple vascular trees exist.

As a few examples, the question of whether vasculature grows in proportion to the myocardium as the rat heart develops was studied by the erode/dilate method of analysis [84], and the method was shown to compare accurately to the results of more complex methods, as well as indicate what diameter interbranch segments trap a microsphere of a given size [63].

Segment Length

Once a vessel tree's centerline is extracted, measurements of the individual branch segments' length can be easily performed. The measurement of an individual branch segment's length can be determined by moving from one voxel to the next in the list of ordered centerline voxels, calculating the Euclidean distance between contiguous voxels, and summing the distances.

Ideally, the length of the branch segment is given by the line integral:

$$L(C) = \int_C ds, \tag{3.2}$$

where ds is the infinitesimal element of length measured along the curve C. The approximate method described is therefore essentially the "sample-distance" method [88] where geometrically the curve C is being approximated by the connected polygonal curve whose vertices are the branch segment's centerline voxels. Another method, that of simply counting voxels [73, 89], can significantly under-estimate interbranch segment length. Further smoothing of the centerline, either through a moving average type approach, or curve-fitting can further improve the accuracy of interbranch segment length measurements.

Segment Diameter

In [76] several methods for measuring the branch diameter were tested including: distance map computation, cross-sectional area determination (brightness area product based methods), as well as volume based methods (where the diameter was then calculated based on the segments length and volume). These methods were observed to over-estimate small vessel diameters. Another detailed study by Hoffman et al. [90] compared the various techniques for determining vessel diameters. The main conclusion was that no technique perfectly characterized vessels over the full size range found in angiographic images, yet it was suggested that a derivative-based technique was the most accurate for larger vessels. For vessels with diameter greater than 2 times the FWHM of the scanner's MTF, the first-derivative edge detection as well as a thresholding technique of the local FWHM accurately characterize the input square wave's width. At a basic level, the convolution of a square wave function and a Gaussian blurring function results in an image which has a correct width at exactly half the original intensity (i.e., FWHM). All of these methods will over-estimate smaller diameters. The method of determining the full-width half-maximum (FWHM) diameter for large branch segments is therefore accurate.

3.4.5 Modeling

Analytical

The data regarding branching geometry can be investigated by analyzing the geometric properties of the vascular structures, in particular with regard to the model derived by Murray [8] on the basis that the fluid transport system (vasculature) geometry is consistent with simultaneous minimization of both the power loss of laminar flow and of a cost function proportional to the total volume of material needed to maintain the system (lumenal contents) - factors that have opposing geometric consequences. The vessel tree structures can be modeled as a binary tree in that at each bifurcation there exists one parent segment that divides into two branches. The 'level' (or generation) of the branches is one higher than that of their parent branch segment.

Use of the Hagen-Poiseuille equation [32]

$$\Delta P = \frac{8\mu l Q}{\pi r^4}, \tag{3.3}$$

which describes laminar flow of an incompressible Newtonian fluid through a pathway with a circular cross-section. ΔP is the difference in pressure between the inlet and outlet, μ is the fluid's dynamic viscosity, l is the path length, Q is the volumetric flow rate, and r is the radius at each voxel along the path, can also be used to calculate fluid flow resistance through different sections of vasculature, as well as local shear stresses on vascular walls [25].

Computational Fluid Dynamics

More computationally demanding methods to characterize vasculature exist. These typically include fluid dynamic simulations. The pressure distribution within vascular trees can be computed as well as shear stresses [70].

Chapter 4

Accuracy of Microvascular Measurements Obtained from Micro-CT Images

4.1 INTRODUCTION

The state of microvasculature can reflect and/or be the cause of pathophysiological changes in organ function. Analysis of 3D tomographic images can be used to characterize the branching geometry of the microvasculature - but due to the huge logistic problem, automation of such an analysis is essential. At a basic level of investigation it is sufficient to examine the density or overall pattern of vasculature, but a more detailed analysis of the microvasculature, which deals with the tree's hierarchy as well as its physical (and fluid dynamic) properties, provides quantitative insight into its capacity to transport blood throughout an organ. In particular, how the spatial heterogeneity of perfusion distribution relates to the branching geometry of the microvasculature, is an important question which has been addressed by various investigators [9, 57, 91, 92].

This chapter was modified from the original manuscript: **TL Kline, M Zamir, and EL Ritman. Accuracy of Microvascular Measurements Obtained From Micro-CT Images.** ***Annals of Biomedical Engineering*****, 38(9):2851-2864, 2010.** and reproduced by permission of the publisher: Springer (see **Chapter A**)

The measurement of length, diameter, and the branching angles and connectivity relationship between interbranch segments lie at the foundation of almost all vascular bed characterizations. For example, using segment diameters and interbranch segment relationships, wave reflection effects in a right coronary artery were studied [83] and a model of a branching tree was developed [25]. To measure these properties of the vasculature, a technique with a high degree of accuracy is needed that can deal with both the wide range of dimensional scales and the inherent complexities of the microvasculature. Although many attempts have been made to automate such image analysis processes, a major problem has been the lack of accurate and precise measurements (or a "gold-standard") against which such programs could be evaluated. Qualitative parameters are generally used to establish the utility of a newly developed image analysis algorithm. In this sense, the fact that a vessel was found or not found, the extracted centerlines were smooth or not smooth, a noise 'blob' was removed or not removed, are measures used to justify the effectiveness and accuracy of a particular method. The gold-standard used in this study is the optical measurement of the branches of intact casts of vascular trees, with each vascular segment mapped out and measured using micrometer translation and rotation [10]. Based on these optical measurements, the tree's hierarchical structure in terms of interbranch segment connectivity, individual branch segment lengths, and individual branch segment diameters becomes 'known'. This study evaluates the accuracy with which 3D micro-CT image data can convey this information of vascular branching geometry, as compared to direct optical measurement of vascular trees.

The optical measurement method is thought to be more accurate and is therefore used as the gold standard for testing the measurements obtained from micro-CT. Casts, on which the gold-standard is based, are frequently used for measuring vascular branching networks [10, 93]. However, such a method typically loses information pertaining to the interconnectivity of the branch segments due to the fact that often the casts are physically broken in order to measure the physical dimensions of interbranch segments. Statistical analysis approaches are then used to say something general about the characteristics of that vascular bed [2]. The method of optical measurement is very time consuming, labor-intensive, and highly inefficient. Therefore, the automated method analyzing micro-CT images is of great benefit. For the work presented in [10], more than a year was spent doing measurements of the vascular tree from a right coronary

artery, and a few months were spent on *h61* and *r14*, the two human coronary artery casts used in this current study. Also, because the measurements are made from a cast of the vascular tree, the hand measurement method is somewhat destructive in the sense that the vascular bed is isolated from the perfused tissues, which are destroyed in the process. Hence, the method of casting is not applicable to the tissue of a living specimen. The cast was used solely to check the accuracy of our approach and could be thought of, rather, as a test phantom (i.e., a structure of 'known' dimensions).

Using the automated analysis of micro-CT images, instead of optical measurements of a cast, saves time and allows analysis of highly complex tree structures. More important, using micro-CT images of *in situ*, opacified microvasculature, instead of an isolated cast, offers the opportunity to extend the technique to *in vivo* analysis. While this paper actually uses the micro-CT images of the casts, this was done only for the purpose of establishing the accuracy of the image analysis method.

Quantifying the impact that the vascular branching geometry has on blood flow distributions still involves uncertainties attributable, in part, to measurement inaccuracies, as well as the fact that measurements are obtained from somewhat distorted (due to casting and/or imaging process) representations of the vascular tree, or the fact that the representations are a "snap-shot" taken from a dynamic geometry (due to cardiac pulsation and/or dynamic smooth muscle tone). In addition, the micro-CT imaging process introduces blurring due to the modulation transfer function of the scanners imaging system [94], and partial volume effects due to pixelization of the image data [95]. Variance in the gray scale of the resulting image also depends on the tomographic approach used (e.g., number of angles of view, cone vs. parallel beam, etc. [96]). The effect of blurring disproportionately affects the accurate determination of small vessel diameters. In any real imaging system, the modulation transfer function (MTF) is non-ideal in that the MTF values drop at higher spatial frequencies. This results in the apparent broadening of small vessel diameters, as well as decreases of the CT-value found in opacified small vessel lumens. To account for this, a method was developed that incorporates both a vessel lumen's local gray scale value, and the fact that the gray scale of the lumenal contents should always have a fixed value.

Previous image analysis methods contain significant problems, including: large computer memory requirements and long run-times [82, 97], post-processing manual tree

editing procedures and problems dealing with small vessel measurements [73, 98], among others. The present micro-CT analysis differs from others [24, 74, 99] in that it has an objective basis for evaluation of the image analysis approach's accuracy and thereby can provide added insight into the accuracy of the vessel lumen centerline, and interbranch length and diameter measurements. The extracted lumenal centerline provides insight into the interconnectivity of the branch segments and is also used for the measurement of interbranch length and diameter. Our centerline extraction method contains modifications of existing methods - modifications which were found to improve such centerline properties as: basic centered-ness (i.e., how well the centerline is actually centered within tortuous paths), the accurate representation of bifurcations, and automatically finding vessel tree endpoints.

Finally, having created an accurate measurement method, we will be able to study questions such as vessel tree branching patterns. This includes the relationships between parent and its branch segments (parent is the root segment that bifurcates into two branch segments) and whether the branching pattern as a whole is responsible for, or reflects, the spatial distribution heterogeneity of perfusion. Another is the question of how well a micro-CT scan of a vascular tree, which is a snap shot in time, represents the dynamic tree geometry. For instance, how important is the diameter change caused by the pressure pulses resulting from the contraction of the heart? This question can only be answered by doing *in vivo* scans at many time points within a single cardiac cycle. However, *in vivo* we do not have a way of determining the accuracy of measurements, and thus an in depth comparison, as performed in this study, is aimed at assessing that accuracy.

4.2 METHODS

4.2.1 Gold-Standard

The casting method used was discussed in more detail by Zamir and Chee [11] and is here more succinctly described. The casts were produced using a partially polymerized

methylmethacrylate plastic (Batson's No. 17 corrosion-casting compound: Polysciences Inc., Warrington, Pa.), adding the red color dye for observation. This initially freely flowing liquid was injected through the main coronary ostia, maintaining a pressure between 100 and 120 mm Hg. The vascular micro circulation was reached within the first few minutes. Within half an hour setting occurred, resulting in a rigid cast of the vascular lumens. The myocardial tissue was digested by immersing the heart in a 34% potassium hydroxide solution for several hours and then rinsing in warm water. This process was repeated as necessary, with the end result being an accurate replica of the coronary vasculature.

Displayed in Figure 4.1 (left) is a micrograph of the cast of *h61* , which is a sub-segment (or piece) of the entire vasculature. A detailed analysis of each of two casts was carried out by optical measurements of individual branch lengths and diameters depicted in micrographs. The samples were placed under the microscope and the vascular segments were mapped and measured utilizing micrometer translational and rotational movements [10]. The tree's hierarchical structure was labeled in (J,K) notation [100] as illustrated in Figure 4.2. Under this notation, 'J' is the level (or generation) and 'K' is the sequence within that generation of the individual branch segment. Also, under this labeling scheme, the larger diameter branch receives the odd 'K' sequence label (i.e., the larger diameter branch of (1,1) is (2,1), and the smaller diameter branch is labeled (2,2)).

For these measurements, the bifurcation point was defined as the point at which the extrapolated centerlines of the parent and its two branches meet. If a centerline was curved then it was replaced by its tangent at the bifurcation point. Diameters were measured at three places along a vessel segment and an average was taken. These methods pertaining to the measurement of vessel segment diameter and vessel bifurcation representation are also discussed in [101]. The segment length was taken as the length of the centerline connecting the proximal and distal bifurcation points of the segment (or an endpoint of the terminal vessel segment). If the centerline (i.e., branch segment) was curved then it was divided into smaller sub-segments and the chord lengths of each sub-segment were added. Finally, matching the individual segments in the micro-CT image to the schematics from these optical measurements allowed for the definitive, branch-to-branch, comparison of micro-CT measurements of the individual branch segments'

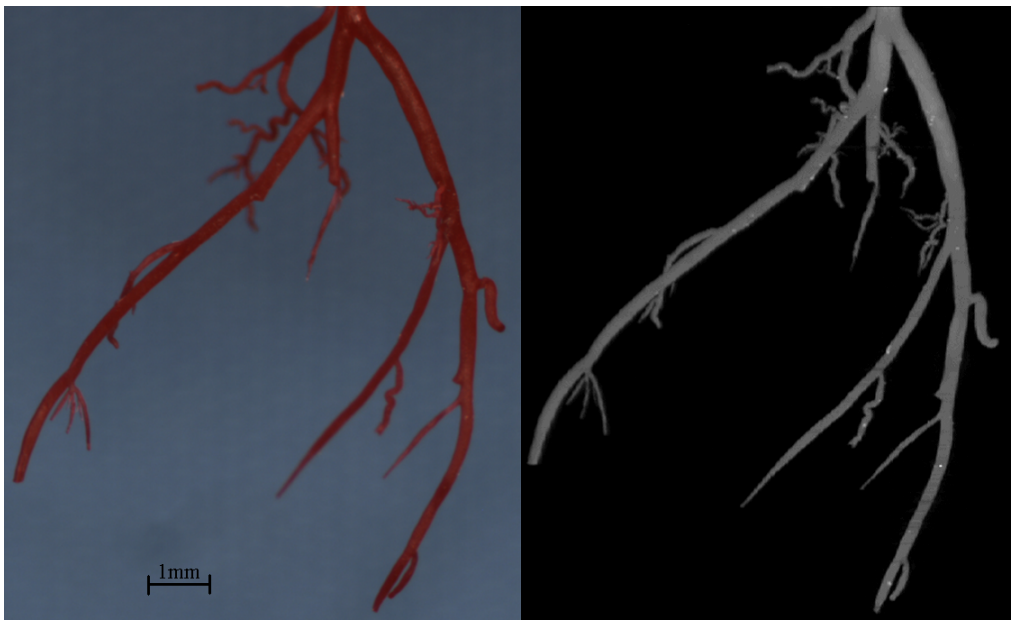

Figure 4.1: Left panel: microscope digital photograph of specimen *h61*. Right panel: maximum intensity projection of reconstructed micro-CT image. From [76].

lengths and diameters.

4.2.2 Micro-CT Imaging

Micro-CT images of the two casts were used as the volume data sets for analysis. Figure 4.1 (right) is the maximum intensity projection of *h61*, visualized with the Analyze software package [73]. The micro-CT imaging methods that were used are discussed in more detail elsewhere [13]. Briefly, the vascular cast was mounted on a computer controlled rotating stage so that an x-ray projection image was generated on a CsI crystalline plate, which converted the x-ray into a light-image, at each of 360 angles of view around 360^o. This image was optically projected onto a CCD imaging array which converted the light intensity on each of the 1024×1024 24μm on-a-side square pixels in the array to an electronic signal proportional to the light (x-ray) intensity. The data, once recorded, were subjected to a modified Feldkamp cone beam reconstruction algorithm [60] to generate a 3D volume data set. The 3D image consisted of up to 1024^3 cubic

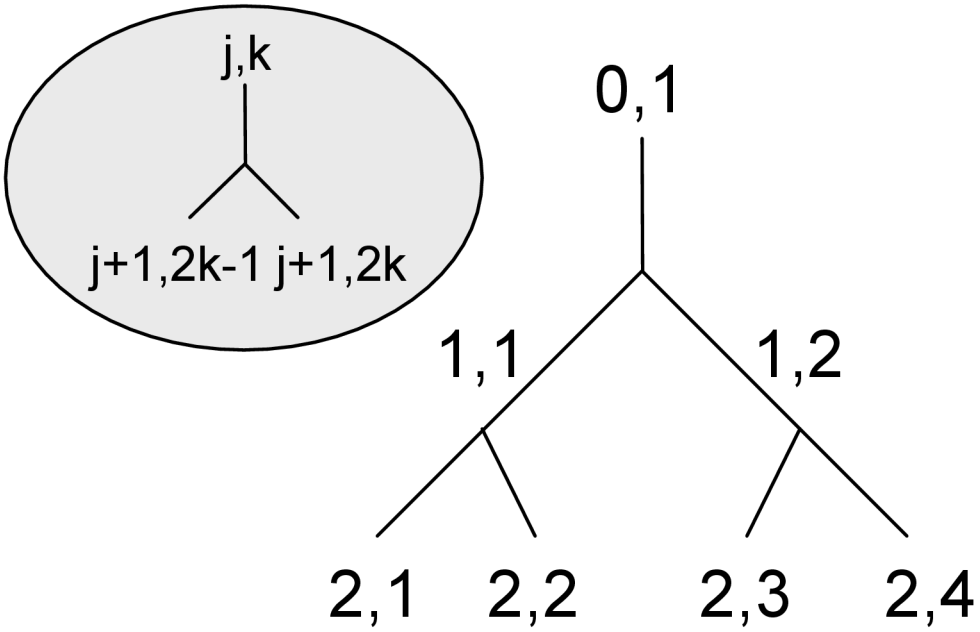

Figure 4.2: The J,K notation used for labeling the vessel segments in a tree structure, adapted from [100]. In general if j,k are the coordinates of a parent segment, then the coordinates of the two branches are j+1,2k-1 and j+1,2k respectively, the latter being the branch with the smaller diameter. In particular, if the root segment is labeled as 0,1, then the labels of its two branches will be 1,1 and 1,2 respectively, the latter being the branch with the smaller diameter. From [76].

voxels, each 18μm to a side, with gray scale equal to the x-ray attenuation coefficient in units of 1000cm^{-1}.

4.2.3 Segmentation

A binary file was first computed from a thresholding of the gray-scale 3D micro-CT images. Nearly all of the background (i.e., not cast) image noise could be filtered out through the technique of thresholding because the signal (i.e., the gray scale of the cast material) and the background were divided into two "well separated" distinct gray scale populations. The vascular trees were extracted from this image by means of a region-growing segmentation method to include those voxels, with gray scale values above the thresholded range, that were connected to the vessel tree's root which was initially identified by visual inspection. In order to include small vessel segments, a low CT-threshold of 400 (much lower than half the max value found in large vessel lumens) was chosen in order to include vessel segments that have a reduced peak gray-scale value caused by blurring. The region-growing method resulted in a single connected tree structure for both specimens, *h61* and *r14*.

4.2.4 Centerline Extraction

The segmented volume data set was used as the input for the extraction of the vascular tree's centerline or "skeleton". This is the first step in defining the vascular tree topology. The extraction of the vascular tree centerline allows for the simplification of the complex tree structure from which the branch segment location within the tree, and its connection to the other branch segments, is conveyed [102]. In the case of *h61* and *r14*, this graph is a binary tree in that one parent bifurcates into two branch segments. Using locations along the centerline within the segmented image, the tree's hierarchical nature, branch lengths, and branch diameters can subsequently be determined.

Our centerline extraction method utilizes the fast marching algorithm [103], which simulates the propagation of a wave. This algorithm begins at a source, in this case a single voxel at the root of the tree, and emanates a wave in all directions. This

propagating wave is governed by a weighting map which specifies how fast the wave can travel at each voxel it touches as the wave radiates outwards. The weight incorporates details of a vessel voxel's distance to the closest segmented surface. The weight function is such that the wave propagates only inside the lumen of the tree. As the wave passes over each voxel, how long it took the wave to get to that voxel is recorded. Therefore, this arrival time is a function of both the distance a particular voxel is from the source of the wave front, as well as the weighting function that the wave front experiences along the way.

In $\mathbb{R}^3$ we begin with a potential function $F(x)$ that weights vessel tree voxels according to their distance from the vessel wall. The weighted geodesic distance (later referred to as the "arrival time function" under the fast marching algorithm's framework) between two points $x_0, x_1 \in \mathbb{R}^3$ is given by [104]

$$U(x_0, x_1) = \min_{\gamma} \left(\int_0^1 \frac{\|\gamma'(t)\|}{F(\gamma(t))} dt \right), \tag{4.1}$$

where γ is the geodesic curve with $\gamma(0) = x_0$, $\gamma(1) = x_1$, and $\|$ represents the Euclidean norm (i.e., the vector length). In the case that $F(x) = 1 \forall x$ then the integral in Eq. 4.1 is simply the length of γ and U is the Euclidean (straight-line) distance between x_0 and x_1. To obtain the arrival time function (weighted geodesic distance), we adapted the Eikonal equation [103]:

$$\|\nabla U\| = \frac{1}{F}, \tag{4.2}$$

where U is the arrival time function and F corresponds to the weight function or the "speed" of the front progression (we defined F to be the square of the distance map, as discussed later). This equation is solved by computing the arrival time function U at location *(x,y,z)* using the arrival time value of its neighbors.

Due to the discrete nature of the gradient ∇U in the voxel-based representation of the vessel tree by micro-CT imaging, the corresponding discrete solution to Eq. 4.2 is given by [105]

$$\left[\begin{array}{l} \max(D_{xyz}^{-x}U,0)^2+\min(D_{xyz}^{+x}U,0)^2+ \\ \max(D_{xyz}^{-y}U,0)^2+\min(D_{xyz}^{+y}U,0)^2+ \\ \max(D_{xyz}^{-z}U,0)^2+\min(D_{xyz}^{+z}U,0)^2 \end{array}\right]^{1/2} = \frac{1}{F_{xyz}}, \tag{4.3}$$

where D represent the forward and backward differential operators from standard finite difference notation, as in:

$$D_{xyz}^{-x}U = \frac{U_{x,y,z}-U_{x-1,y,z}}{h_x}, D_{xyz}^{+x}U = \frac{U_{x+1,y,z}-U_{x,y,z}}{h_x}$$

$$D_{xyz}^{-y}U = \frac{U_{x,y,z}-U_{x,y-1,z}}{h_y}, D_{xyz}^{+y}U = \frac{U_{x,y+1,z}-U_{x,y,z}}{h_y} \tag{4.4}$$

$$D_{xyz}^{-z}U = \frac{U_{x,y,z}-U_{x,y,z-1}}{h_z}, D_{xyz}^{+z}U = \frac{U_{x,y,z+1}-U_{x,y,z}}{h_z},$$

where *(x,y,z)* in the above equations represent the 3D location indices of a particular voxel, and h_d is the voxel spacing in the corresponding ('d' subscripted) direction. The zeros and min-max operators cause only voxels, whose arrival time value has already been computed, to be considered when solving Eq. 4.3. An easily implemented "upwind" approach [106] was used:

$$\left[\begin{array}{l} \max(D_{xyz}^{-x}U,-D_{xyz}^{+x}U,0)^2+ \\ \max(D_{xyz}^{-y}U,-D_{xyz}^{+y}U,0)^2+ \\ \max(D_{xyz}^{-z}U,-D_{xyz}^{+z}U,0)^2 \end{array}\right]^{1/2} = \frac{1}{F_{xyz}}, \tag{4.5}$$

During the fast marching algorithm, voxels pertaining to the vessel tree may be thought of as having one of the following labels: "frozen" (the arrival time value has been determined for the voxel), "narrow band" (an arrival time value has been computed for the voxel, but the value may not be the voxel's final arrival time value), and "far" (the arrival time has not been computed for the voxel). The algorithm starts from a seed voxel (vessel tree root) and calculates the arrival time outwards, away from the seed voxel. The initial seed voxel is "frozen" and distances to neighbors are computed according to Eq. 4.5. The voxels that are computed are now a part of the "narrow band" voxel list. At each step of the algorithm the "narrow band" voxel having the smallest arrival time becomes "frozen" (removed from "narrow band" list) and the neighbors'

arrival times are updated as long as they are not already "frozen". The algorithm's speed is greatly increased through the use of heap structures (such as heap-sort [107]) that can be used to efficiently keep track of "narrow band" voxels having the minimum arrival time value. The use of heap-sort gives the fast marching method a computational cost of $\mathcal{O}(N\ logN)$, for N voxels within the vascular tree.

One particular difficulty that was overcome was automating the determination of the vascular tree's endpoints (i.e., ends of terminal branch segments). By first propagating a wave with no weighting other than the binary representation of the object, allowed the vascular tree's voxels to be labeled according to their path distance (through the vascular tree) from the vessel tree root. Labeling the background as zeros, the voxel distances were grouped into regions at relatively the same distance (e.g., by normalizing the individual voxel distances to the largest distance and then multiplying by a constant in order to cluster voxels into groups), and the endpoint locations were therefore regional maxima (i.e., the grouping of voxels with higher distance values than their neighbors). Each regional maximum cluster was then searched for a single voxel having the greatest arrival time value. Above a constant multiplier value of 100, the number of endpoints found was observed to plateau (i.e., the same number of endpoints were found) signaling convergence of the endpoint finding process.

The arrival time function, as determined through the fast marching method, can also be thought of as a type of geodesic distance (i.e., the shortest path over a curved surface, in this case the "surface" represented by the spatial distribution of the arrival time value of surrounding voxels) from any voxel to the wave front's source voxel (thus finding the geodesic curve γ from x_0 to x_1 in Eq. 4.1). Propagating a second fast marching wave to map the object in terms of the arrival time (weighted by a squared distance map), geodesic paths (vascular tree centerlines) were extracted by means of solving a back propagation equation [108] (e.g., gradient steepest-descent) of the form:

$$\frac{dC(t)}{dt} = -\nabla U. \tag{4.6}$$

where $C(t)$ is the parametric curve that is used as the object's centerline (with $C(0) = x_1$), and U is the geodesic distance (arrival time function).

Once the path was extracted, any voxel with a path passing through it was labeled.

A weighted comparison between voxels was then used to remove voxels that were not necessary to keep the vascular tree (via one of 26 contiguous neighbor voxels) connected. Taking the extracted paths into a voxel-based representation allowed for later delineation of individual branch segments.

In summary, there were two fast marching waves that were propagated in order to extract the vessel tree's centerline. The first wave acted on a binary representation (i.e., a weight function that was constant throughout the tree). The arrival time function that was found for this first wave was used for determining endpoint locations. The second wave that was propagated acted on a distance map representation of the vascular tree, a map which had its values squared in order to increase the weighting at the center of vessel lumens. This arrival time function was used to extract the centerline paths from each endpoint to the root (i.e., solving Eq. 4.6).

Finally, the process of labeling branch endpoints and bifurcations was automated and individual branch segment voxels (as determined by the extracted centerline) were ordered in a connected voxel list as a pre-processing step to subsequent measurements. This allowed branch segments to be distinguished, labeled, and analyzed individually. The process of automatically labeling the micro-CT vascular tree's centerline in (J,K) notation allowed individual branch segments to be compared with the optical measurements. Due to the fact that some branch segments were physically lost before the micro-CT scan was performed, this matching process was performed visually to account for the lost segments.

4.2.5 Vessel Branch Measurements

Once the vascular tree's centerline was extracted and labeled, measurements of the individual branch segment's length and diameter were performed. The measurement of an individual branch segment's length was determined by moving from one voxel to the next in the list of ordered centerline voxels, calculating the Euclidean distance between contiguous voxels, and summing the distances, as in:

$$L = \sum_{i=1}^{i=n} \sqrt{(x_i - x_{i+1})^2 + (y_i - y_{i+1})^2 + (z_i - z_{i+1})^2}. \tag{4.7}$$

where n is the number of voxels of the branch segment, i is a reference to the voxel at location *(x,y,z)*, and L is the computed length.

Ideally, the length of the branch segment is given by the line integral:

$$L(C) = \int_C ds, \tag{4.8}$$

where ds is the infinitesimal element of length measured along the curve C. The method used here (Eq. 4.7), is essentially the "sample-distance" method [88] where geometrically the curve C is being approximated by the connected polygonal curve whose vertices are the branch segment's centerline voxels. Another method, that of simply counting voxels [73, 109], can significantly under-estimate interbranch segment length. Curve fitting or smoothing (e.g., a moving average filter) could also be performed and would likely be beneficial for characterizing such properties as branch segment tortuosity in order to remove voxel-based artifacts.

Measurements of vessel diameters have received much more attention than length measurements [110]. In numerical modeling of such properties as vessel resistance there is a much stronger dependence on vessel diameter than on vessel length. According to the Hagen-Poiseuille equation [32], the resistance to flow is proportional to length over the diameter to the fourth power, and thus an error of vessel diameter results in a far larger functional impact. Previous methods for measuring vessel diameters can be grouped into four main categories [90]: derivative-based, threshold-based, densitometric, and model-based techniques.

To measure the diameter, a gray scale threshold-based method was developed. For each centerline voxel of an interbranch segment, the nearest non-vessel voxel (nearest-neighbor transform) was determined. A line profile was then computed that started from this non-vessel voxel, intersected the centerline voxel, and ended once another non-vessel voxel was reached. The profile length was calculated for two different gray scale thresholds (1300 and 1500) about the FWHM value (max gray scale $\approx$2800) and an average was taken. The average length of this profile (as computed for each centerline voxel) was used as an individual interbranch segment's diameter. Since a far lower threshold than the FWHM of the casts was initially chosen in order to extract small vessel segments, small vessel diameters were corrected as discussed below.

4.2.6 Compensating for Micro-CT MTF

To correct for the modulation transfer function (MTF) of our scanner we also analyzed the effect of vessel blurring in order to correct for the over-estimation of small branch segments. Figure 4.3 depicts CT image brightness line profiles through different-diameter branch segments. The ideal profile would be a square wave. As vessel segment diameter decreases, a significant decrease in the peak gray scale value, as well as broadening of the profile relative to the vessel diameter, was observed. The point spread function derived from the MTF was a quasi-Gaussian blurring function with a 30μm standard deviation [111] (0.07mm FWHM). Displayed in Figure 4.4 is a schematic of two different diameter input square waves, or line profiles (dashed line), along with the line profile that occurs in the image due to blurring (solid line). Large diameter vascular segments' diameters are accurately represented by their FWHM profile, however small segments are not. As the vessel's diameter decreases, the output signal becomes broader (with respect to the true diameter) and the peak output signal decreases. This concept is further elaborated on in Figure 4.5. Displayed in the top panel is a plot of the theoretical peak gray scale values' dependence on vessel diameter, and the bottom panel displays the full-width-half-max of the output signal, with respect to the input (ideal) vessel's square wave profile. The experimental results show that vessel diameters below 0.1mm were significantly over-estimated due to blurring, which matches our theoretical prediction. These branch segments' diameter measurements were corrected by fitting a Gaussian distribution function to the line profiles and then computing the input square wave (segment diameter) that was convolved with the imager's blurring function to give such a profile. This was derived on the basis that the area under the blurred image is equivalent to the actual input square wave's area. These line profiles were extracted as discussed previously, using the nearest-neighbor transform (nearest non-vessel voxel) computed from the original vascular tree segmentation (i.e., the segmentation used to extract the centerline).

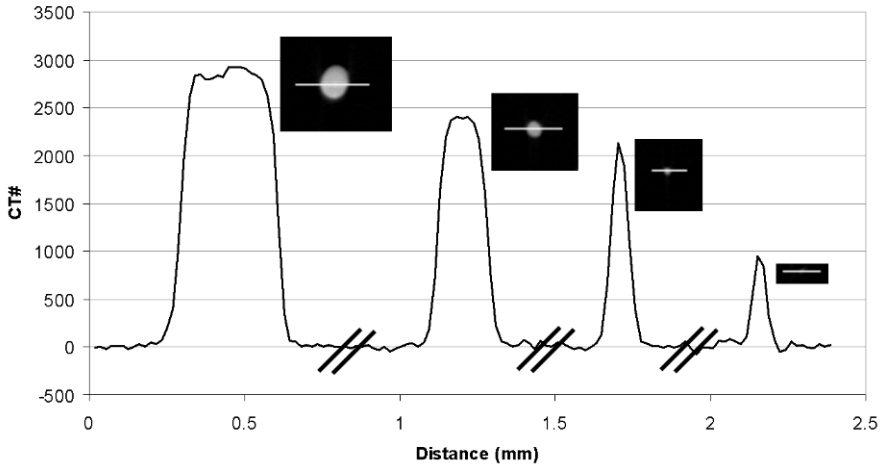

Figure 4.3: Line profile of varying diameter branch segments. The y-axis is in units of 1000cm^{-1}. Larger diameter segments retain to a great extent the ideal square wave profile. As the branch segments decrease, significant reduction in peak gray scale is observed. From [76].

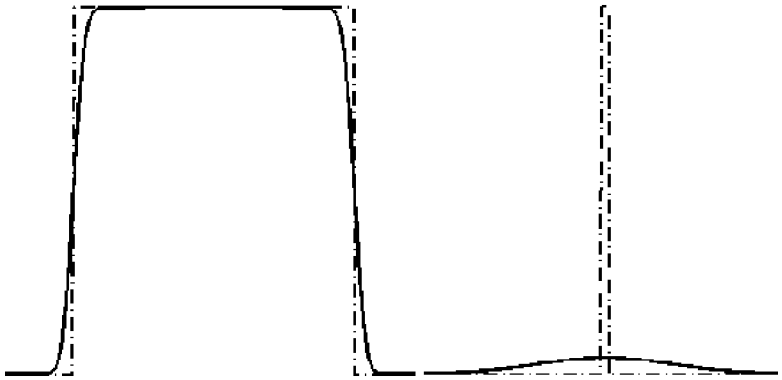

Figure 4.4: An illustration of the image blurring process. The modulation transfer function of the micro-CT scanner is a Gaussian blurring function. This blurring function is convolved with the vessel's true cross-sectional profile (dashed line), resulting in the blurred output (solid line). For large diameter vascular segments (left), the full-width-half-max of the line profile accurately characterizes the true diameter. For small vessel segments (right), equating the area under the blurred profile to that of an equal area square profile, with peak gray scale height equal to that found in large vascular lumens, allows for the accurate measurement of small vessel segment diameters. From [76].

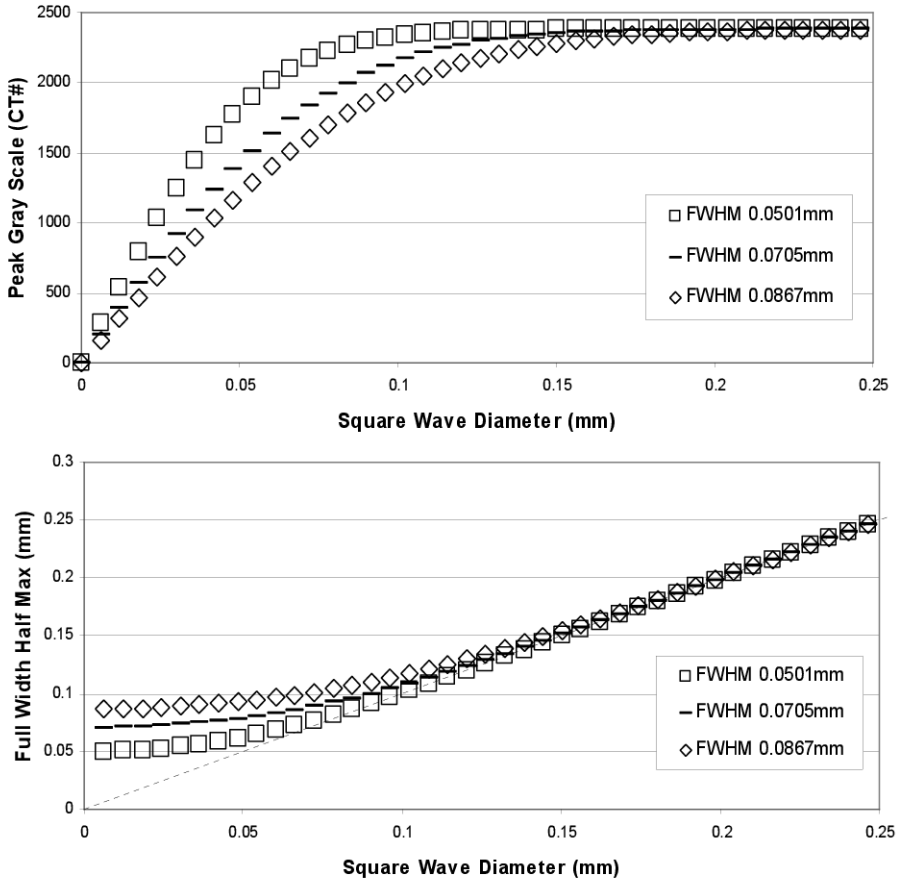

Figure 4.5: A plot of the theoretical gray scale values' dependence on vessel diameter (top panel), for three different scanner blurring function widths. Vessel segments with small diameters will have a significantly reduced peak gray scale value. This is also dependent on the modulation transfer function of the imaging system. The full-width-half-max of the output signal with respect to the input (ideal) vessel's square wave profile is also shown (bottom panel). Large vessels' diameters can thus be accurately measured but small vessels' diameters will be overestimated. This deviation occurs at about 0.1mm, with increasing severity as the vessel segment diameter decreases. From [76].

4.3 RESULTS

Compared with the months spent analyzing the casts by optical measurements, the micro-CT scanning, reconstruction, and image analysis each took a few hours to complete. The centerline extraction and individual branch measurement algorithms, fully automated, ran in under 10 minutes for both specimens (non-optimized code). Figure 4.6 displays the computed centerline superimposed on the segmented image of the vascular tree (*h61*), and Figure 4.7 depicts zoomed-in views of two particularly critical areas. These areas highlight the ability of the centerline extraction method to follow the centerline paths within tortuous branches, as well as distinguish between branch segments that have some degree of overlap due to blurring. Note that the tree endpoints are followed all the way to their ends, there are no false branches ("whiskers") within the larger vessel lumens, and the centerlines are well centered within the lumens. In the case of physically missing large branch segments (i.e., broken), the extracted centerline still retains the information pertaining to the remaining 'stump' and thus the tree hierarchy is well preserved. Figure 4.8 depicts the extracted centerline along with the semi-transparent 3D volume rendering of *r14*.

Shown in Figure 4.9 are the results for individual branch segments' diameters and lengths in the form of a regression plot comparison for *h61*. In the top panel (diameters), the corrected and non-corrected results are given. The non-corrected result agrees with our expectation, that small vessel diameters are over estimated. This is also represented theoretically in the bottom panel of Figure 4.5. In the case of the diameter measurements, the standard deviation of the difference between optical and micro-CT measurements (13μm) is within the theoretical voxel resolution of the micro-CT images (voxels are 18μm to a side). By developing a method to correct for the over-estimation of branch segments with small diameters, an improvement of the regression analysis resulted. Also, the method is valid over a wide scale-range, with diameters spanning 12-338μm, and lengths spanning 14-3,159μm. Figure 4.10 displays the same regression analysis performed for specimen *r14*. The closer to ideal 1:1 relationship for the diameter regression analysis of *r14* shows that the developed micro-CT measurement method is accurate for an even larger range of interbranch segment diameters.

Figure 4.6: Extracted centerline shown superimposed on the volume rendered display of the vascular tree *h61*. Arrows indicate regions highlighted in zoomed-in views displayed in Fig. 7. From [76].

Figure 4.7: Zoomed-in views of the vessel tree displayed semi-transparently, with the corresponding extracted centerline. Left image displays path centered-ness along a particularly tortuous branch segment, as well as the ability of the centerline extraction method to follow segments to their endpoints. Image on right depicts the ability to delineate overlapping branch segments, and also extract small terminating segments. From [76].

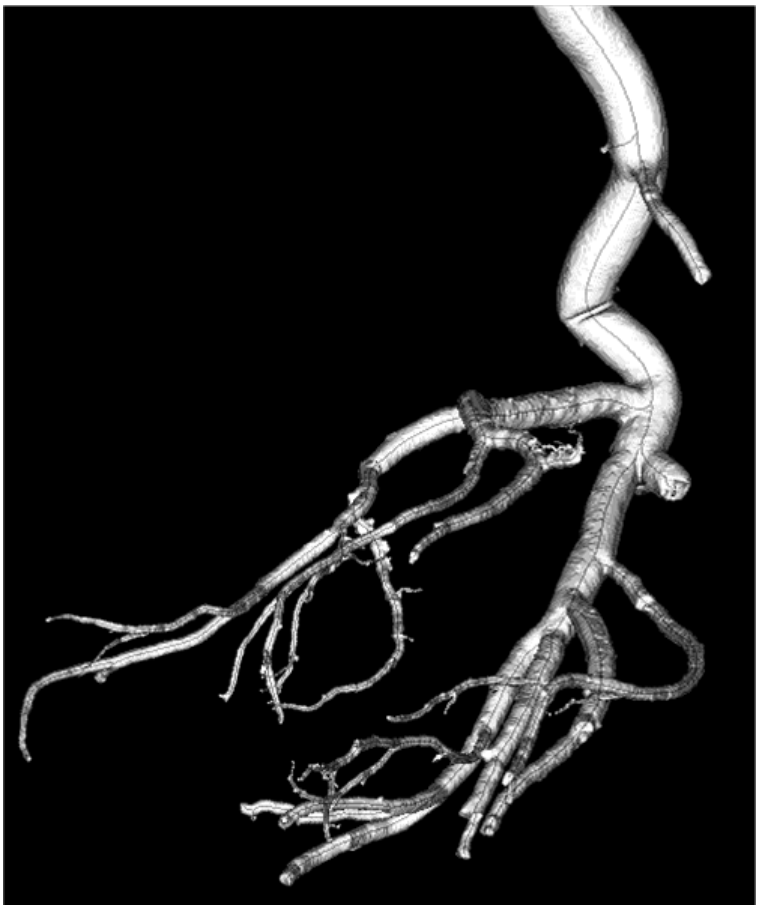

Figure 4.8: The centerline extraction method also has the ability to handle complex vascular structures as is shown here with the centerline superimposed on the volume rendered display of the vascular tree *r14*. From [76].

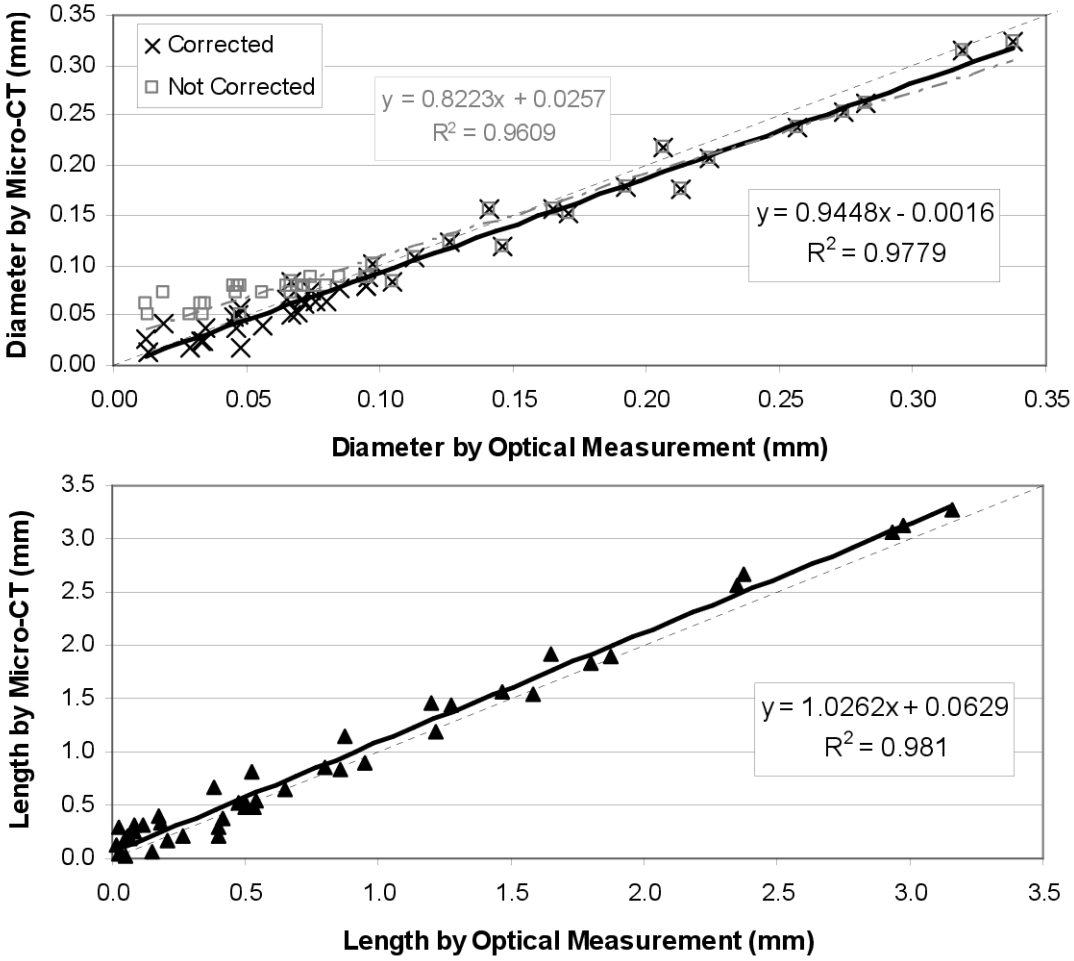

Figure 4.9: Regression plots for individual branch segments diameter (top) and length (bottom) measurements of specimen *h61*, by the micro-CT (y-axis) and optical (x-axis) measurement methods. Solid black line depicts linear least squares fits to the data. Dotted lines are 1:1 values. The corrected (black x's) and not corrected (gray squares) diameter measurements are both shown in the top panel. Vessel segments with diameters below 0.1mm were measured much larger by micro-CT. These small segments measurements were significantly improved by compensating for the imager's modulation transfer function. From [76].

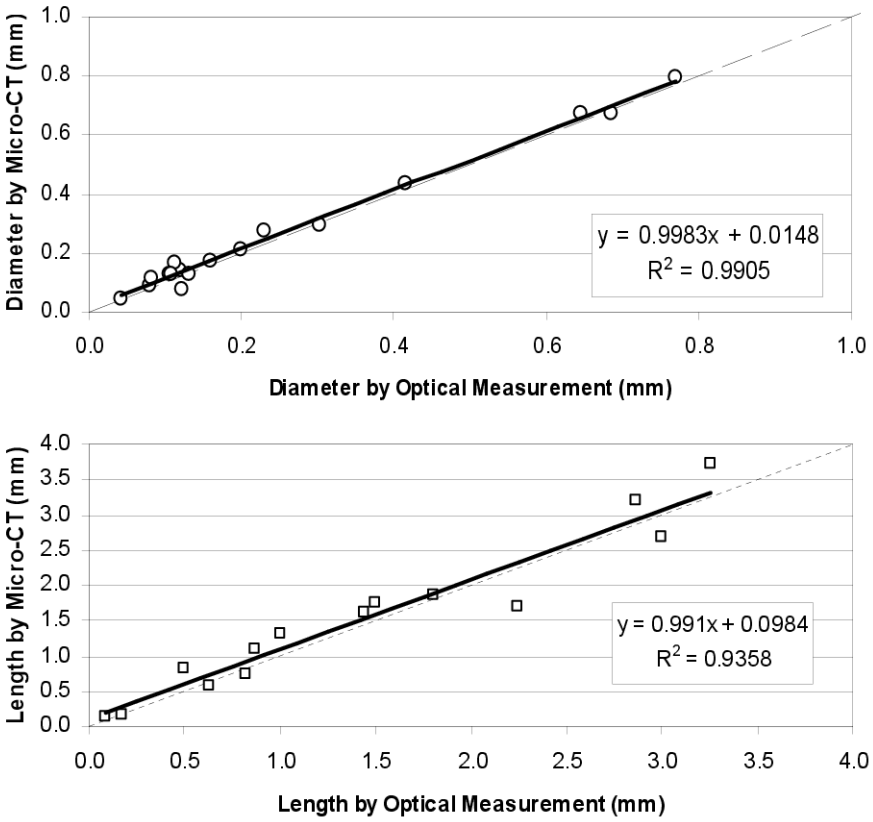

Figure 4.10: Regression plots for individual branch segments diameter (top) and length (bottom) measurements of specimen *r14*. Solid black line depicts linear least squares fits to the data. Dotted lines are 1:1 values. From [76].

To further quantify the individual branch segment comparison, the results for specimen *h61* were plotted in a Bland-Altman comparison [112] which assumes that neither method necessarily gives the correct measurement but shows how well the two measurement methods compare. Figure 4.11 shows these results, along with the mean value and 95% confidence intervals for the difference between measurement methods, which is calculated as $mean \pm 2 \times standard\ deviation$. The mean diameter difference is 8μm (micro-CT measured slightly smaller than optical measurements) with 95% confidence interval -34 to +18μm. The mean length difference is 85μm (optical measurements measured slightly smaller than micro-CT) with 95% confidence interval -171 to +341μm. Combining the results from both casts, the standard deviation of the difference between measurement methods was 19μm for the measurement of interbranch segment diameters (for 60 segments between 12 and 769μm in diameter). Also, the standard deviation between measurement methods was 172μm for the measurement of interbranch segment lengths (between 14 and 3,252μm in length). The larger difference for the case of individual branch segment lengths stems from a few issues. Probably the largest factor is that the definition of a "bifurcation point" is somewhat subjective during the optical measurement. The designated location of this intersection will affect all three branch segments' length measurements (i.e., parent and two branches). This error resulting from different bifurcation points is reduced if we consider multiple sequential segments (i.e., a single path through the tree). Comparing the longest path through the tree (i.e., a summation of the individual branch segment lengths) resulted in a percent difference between the optical and micro-CT measurements of only 5%. This was calculated from

$$D = 100\% \times \frac{|O_l - M_l|}{O_l} \tag{4.9}$$

where D is the percent difference, O_l is the length measured by optical measurements, and M_l is the length measured by micro-CT.

The introduction of the small vessel correction allowed small vessel diameters to be accurately measured. In the works of [113, 114], approximately 1.5 voxels was determined to be the limit of accuracy for the estimation of vessel radii. For our current investigation of specimen *h61*, 12 out of the 43 individual branch segments are smaller than this value for their optically measured diameter (i.e. the optical method measured

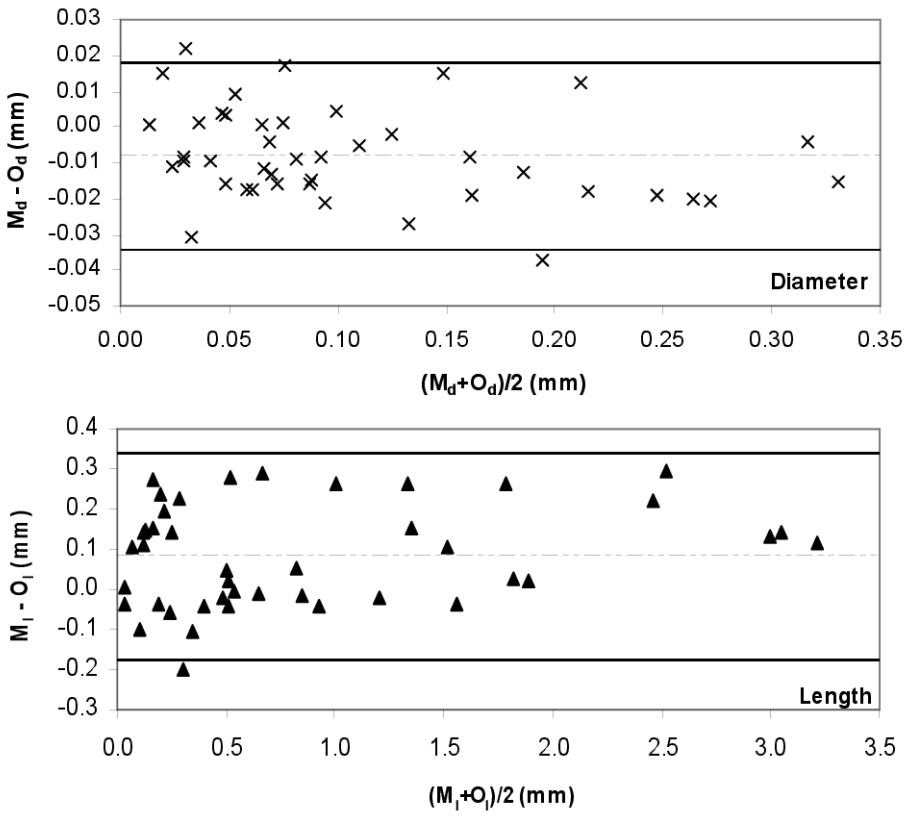

Figure 4.11: Bland-Altman method [112] comparison analysis for both interbranch segment diameter (top) and length (bottom) of specimen *h61*, by the micro-CT (M_d and M_l, respectively) and optical (O_d and O_l, respectively) measurement methods. Dashed black line is the mean offset between measurement methods and dotted lines are the 95% confidence intervals for the difference between measurement methods. From [76].

a diameter below 54μm). The proposed correction method allowed for a significant increase in the accuracy of small vessel diameter measurements, improving the average percent difference from 129% for the non-corrected measurements to 38% for the corrected measurements. Also, for the non-corrected diameter measurements, an average difference between the micro-CT measurement and the optical measurement was 1.68 voxels. For the corrected measurements this value was reduced to just 0.58 voxels, meaning that we were able to measure the diameter of small interbranch segments to within approximately half a voxel.

4.4 DISCUSSION

The use of the "fast marching" method for centerline extraction is an active research area [81, 82, 97]. The advantage of this method for our purpose is that the flow pathways are of particular interest in our application. Here the focus is on finding the centerline paths through the vessels as opposed to two other skeletonizing methods: (i) iterative thinning [79, 115] (i.e., peeling away surface voxels) and (ii) mesh contraction [80] (i.e., shrinking). Thinning methods suffer from whiskers and shortening of branch segments (a consequence that is accentuated for thicker branch segments). Shown in the left panel of Figure 4.12 is the result of applying morphological thinning to *h61* as the means of forming a skeleton. Major problems of note are that larger diameter segments are significantly truncated (centerline does not extend to branch segments' ends), overlapping vessels are not well delineated, loops are formed, false branch segments are generated (whiskers), and the centerline is very noisy and does not follow curved segments well. The other method of mesh contraction requires conversion from a voxel-based representation into a mesh-based representation, and also requires many update steps for centering and correcting skeletons. Shown in the right panel of Figure 4.12 is the result of applying a mesh contraction method to specimen *h61*. Major identifiable problems include strange bifurcation representations by the centerline, poor overlapping segment delineation, and problems identifying small vessel segments (particularly broken segments).

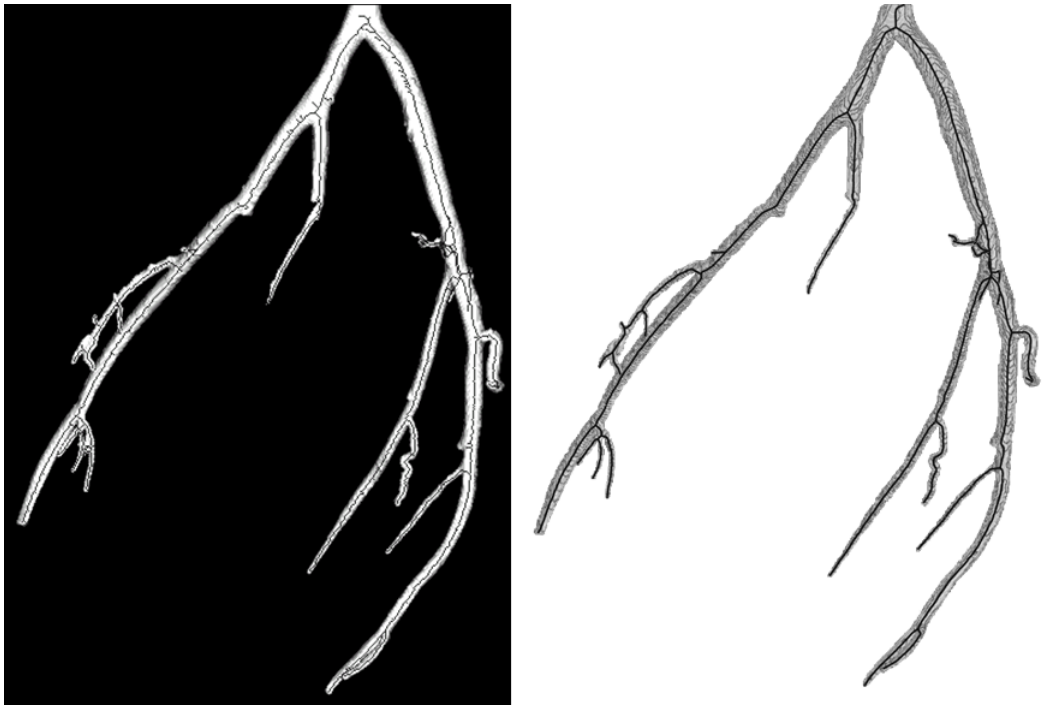

Figure 4.12: Left panel (black background): The result of applying morphological thinning to *h61*. Major problems include the truncation of larger diameter segments (centerline is shorter), overlapping vessels are not well delineated, loops are formed, false branch segments are generated (whiskers), and centerline is very noisy and does not follow curved segments well. Right panel (white background): The result of applying a mesh contraction method to specimen *h61*. Major problems include strange bifurcation representations by the centerline, poor overlapping segment delineation, and problems identifying small vessel segments (particularly broken segments). In addition, mesh contraction requires conversion from a voxel-based representation (into a mesh-based representation) and also requires many update steps for centering and correcting skeletons. From [76].

It is well known that by using a weighting function that is a constant value inside the object (i.e., the object's binary representation) for the fast marching wave propagation, the "shortest path" will cut corners and will not be centered (i.e., the path will be the shortest 'Euclidean' geometric distance). It has been shown [81] that applying a weight function corresponding to the distance map within an object caused the paths to retain some amount of centered-ness in binarized images of brain vessels. The weight function assigned to each vessel voxel was a value corresponding to the inverse of that voxel's distance to its nearest non-object voxel neighbor. The result was that the fast marching wave propagated more quickly at the vessel lumen's centers (i.e., the wave front reached those voxels faster), so that the extracted "geodesic" path was constrained from cutting corners.

In addition to single path centered-ness of microvasculature, the path centered-ness within bifurcations is very important because measurements of branching angle and lengths are significantly affected on this scale by the accuracy of the branching geometry. Dependent on branching angles and the cross-sectional eccentricity of the bifurcation, stronger weight functions may be necessary in order to cause extracted centerlines to pass through the true junction point. The drawback of using stronger weight functions is an increase in the sensitivity to the surface irregularities (usually due to noise in image gray scale) of the vessel tree, as well as possible numerical inconsistencies which are problematic during the sub-voxel precise gradient-descent step. A discrete gradient-descent along a voxel's 26 contiguous-voxel neighborhood increases this problem at bifurcations, and therefore requires even stronger weighting functions.

The developed centerline extraction method is fully automated and is computationally efficient, overcoming computationally expensive fast-marching-based methods seen in such work as in [82] where fast marching wave propagations are calculated for each endpoint that is determined, and in which there is a criteria set on branch lengths in order to exit the iterative algorithm. In the case of *r14* this would have resulted in up to 60 fast marching waves (versus the two proposed in this work), while potentially still missing shorter branch segments. Also, for our present application, such methods as using gradient vector flow [97] to define the object's centerline is unnecessary as the vessel pathways are highly tubular and thus the less computationally expensive distance map is beneficial. To compute the gradient vector flow field for *h61* took 40 minutes as

opposed to the 13 seconds spent computing the distance map. Additionally, for large vessel trees the gradient vector flow field becomes very memory-intensive since it relies on the use of three cardinal direction gradient maps, typically at double floating point precision. Due to many factors such as: (i) the high level of image analysis throughput of our lab, (ii) that our intention is to apply our analysis methods to far larger image volumes, and (iii) the fact that no major benefits in the extracted centerline were observed when a gradient vector flow map was used, a faster, less memory intensive method will be highly beneficial at little to no expense in the subsequent data's accuracy. However, it should be noted that such a weighting map (such as the gradient vector flow field) is useful for irregular pathways, or pathways deviating greatly from circular lumenal cross-sections, as it has the ability to distinguish the center of mass of such cross-sections as an oval or rectangle (for instance), whereas a distance map may have a string of voxels, all at the same value.

Using the binary representation of the object for automated endpoint determination resulted in the endpoints being followed to the correct ends, and was far less sensitive to the noisiness (i.e., roughness) of the vascular tree's surface, compared with a similar method. This similar method, termed the level set graph [97], utilizes a distance map weighted representation of an object to determine endpoints. This method, we found, did not converge on a specific number of endpoints and was also highly sensitive to the chosen cluster size. In the case of a distance map weighting, the number of endpoints was not found to converge, meaning that increasing the 'constant multiplier' resulted in more and more endpoints being (falsely) identified. These were found to exist on the wall of interbranch segments, not necessarily at the ends of the vascular tree. Intuitively this makes sense since the distance map weighting introduces a strong gradient moving away from the center of vessel lumens towards the wall.

In regards to vascular segment diameter measurements, a detailed study was performed by Hoffmann et al. that compared various techniques for determining vessel diameters [90]. These techniques included derivative-based, threshold-based, densitometric, and model-based methods. The study was performed on simulated images, as well as a vessel phantom, composed of distinguished cylindrical objects (i.e., non-bifurcating structures.) The main conclusion was that no technique perfectly characterized vessels over the full size range. However, large vessel segments with diameters larger than

the FWHM of the imaging systems blurring function (or simulated blurring function), were found to be accurately measured (errors of ≈0.1 mm) using an averaging of the first and second derivatives of vessel line profiles. Theoretically the second derivative method is guaranteed to always over-estimate vessel diameters, while the first-derivative as well as the FWHM accurately characterize the input square wave's width (for large diameter vessel segments). Our method of measurement accurately measures large diameter vessel segments, and is fully automated. Also, small diameter branch segments were accurately measured by using local gray scale information to take into account the imaging system's blurring properties.

The micro-CT method is a far faster analysis method that limits the effects of manual error introduced by the tedious, optically based measurement method used in this work and others. Also, the micro-CT method extracts 3D information (such as bifurcation points), which differs from the 2D information contained in optical measurements. Since the accuracy of the micro-CT method of analysis has been characterized, showing favorable results, we are able to validate alternative methods of analysis [63], and will be able to compare the branching geometry of different vascular structures (e.g., the portal vein, hepatic artery, and biliary tree of the liver).

4.5 CONCLUSIONS

An important tool for providing information pertaining to a vascular tree's contribution to various diseases and organ malfunctions is the image analysis of microvasculature. In contrast to the imaging of organ tissues, which typically focuses on topology and variable intensity within that organ, the imaging of vasculature requires a focus on vascular branching architecture. The goal of this work was to highlight some key difficulties in this area of analysis such as: imaging resolution, segmentation, centerline extraction, as well as the measurement strategy of individual branch segment's lengths and diameters. The comparative results presented are positive and suggest that a method of characterizing microvasculature tree structures can be accomplished by micro-CT, which is beneficial since the time scale of such an analysis is far faster and less prone to errors

than a tedious method, such as the optical measurement of individual branch segments (i.e., the gold-standard used in this study).

Chapter 5

Comparison of Measurement Strategies for Vascular Characterization

5.1 INTRODUCTION

To date there appears to be no single image analysis algorithm that can automatically perform accurate direct dimensional measurements over the wide-scale range of vascular tree structures. This is because 3D image analysis of vascular trees presents many image processing challenges. Such challenges include the fact that there are more than 18 branching generations between a 1mm diameter artery and a 5μm diameter capillary as well as blurring of the 3D image which disproportionately affects smaller interbranch segments. Additional problems include the accurate segmentation of the vascular tree [75], extracting information regarding the tree's hierarchical structure [98], and measuring the dimensions of individual branch segments [90]. The study of microvasculature branching geometry's role on the spatial heterogeneity of perfusion distribution has

This chapter was modified from the original conference proceedings paper: **TL Kline, Y Dong, M Zamir, and EL Ritman. Erode/Dilate Analysis of Micro-CT Images of Porcine Myocardial Microvasculature.** ***Proceedings of the SPIE*****, 7626:762620-1–762620-9, 2010.** and reproduced by permission of the publisher: SPIE (see **Chapter A**)

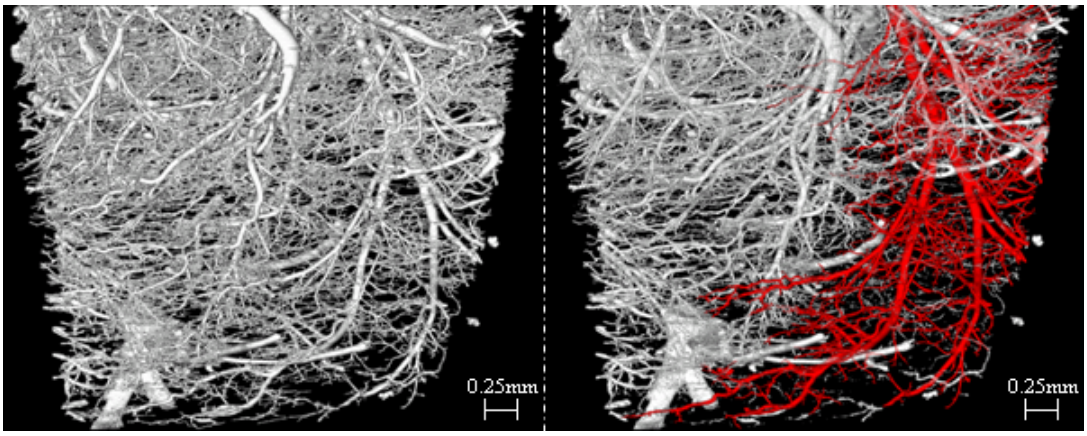

Figure 5.1: Computer generated display of a volume rendered 3D micro-CT image of the microvasculature within porcine myocardium. The vessel lumens are filled with a radiopaque Microfil polymer. Left panel: entire biopsy volume. Right panel: individual tree (red or dark gray) isolated from the image data in left panel. The volume rendering is displayed semi-transparently to allow a clearer visualization of the isolated tree. From [63].

been addressed by a number of investigators [9, 91, 92]. The analysis of intact vascular trees over a wide range of scales is necessary in order to detect early changes in branching geometry of microvasculature as well as study the associated impact on the perfusion distribution in diseases in which different branching generations are affected differently [116]. Micro-CT offers an excellent framework from which to analyze intact microvascular beds, and a sequential 'erode/dilate' technique [84] which progressively eliminates branches of increasing diameter is one approach that greatly reduces image analysis effort. By this method, the total luminal volume of different diameter branches is calculated.

5.2 METHODS

5.2.1 Sample preparation and micro-CT scanning

This study was reviewed and approved by the Mayo Clinic College of Medicine's Institutional Animal Care and Use Committee (IACUC) in accordance with the National Institute of Health Guidelines. The control and embolized samples were obtained from

female domestic pigs. The embolized specimens differed from the control in that an injection of non-radioactive microspheres into the LAD was performed. The pigs were then euthanized and the hearts harvested. The coronary arteries were infused with Microfil polymer (Flow Tech, Inc., Carver, Massachusetts) at 100mmHg infusion pressure and a nominal 2cm^3 transmural "biopsy" of the myocardial region was collected after the Microfil injection. An example of a microvascular bed is depicted on the left panel of Figure 5.1. See [13, 117] for more details on the bench-top (20μm voxel) and Brookhaven National Laboratory (4μm voxel) micro-CT imaging methods used.

5.2.2 Erode/dilate analysis

The morphological operations of successive erosion and dilation [86, 87] were used to characterize the tree branches, similar to the method used in [84, 85]. Briefly, the method eroded and then dilated the vessel tree volume 'n' number of times, where 'n' was the iteration number. Both the erosion and dilation operations were performed by analyzing an individual voxel's 6-connected neighborhood. Thus for voxel $v(x, y, z)$ it's 6-connected neighbors are located at

$$v(x \pm 1, y, z), v(x, y \pm 1, z), v(x, y, z \pm 1). \tag{5.1}$$

For the erosion step, a vessel voxel $v(x, y, z) = 1$ was turned into a non-vessel voxel $n(x, y, z) = 0$ if any voxel in it's neighborhood was a non-vessel voxel (thus voxel $v(x, y, z)$ was located on the surface). For the dilation step, a non-vessel voxel was turned into a vessel voxel if any of it's 6-connected neighbors were a vessel voxel. We did not use other voxel connectivities, such as a voxels 18 (face + edge) or 26 (face + edge + corner) nearest neighbors, because these tend to misrepresent vessel diameters by removing a greater number of surface voxels, thereby incorrectly conveying vessel volumes. After each iteration the total vessel volume was measured. The results were then binned according to the vessel volume 'V' that was lost (i.e., $V(n-1) - V(n)$) by removing individual branches $2nh$ in diameter ('h' is the voxel size). This method was performed on both the entire vascular bed and the individual tree.

To reduce processing time it was noted that an 'n' iteration erosion is equivalent to thresholding a 'city-block' distance map. The 'city-block' distance map was calculated

once and any 'n' iteration erosion computed in one pass over the distance map volume. The 'city-block' distance map assigns all non-vessel voxels a value of zero and all vessel voxels a value corresponding to their distance to the nearest zero voxel. Differing from the true Euclidean distance, the 'city-block' distance is always an integer as only movements in one cardinal direction at a time are allowed. Therefore, the 'city-block' distance map is the shortest path from each vessel voxel to the nearest non-vessel voxel along a 6-connected neighborhood path. This distance is known as the L_1 distance in which the distance between two points is the sum of the absolute differences of their coordinates, as in

$$L_1(\vec{v}, \vec{n}) = \|\vec{v} - \vec{n}\|_1 = \sum_{i=1}^{n} |v_i - n_i|, \tag{5.2}$$

where $\vec{v} = (v_x, v_y, v_z)$ is a vessel voxel (i.e., $v(x, y, z) = 1$), and $\vec{n} = (n_x, n_y, n_z)$ is the nearest non-vessel voxel to $\vec{v}$. Therefore, the voxels remaining after an 'n' iteration erosion are the same as those with a 'city-block' distance map value greater than 'n'.

5.2.3 Model vascular tree

For the purpose of illustrating the difference between knowing both the dimensions and interconnectivity of a vascular tree and knowing just the erode/dilate analysis data we assume that the vessel tree bifurcates symmetrically at each branch point. The "level" (or generation) of the branches is one higher than that of their parent branch segment. The radii of the branches (r_1 and r_2) are related to the parent segment's radius (r_0) by

$$r_0^k = r_1^k + r_2^k, \tag{5.3}$$

where k is the junction exponent and under the framework of Murray's cube law [8] $k = 3$. Also, in our model, $r_1 = r_2$. Shown in Figure 5.2 is the radius of interbranch segments for 30 steps down a Murray-type tree. The radii were normalized to the root segment. In our erode/dilate method we measure the volume of vessels having different diameters. In the Murray model, with $k = 3$, the total vessel volume for each generation is the same. The diameter "bins" produced by the erode/dilate method do not correspond to diameter increments as described by Murray [8] and others. The

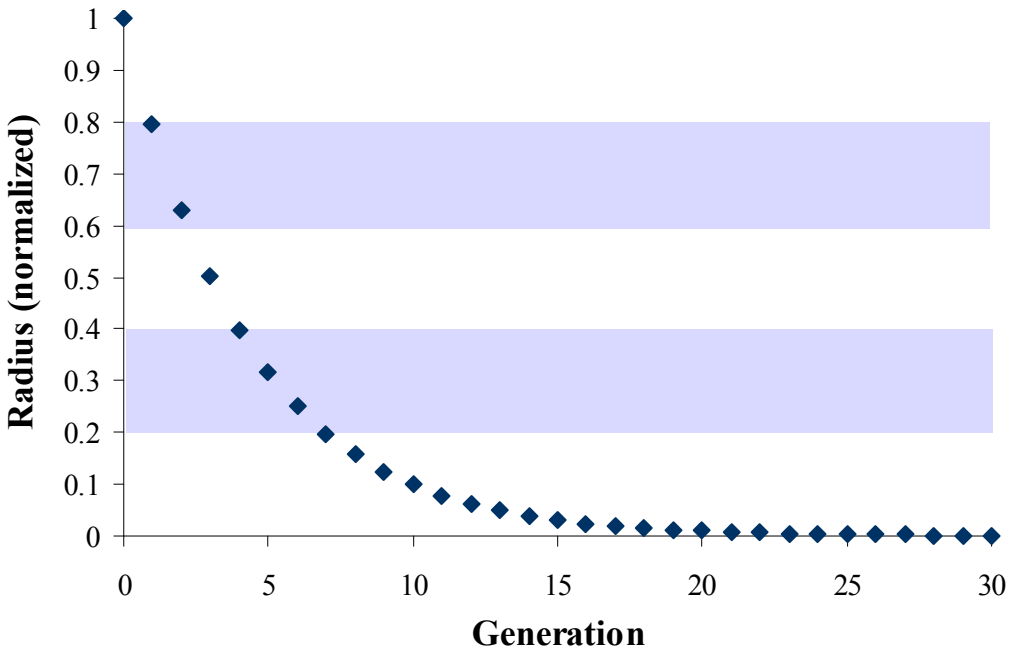

Figure 5.2: Radius increments of an hypothetical Murray-type tree, found by solving Eq. 5.3 for 30 different generations (generation 0 = root segment) with junction exponent $k = 3$. The radius was normalized by setting the root segment radius equal to unity. The alternating horizontal background shades represent the different radius "bins" that each generation's volume is put into by the erode/dilate method. Here the bin size is 0.2 (see Figure 5.3). Therefore, generations with vessel radii between 0 to 0.2 are put into one bin, 0.2 to 0.4 another, and so on. The bins containing the smaller radius vessel segments contain more generations. From [63].

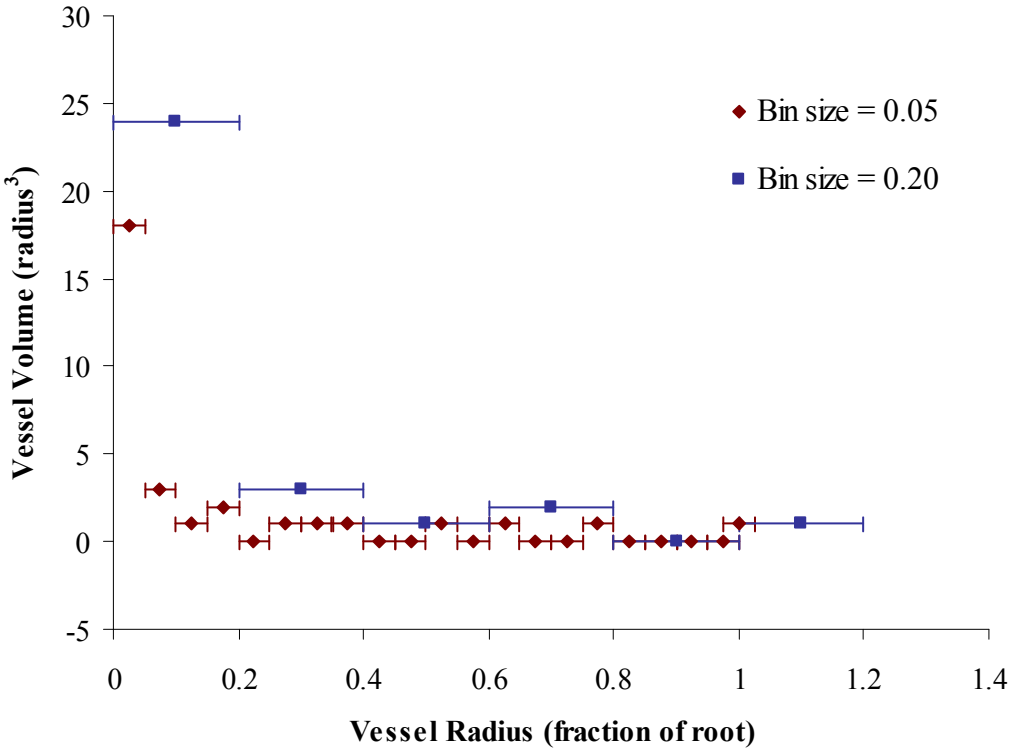

Figure 5.3: The vessel volume distribution calculated for the Murray-type tree, binned according to the erode/dilate analysis method. Two different bin sizes are shown depicting how the results also depend on bin size. Here, each generation has a total vessel volume equal to unity. The horizontal bars surrounding each data point represent the bin size. From [63].

erode/dilate method has equal sized bins, and therefore at smaller vessel diameters more generations have vessel diameters falling within the same bin, causing the observed increase in vessel volume. In addition, if we consider the ideal Murray-type tree, the vessel volume distribution will alias and result in fluctuations caused by finding more or less vessel segments in each bin. The theoretical result for a Murray-type tree, and the erode/dilate data that would result is given in Figure 5.3.

Another problem with the erode/dilate method has to do with the inherent heterogeneity of the vascular tree (i.e., the two branches bifurcating from a larger segment generally have different diameters). At each step of the erode/dilate process we remove

vessels of the same diameter, but these vessels actually come from different levels of the hierarchical tree structure. The positive aspect of this characteristic is that when the microspheres are injected, they too will occlude same-diameter branches at different levels of the tree.

The last notable problem is that when applying the erode/dilate method to a vascular bed we will also be dealing with more than one vascular tree. If the microspheres are injected into the vascular bed via one root segment they will only affect part of the vascular bed, thereby "diluting" the detectable signal from the microsphere embolization.

The effect of an embolization is expected to decrease the vessel volumes found at small vessel diameters. As shown in Figure 5.4 microspheres trapped in vessels having a diameter smaller than T_t will result in a sharp decrease in the volume of vessels found in smaller diameter bins. Since not all of the vessels of a certain diameter are blocked with microspheres, after this initial decrease in vessel volume, the non-embolized vessels' volume should still follow the distribution of the control sample. Thus the difference between the vessel volumes found in the control specimen and the embolized specimen should be a constant below this trapping threshold (in this example those vessels having diameters smaller than T_t).

5.2.4 Individual tree segmentation

A binary file was first computed from a thresholding of the gray-scale 3D micro-CT images. Nearly all of the background image noise was removed by this technique because the signal (i.e., the gray scale of the lumens) and the background were divided into two "well separated" distinct gray scales. The vessel trees were extracted from the binary image by means of a region-growing segmentation method to include those voxels, with gray scale values above the thresholded range, that were connected to the vessel tree's root which was initially identified by visual inspection. Starting at that root, the region-growing method resulted in a single connected tree structure as shown in the right panel of Figure 5.1.

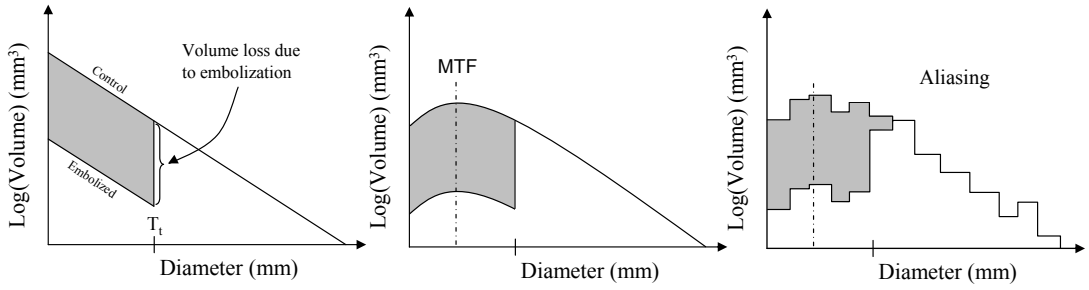

Figure 5.4: A schematic representation of the expected impact of the erode/dilate analysis when microsphere embolization blocks a proportion of vessel segments below the microsphere diameter. The total vessel volumes for vessel diameters below the trapping threshold T_t of the microspheres will be significantly reduced (left panel). This reduction will essentially cause a constant decrease in the total vessel volume in each diameter bin. In addition, the modulation transfer function (MTF) of the imaging system will disproportionately blur small vessels, causing less small diameter segments to be found in the image (middle panel). Finally, the erode/dilate 'bin' sampling does not correspond to the diameter increments of individual generations therefore the data is aliased (right panel). From [63].

5.2.5 Direct measurements

To measure the individual tree by direct measurement the centerline of the vessel tree was first found from the binary volume data set. Following the centerline extraction, measurements of individual branch lengths and volumes were performed. Finally, the results were binned in order to mirror the erode/dilate method of analysis, whereby the total volume of vessels at each diameter bin was derived. The centerline extraction and individual branch segment measurement methods are discussed in the following sub-sections.

Centerline extraction

The binary volume data set of the individual segmented tree was used as the input for the extraction of the vessel tree's centerline. Using locations along the centerline within the segmented image, the tree's hierarchical structure, branch lengths and branch volumes were determined. The centerline was found utilizing the method discussed in

Figure 5.5: Volume rendering of 3D image data of centerline (red or dark gray) as extracted from an example vessel tree (light gray and transparent). This tree was not used for analysis due to its limited number of interbranch segments but rather here for visualization of the accuracy of the extracted skeleton. From [63].

Chapter 4. Figure 5.5 displays a detail of an individual vessel tree centerline extracted by this method, visualized with the actual vessel tree displayed semi-transparently. This individual tree was extracted from the control sample and is here used to display the effect of our centerline extraction method. Finally, the process of labeling branch endpoints and bifurcations was automated and individual branch segment voxels were ordered in a connected voxel list in order to perform individual branch segment measurements.

Individual branch segment measurements

Once the vessel tree's centerline was extracted, measurements of the individual branch segments length and diameter were performed. The measurement of an individual branch segment's length was determined by moving from one voxel to the next in the list of ordered centerline voxels, calculating the Euclidean distance between contiguous

voxels, and summing the distances, as in:

$$L = \sum_{i=1}^{i=n} \sqrt{(x_i - x_{i+1})^2 + (y_i - y_{i+1})^2 + (z_i - z_{i+1})^2}. \tag{5.4}$$

where n is the number of voxels of the branch segment, i is a reference to the voxel at location *(x,y,z)* and L is the computed length.

To measure the volume of an individual branch segment, the number of voxels pertaining to each segment was determined. From this volume individual branch segment's average radius was computed as

$$r = \sqrt{\frac{V}{\pi l}}, \tag{5.5}$$

where V is the volume, and l is the length, of an individual branch segment. Using this volume-based approach guaranteed that the total vessel volume of both the erode/dilate method and the direct measurement method would be computed the same way.

5.3 RESULTS

Figure 5.6 displays the vessel volume to vessel diameter relationship in control samples. The analysis of the micro-CT images of the biopsies involved erode/dilate analysis of the opacified vessels in the entire biopsy and of just one vascular tree in that biopsy. This isolated tree was also analyzed by direct measurement of all the branches' segmental volumes. The regressions of these data (given in Table 5.1) show that all three methods provide similar relationships between the volume of vessels for each diameter.

Figure 5.7 shows the impact of the embolization. To account for the volume difference between specimens, the control and embolized specimens vessel volumes, for diameters above 60μm, were normalized to each other. From the data of Figure 7 the fractional vessel volume loss due to embolization was calculated and given as: (i) 41.8% for the erode/dilate method applied to the entire biopsy, (ii) 48.8% for the erode/dilate method applied to the individual selected tree within the biopsy, and (iii) 43.5% by dimensional measurement of every interbranch segment in an isolated tree within the biopsy.

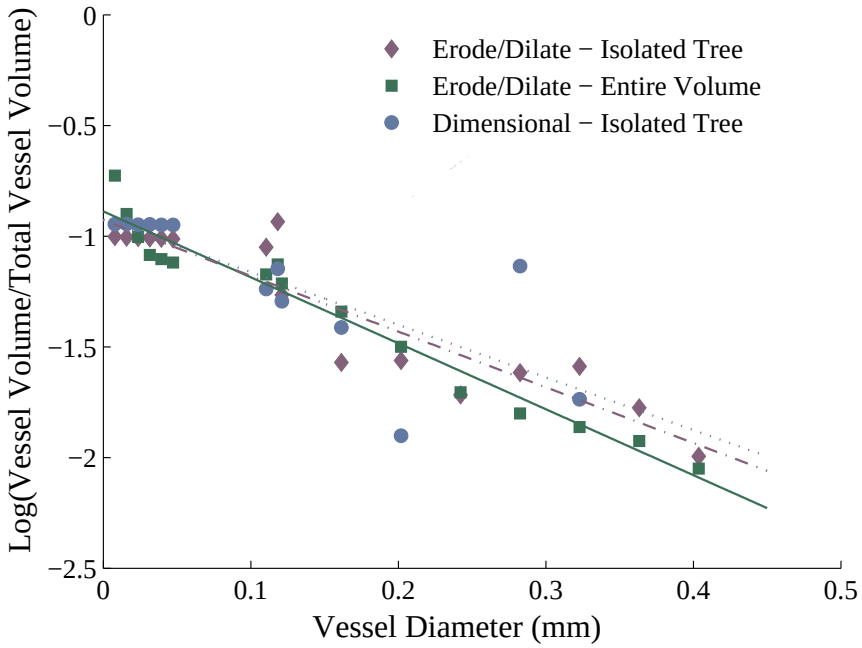

Figure 5.6: Results found for the non-embolized sample (control). The results were found for the entire tree (squares) and individual tree (diamonds) by the erode/dilate method, as well as by direct measurements of the individual tree (triangles). From [63]

Table 5.1: Least-squares fitting results for erode/dilate measurement method validation corresponding to Figure 5.6.

Specimen	Method	Slope	Intercept	R^2 Value
Isolated Tree	Erode/Dilate	-2.52	-0.93	0.87
Entire Biopsy	Erode/Dilate	-2.98	-0.89	0.96
Isolated Tree	Direct	-2.38	-0.92	0.59

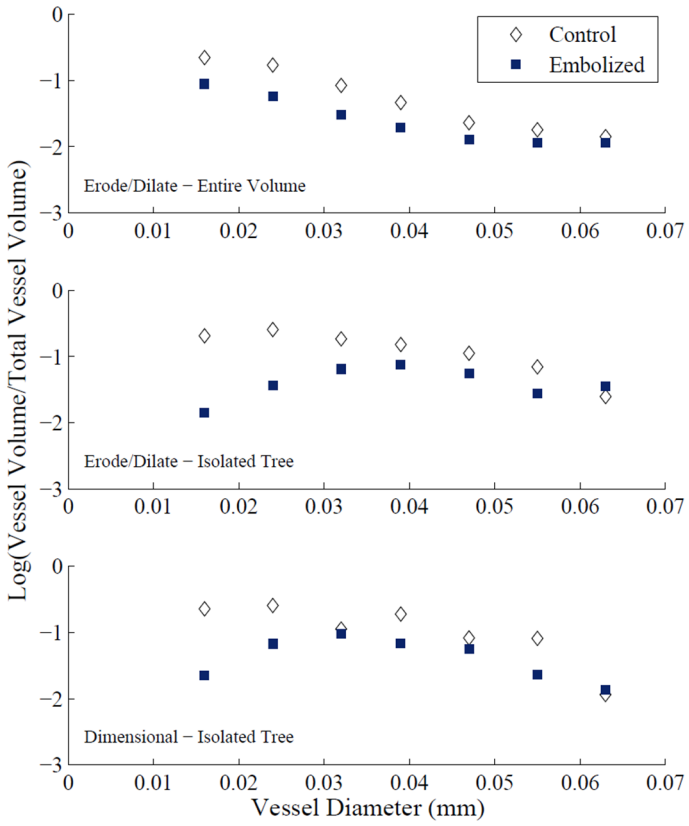

Figure 5.7: Comparison of embolized to non-embolized specimens for entire biopsy studied by erode/dilate method (top), individual tree studied by erode/dilate method (middle), and individual tree studied by direct measurements of interbranch segments (bottom). From [63].

5.4 CONCLUSIONS

The ultimate aim of this project was to test the method of erode/dilate in determining the volume distribution in a vascular bed under varied conditions of flow and/or disease. The method was tested in comparison with direct measurements and in the presence and absence of microspheres. It was observed that the erode/dilate method provided essentially the same information as those obtained by direct measurement, regarding vessel volume distribution with respect to vessel diameter, for the entire biopsy and an isolated tree within the biopsy. It was found that the microembolization volume in vessels with diameters less than the microsphere were selectively diminished. A 100μm microsphere appears to travel further downstream, affecting vessel segments 60μm and less, in diameter.

Chapter 6

Relating Function to Branching Geometry: A Micro-CT Study of the Hepatic Artery, Portal Vein, and Biliary Tree

6.1 INTRODUCTION

The liver has two surfaces, the 'diaphragmatic surface' and the 'visceral surface' [43, 33]. The diaphragmatic surface is convex and is molded to the under-surface of the diaphragm. The porta hepatis, a deep fissure on the visceral surface, is where the hepatic artery and portal vein enter, and the biliary tree exits the liver. At the porta hepatis, two layers of the lesser omentum enclose the right and left hepatic ducts (components of the biliary tree), as well as the right and left branches of the hepatic artery and portal vein. Shown in Figure 6.1 is a diagram of the relevant liver vasculature for this chapter. The flow direction of the hepatic artery, portal vein, and biliary tree are shown, along with the liver surface for orientation. The vascular structures lie in the order of portal

This chapter was modified from the original manuscript: **TL Kline, M Zamir, and EL Ritman. Relating Function to Branching Geometry: A Micro-CT Study of the Hepatic Artery, Portal Vein, and Biliary Tree.** ***Cells Tissues Organs*****, 194:431-442, 2011.** and reproduced by permission of the publisher: Karger (see **Chapter A**)

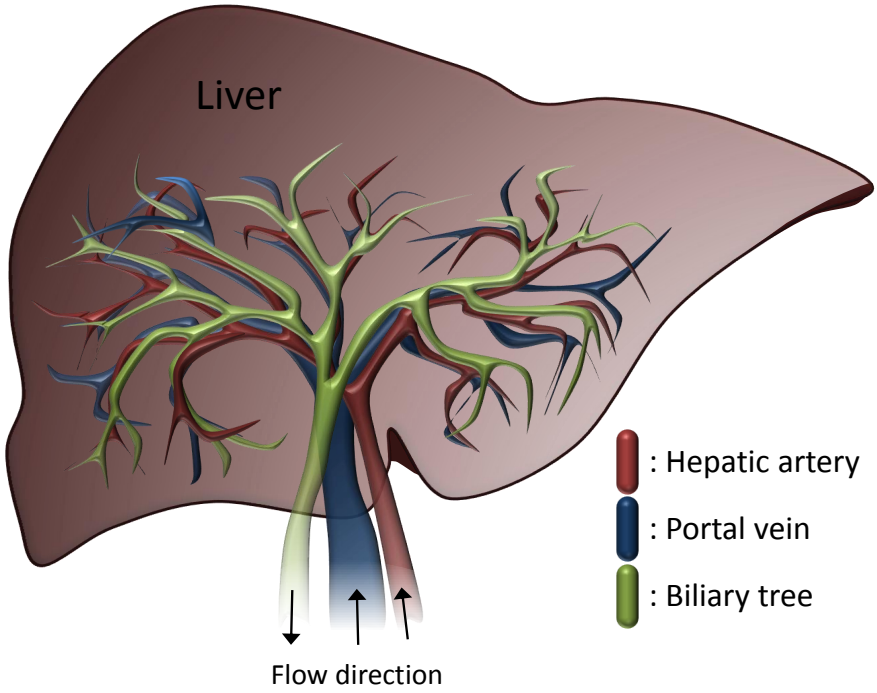

Figure 6.1: The hepatic artery, portal vein, and biliary tree all follow roughly the same anatomical paths throughout the liver, and all three enter the liver through the porta hepatis. The liver outline is also depicted for orientation.

vein, hepatic artery, and bile ducts (therefore bile ducts are more accessible during surgery due to being located the most ventral of the three [33]). The hepatic artery, portal vein, and biliary tree follow essentially the same anatomical paths within the liver, thereby known collectively as the portal triad.

To investigate the branching geometry of the vascular trees, we analyzed micro-CT images of rat livers after contrast medium was injected into the vessel trees. The hierarchical structure, interbranch segment lengths, and interbranch segment diameters were characterized. These data were then investigated by analyzing the geometric properties of the vascular structures, in particular with regard to the model derived by Murray [8] on the basis that the fluid transport system (vasculature) geometry is consistent with simultaneous minimization of both the power loss of laminar flow, and the total volume

of material needed to maintain the system (i.e., the lumenal contents). Note that these factors have opposing geometrical consequences.

6.2 METHODS

6.2.1 Specimens

Previously prepared specimens [23] were used as the dataset in this study, and are here briefly described. Male Fisher-344 rats weighing between 200 to 220g were separated into three groups. Microfil, a radiopaque liquid silicone polymer compound (MV-122; Flow Tech,. Inc,. Carver, MA), was injected into either the hepatic artery (Group 1), the biliary tree (Group 2), or the portal vein (Group 3). Therefore, a comparison of the different vessel structures necessitates the use of three different rat specimens; a hepatic artery from one, a biliary tree from another, and a portal vein from the last specimen. Two biliary tree specimens were analyzed to check for reproducibility of the results.

For the biliary tree injection, the infusion rate was between 0.01 to 0.05 ml/min and at a pressure of 7 to 10 mmHg. For the hepatic artery, the infusion rate was 2 ml/min and at a pressure of 60 to 70 mmHg. For the portal vein, the infusion rate was 8 to 10 ml/min and at a pressure of 10 to 12 mmHg. These infusion rates and pressures were chosen because they did not exceed the physiological flow and pressure in bile and blood of normal rats. Note that this particular Microfil compound has a viscosity of 25 cP, whereas blood has a viscosity of 3-4 cP. It is important to note, that the viscosity of the Microfil compound is designed specifically to produce a desired rate of filling rather than to match the viscosity of blood. The role played by viscosity in the two cases is quite different.

After the vessels were perfused with Microfil, the specimens were stored under refrigeration overnight to allow polymerization. The following day the liver was dissected into individual lobes and immersed in a 10% buffered formalin solution. In order to dehydrate the liver, each lobe was placed in progressively higher concentrations of glycerin in water solutions (from 30 to 75%) at 24 hr intervals, and then embedded in a clear

BioPlastic polymer (Aldon Corp Avon, NY).

6.2.2 Micro-CT Imaging

The micro-CT imaging methods that were used to scan the specimens are discussed in more detail elsewhere [13,]. Briefly, the liver lobe was mounted on a computer controlled rotating stage so that an x-ray projection image was generated in a cesium iodine crystalline plate, which converted the x-ray into a light-image, at each of 360 angles of view around 360^o. This light image generated by the x-ray within the crystal plate was optically projected (and magnified) onto a charge-coupled device imaging array which converted the light intensity on each of the 1024×1024 24μm on-a-side square pixels in the array to an electronic signal proportional to the light (x-ray) intensity. The scan data, once recorded, were normalized for the exposing x-ray intensity and then subjected to a modified Feldkamp cone beam reconstruction algorithm [60] to generate a 3D volume data set. The 3D image consisted of up to 1024^3 cubic voxels, each $\approx20\mu$m to a side, with gray scale proportional to the x-ray attenuation coefficient.

6.2.3 Segmentation

A binary file was computed by thresholding the gray scale 3D micro-CT images. The vascular trees were extracted from this image by means of a region-growing segmentation method to include those voxels, with gray scale values above the thresholded range, that were connected to the vessel tree's root (identified by visual inspection of the displayed 3D image). In order to include small vessel segments, a low CT-threshold (much lower than half the maximum value found in large vessel lumens) was chosen, just above the "noise" in the liver parenchyma in the CT image, in order to include vessel segments that had a reduced peak gray scale value caused by the MTF (blurring) of the micro-CT system. Specifically, the gray scale within a large vessel lumen is measured, as well as the gray scale in the surrounding tissue. The threshold is then set no higher than the average between these two values. The region-growing method resulted in a single connected tree structure for all specimens.

6.2.4 Vascular Tree Measurements

The 3D segmented data set was used as the input for the extraction of the vascular tree's centerline ("skeleton"). The extraction of the vascular tree centerline allows for the simplification of the complex tree structure from which the branch segment location within the tree, and its connection to the other branch segments, is conveyed (essentially the first step in defining the vascular tree topology). Using locations along the centerline within the segmented image, the tree's hierarchical nature, branch lengths, and branch diameters were determined. More details on the centerline extraction method, and subsequent measurements of interbranch segment lengths and diameters can be found in [63, 76, 118].

6.2.5 Characterization of Branching Geometry

To further characterize the branching geometry of the different samples, we note that the vessel tree structures can be modeled as binary trees, where at each bifurcation one parent segment divides into two branches. By convention [100], the 'level' (or generation) of the branches is one higher than that of their parent branch segment. The diameter of the branches (d_1 and d_2) are related to the parent segment's diameter (d_0) by

$$d_0^k = d_1^k + d_2^k, \tag{6.1}$$

where k is the junction exponent and under the framework of Murray's cube law $k = 3$. To characterize the parameters of vascular branching, we computed properties such as the asymmetry ratio

$$\lambda = \frac{d_2}{d_1}, \qquad d_2 \leq d_1, \tag{6.2}$$

which has a convenient range lying between 0 and 1. In non-dimensional form the two branches are related to the asymmetry ratio by

$$\frac{d_1}{d_0} = \frac{1}{(1+\lambda^k)^{1/k}}, \qquad \frac{d_2}{d_0} = \frac{\lambda}{(1+\lambda^k)^{1/k}}, \tag{6.3}$$

which show the effects of relative vessel diameter. Also, the area ratio at an arterial bifurcation can be defined as

$$\beta = \frac{d_1^2 + d_2^2}{d_0^2} = \frac{1+\lambda^2}{(1+\lambda^k)^{2/k}}, \tag{6.4}$$

which shows how the area ratio depends on the degree of asymmetry as well as the power law index k.

To measure k, the method presented by Zamir et al. [[119]] was used. Under this method, the relative error

$$e(k) = \frac{d_0^k - (d_1^k + d_2^k)}{d_0^k}. \tag{6.5}$$

is computed for each junction. The median value of the error was computed for each vascular tree for junction exponents of 1, 2, 3, and 4. A linear fit of k vs. $e(k)$ has a y-intercept equal to the 'best-fit' junction exponent.

Finally, the power requirement or cost of deviating from the optimum configuration (i.e., $k = 3$), was calculated from [4]

$$\psi = \frac{d_0^{-4}(d_1^3 + d_2^3)^{4/3} + 2d_0^2(d_1^3 + d_2^3)^{-2/3}}{3}. \tag{6.6}$$

The basis for this equation is that we assume the daughter diameters are correct and the parent vessel's deviation from the optimal configuration results in the energy cost ψ. It is derived from the total power required to support both flow and metabolism.

Effect of Variability

The question of whether the observed differences between the biliary tree and the hepatic artery and portal vein could result from either variability in an ideal Murray-type tree, or measurement error, was explored with a theoretical tree model consisting of 10 generations and following Murray's law

$$d_0^3 = d_1^3 + d_2^3. \tag{6.7}$$

Furthermore, we let the asymmetry ratio vary between generations as in

$$\lambda(j) = 0.2j - 0.1(j-1) \tag{6.8}$$

where j represents the generations. Note that this criterion was chosen in order to consider a distribution of asymmetry ratios as is commonly found in physiological systems. We then incorporate a uniformly distributed random variability, in which, the actual vessel segment diameter varies from the ideal configuration by

$$d_a = d_i + R_x d_i, \tag{6.9}$$

where d_i is the ideal Murray-tree diameter, R_x is the random variable multiplier, and d_a is the modified diameter. As an example, when the variability is set at 5%, the random variable lies within the range between -0.05 and +0.05.

6.3 RESULTS

Displayed in Figure 6.2 are the results of the average vessel segment length vs. generation, for the hepatic artery (top left), the portal vein (top right), the biliary tree specimen *bt1* (bottom left), and the biliary tree specimen *bt2* (bottom right). The standard deviation about the mean is also shown. A general trend towards a decrease in vessel segment length is apparent.

The length/diameter ratio is a critical factor in determining both the relevance of Poiseuille flow to the vascular structures, and also if local shear stress is a factor in determining branch segment diameters [120]. The average length/diameter ratio ($\pm$ standard deviation) is 4.85 $\pm$ 3.78 for the hepatic artery, 5.11 $\pm$ 4.15 for the portal vein, 28.17 $\pm$ 26.71 for bile duct *bt1*, and 25.1 $\pm$ 24.48 for bile duct *bt2*.

The non-dimensional diameter (see Equation 6.3) for the larger branch segment vs. asymmetry ratio are shown in Figure 6.3 for the hepatic artery (top left), the portal vein (top right), the biliary tree specimen *bt1* (bottom left), and the biliary tree specimen *bt2* (bottom right). The non-dimensional diameter for the smaller branch segment vs.

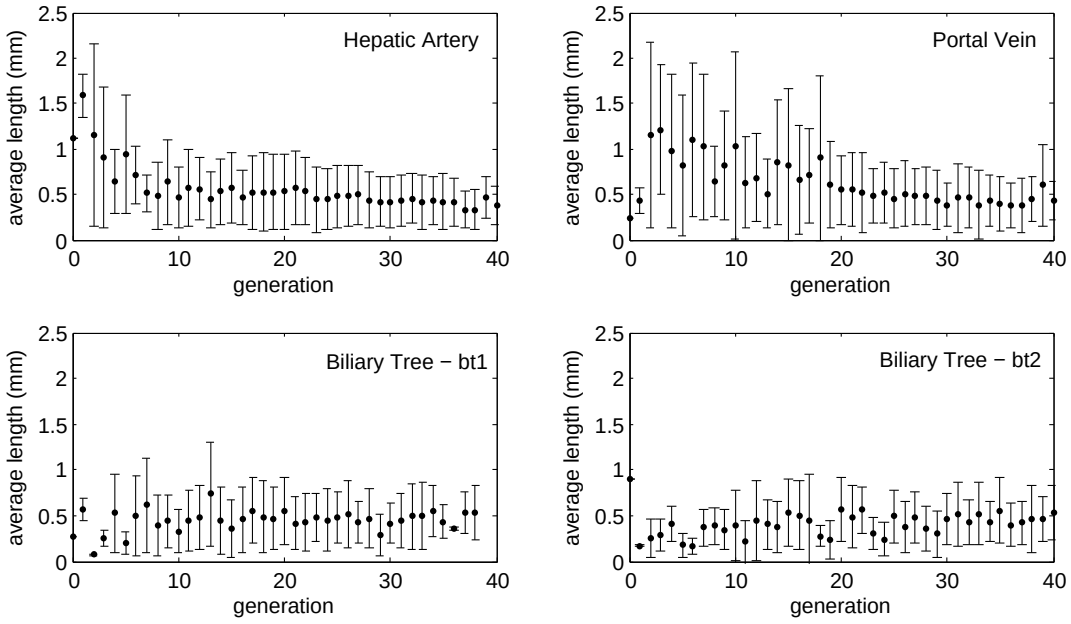

Figure 6.2: Interbranch segment lengths in the tree structure of the hepatic artery (top left), the portal vein (top right), the biliary tree specimen *bt1* (bottom left), and the biliary tree specimen *bt2* (bottom right). The error bars represent the standard deviation of the vessel lengths found within each generation.

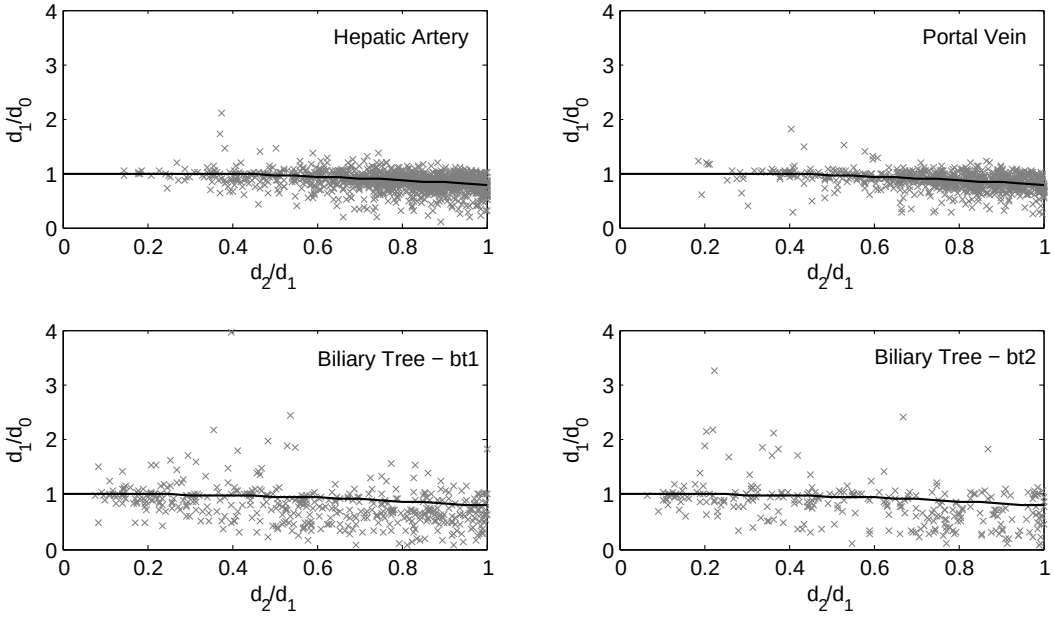

Figure 6.3: Non-dimensional diameters of the larger branch segments asymmetry ratio, in the tree structure of the hepatic artery (top left), the portal vein (top right), the biliary tree specimen *bt1* (bottom left), and the biliary tree specimen *bt2* (bottom right). The result for an ideal tree following a "cube" law (solid black line) is also presented.

asymmetry ratio are shown in Figure 6.4, and the area ratio at an arterial bifurcation vs. the asymmetry ratio for each sample is shown in Figure 6.5.

The junction exponent was found to be 2.97 for the hepatic artery, 2.94 for the portal vein, 1.65 for *bt1*, and 1.84 for *bt2*. How these values were determined is conveyed in Figure 6.6. Using the data of interbranch segment diameters and their interconnectivity, the relative error was computed by Equation 6.5 for $k = 1$, 2, 3, and 4 at each junction of the different vascular trees. The median error value for each k-value was then plotted as shown (i.e., $e(k)$). Thus, each vascular tree has four data points (corresponding to their relative errors at each k-value). A linear fit to the individual vascular tree's data has a y-intercept that corresponds to the junction exponent which best matches the vessel tree data. In terms of the relative power requirement (ψ in Equation 6.7), the hepatic artery is within 4.3%, the portal vein is within 4.0%, the biliary tree *bt1* is

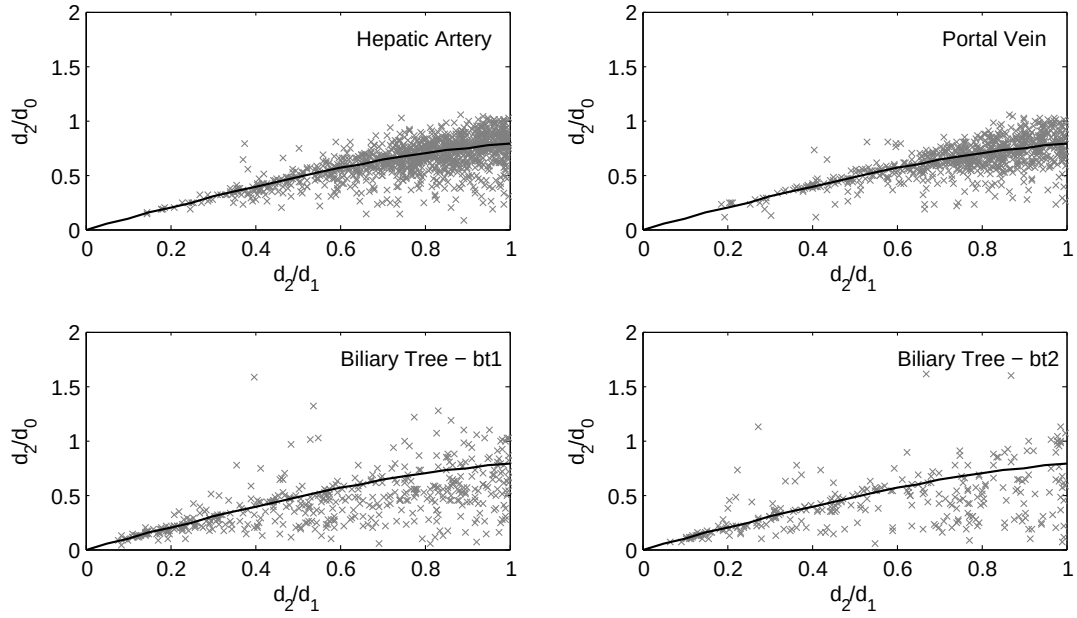

Figure 6.4: Non-dimensional diameters of the smaller branch segments asymmetry ratio, in the tree structure of the hepatic artery (top left), the portal vein (top right), the biliary tree specimen *bt1* (bottom left), and the biliary tree specimen *bt2* (bottom right). The result for an ideal tree following a "cube" law (solid black line) is also presented.

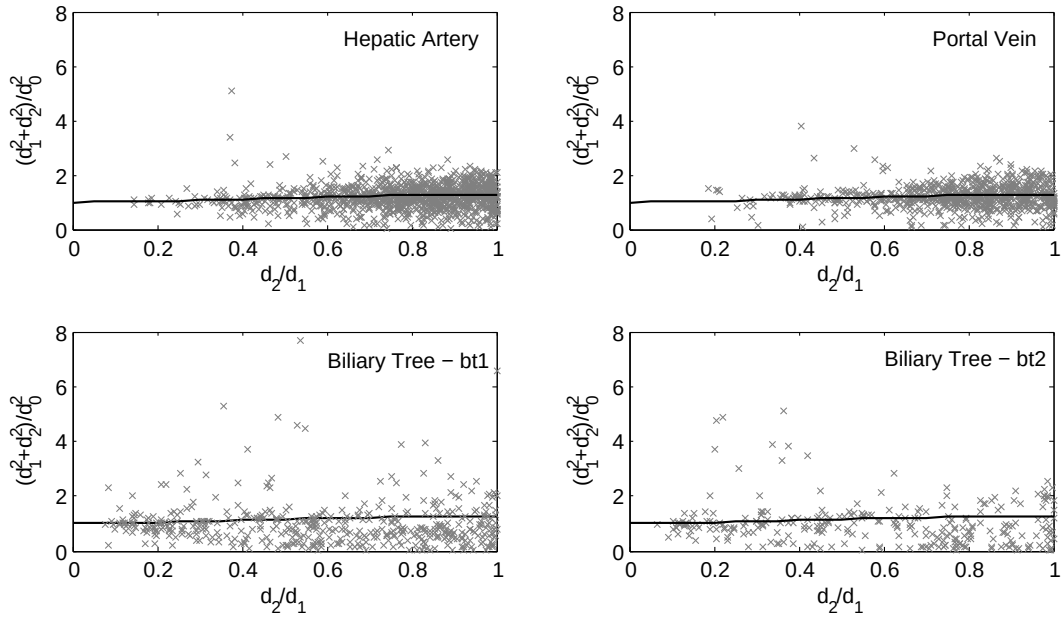

Figure 6.5: Area ratios at arterial bifurcations vs. the asymmetry ratios in the tree structures of the hepatic artery, the portal vein, and the biliary tree specimens
Area ratios at arterial bifurcations vs. the asymmetry ratios in the tree structures of the hepatic artery (top left), the portal vein (top right), the biliary tree specimen *bt1* (bottom left), and the biliary tree specimen *bt2* (bottom right). The result for an ideal tree following a "cube" law (solid black line) is also presented.

within 20.2%, and *bt2* is within 16.6% and of the optimal configuration predicted by Murray [8].

Shown in Figure 6.7 are plots of the larger diameter non-dimensional diameter for the hypothetical model vasculature (the theoretical equivalent of the experimental data presented in Figure 6.3). The variability is set at 5% (top left), 10% (top right), 20% (bottom left), and 40% (bottom right). In each plot the result for an ideal tree following a "square" law (dots) as well as a "cube" law (solid black line) are shown. The line representing the tree following a "cube" law is essentially our model's initial state, before incorporating variability.

6.4 DISCUSSION

Measuring vascular casts is historically the method used for measuring vascular branching networks [10, 93, 94]. However, such methods typically lose information pertaining to the interconnectivity of branch segments. This is due to the fact that often the casts are physically broken in order to measure the physical dimensions of interbranch segments, and statistical analysis approaches are then used to say something general about the characteristics of the vascular bed [2]. The method of optical measurement of an intact vascular cast is very time consuming, labor-intensive, and highly inefficient. In the work of Zamir [[10]], more than a year was required for measurements of the vascular tree from a right coronary artery consisting of 4,531 interbranch segments. At that time, image analysis methods were found inadequate in terms of accuracy, and the technical problem of automatically evaluating the hierarchical structure of the vascular tree had not been solved. Finally, the method of casting is of course not applicable to the tissue of a living specimen due to its destructive nature.

Using the automated analysis of micro-CT images, instead of optical measurements of a cast, saves time and allows analysis of highly complex tree structures. For example, the hepatic artery analyzed in this study is composed of more than two thousand interbranch segments, and the interbranch relationships, measurement of interbranch segment lengths and diameters were performed automatically in minutes, as opposed

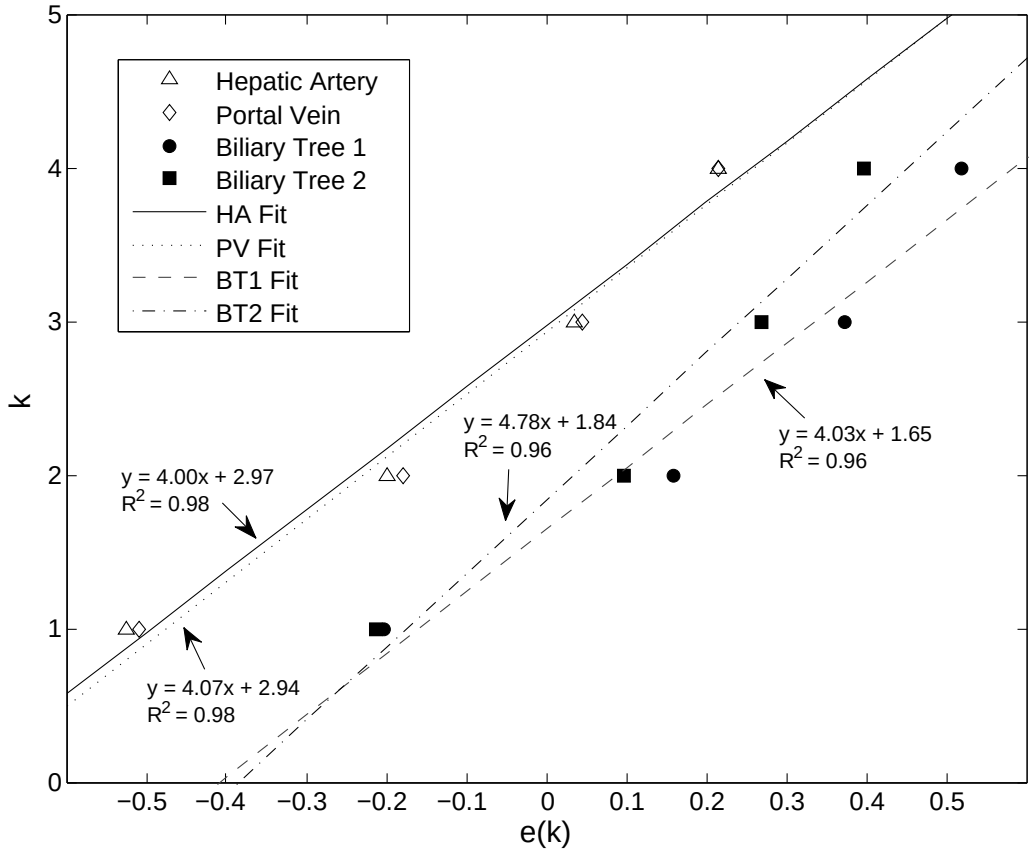

Figure 6.6: To determine the junction exponent for each specimen the relative error was computed by Equation 6.5 for k = 1, 2, 3, and 4 at each junction of the different vascular trees. The median error value for each k-value was then plotted as shown. Thus, each vascular tree has four data points (corresponding to their relative errors at each k-value). A linear fit to the individual vascular tree's data has a y-intercept that corresponds to the junction exponent which best matches the vessel tree data. As shown, the hepatic artery and portal vein are best represented as vascular structures which adhere to Murray's cube law. The two biliary trees, on the other hand, follow a square law.

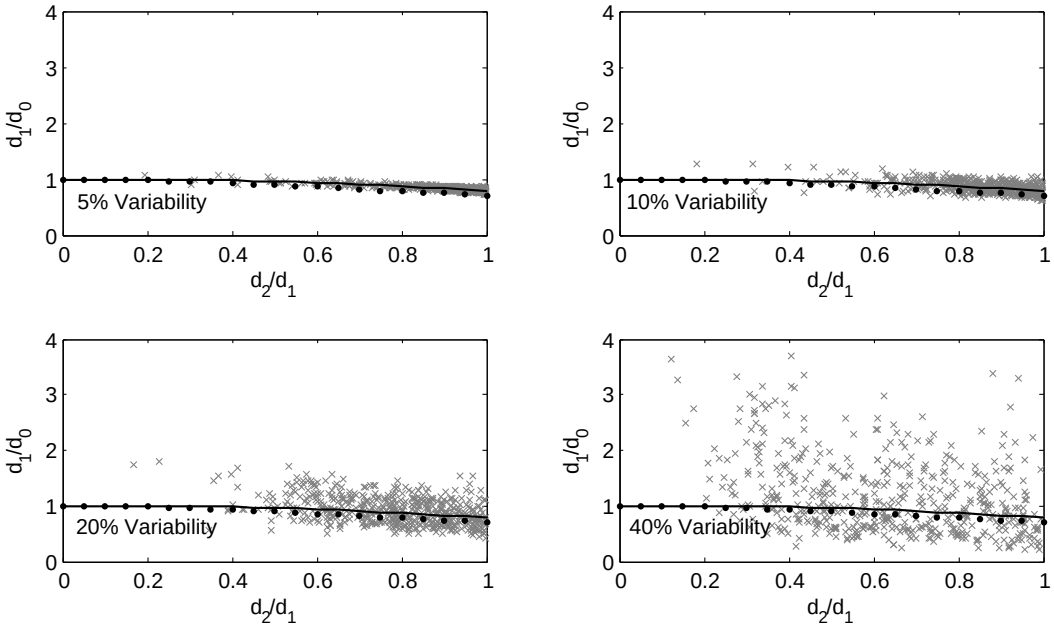

Figure 6.7: Theoretical larger branch non-dimensional diameter with imposed 5% variability (top left), 10% variability (top right), 20% variability (bottom left), and 40% variability (bottom right). Also shown are the result for an ideal tree following a "square" law (dots) and a "cube" law (solid black line).

to months. More important, using micro-CT images of *in situ*, opacified microvasculature, instead of an isolated cast, means that the measurement technique can be easily extended to *in vivo* analysis.

A methodology issue in the present study is that the different vascular trees were obtained from different rat specimens, although each vascular structure was composed of approximately the same number of generations. Ideally all three vessels should have been injected in a single liver. However, in addition to the technical difficulties involved in sample preparation, this would likely result in difficulty in differentiating small diameter branch segments in the reconstructed image due to their close proximity to each other (i.e., "overlapping" of neighboring vessel gray scales due to blurring).

The results in general show some important differences between the trees' vascular branching geometries. Most notably, the strong adherence to Murray's cube law by the hepatic artery and portal vein, and the large deviation from Murray's cube law by the biliary tree. Since the flow rate through a vascular tree must be the same at all levels of the tree, the square law, whereby the cross-sectional area available to the flow is the same at all levels of the tree, implies that the average velocity of the fluid is also the same at all levels of the tree. In the systemic arterial tree this situation is not supportable since the high velocity of blood in the aorta must be reduced by a factor of about 1,000 by the time it reached the capillaries [100]. Furthermore, since the shear stress at the endothelial layer of a vessel segment in Poiseuille flow is proportional to the flow rate over the cube of the vessel diameter, the square law also implies that the shear stress becomes increasingly higher towards the peripheral end of the tree as vessel diameters become smaller [100]. Again, this situation is not supportable in the arterial tree where the shear stress acting on endothelial tissue must be the same. Thus, our finding that the square law is supported in the biliary tree suggests that the optimality considerations of Murray's law are of little consequence in the biliary tree. Thus the characteristics of the flow in the biliary tree are likely closer to those of a low velocity bolus flow rather than Poiseuille flow.

We suspect that the main driving force within the biliary tree is simply that of bile entering at the peripheral end of the tree and pushing/displacing fluid forward, evidently at very low speed, towards the central levels and ultimately the exit end of the tree. These findings imply that the histological makeup and therefore the pathophysiology

of biliary tree vasculature is likely very different from that of vasculature within the systemic arterial tree. Recent findings have shown morphological heterogeneity of the biliary epithelium, as well as a wide range of different pathophysiological responses by different sized bile ducts [121].

The strength of this study's method for measuring the junction exponent (as opposed to a minimization type approach [25]) is that the collective behavior of the vascular tree's range of junction exponents can be determined while still including data in which one of the branch segments may be larger than the parent segment (in which case a minimization approach does not have a unique solution). The range of exponents found in the literature range from 1.0 up to 5.0 [119], but most frequently lie between 2.0 and 3.0 [9]. In addition, the energy cost (ψ from Equation 6.6 calculated for this study's vascular trees are within the cited range of 2 to 24% [4]. Intuitively it makes sense that the biliary tree would not need to adhere to Murray's law as do the other vascular structures. The low flow, low pressure environment would require little investment in materials needed to maintain the system (such as little smooth muscle to contain the pressure).

A notable shortcoming of Murray's law is that there is an unrealistic idealization for fluid flow in the vicinity of vessel junctions. Also, real vascular structures are not actually composed of cylindrical segments carrying parabolic Poiseuille flow profiles. For one, the flow is necessarily altered at branching junctions, and second, Poiseuille flow will only be re-established downstream some distance from a bifurcation, $\sim$10-80 vessel diameters downstream [120].

The much larger length/diameter ratio of the biliary tree is particularly interesting. A large length/diameter ratio, at least above a value of 10 is necessary for fully developed Poiseuille flow, yet the vascular trees which closely mirror the ideal Murray-type tree do not frequently satisfy this criterion. Since measurement of interbranch segment lengths have largely been ignored, data related to this geometric property are scarce. It appears probable that the biliary tree, unlike the hepatic artery and portal vein, favors more tortuous and lengthy pathways, which could result from the biliary tree retaining fluids when not discharging bile to the intestine (a function somewhat compensated for by the human gall bladder). This additional criterion would result in a distinct deviation from Murray's cube law. The median volume ratio (calculating $V_0/(V_1 + V_2)$ at each

bifurcation) was found to be exactly 1.0 for the bile ducts, whereas the hepatic artery and portal vein's volume ratio was 0.7. This suggests that the biliary tree more closely adheres to a local optimization criteria that requires the total vessel volume to remain constant between a parent segment and its branches (recall that the branches actually flow into the parent segment).

From the theoretical analysis of variability, we conclude that neither variability in an ideal Murray-type tree, nor noise/measurement error would explain the observed "square" law behavior of the biliary tree in our experimental data. Thus, the question is whether the hepatic artery and portal vein measurements are biased. Based on the plots of the normalized diameter (comparing Figure 6.3 to Figure 6.7), our data is consistent with a 10% variability. In our theoretical analysis, this resulted in a change in the junction exponent from 3.0 to 3.15. Thus, variability (derived from either measurement error, or variability within the vascular trees) would not cause the differences observed when comparing the hepatic artery and portal vein to the biliary trees. In addition, variability (actual deviations from Murray-tree-type behavior) could help to explain the large amounts of scatter [9, 119, 120] typically found when comparing vascular tree data to those predicted by Murray.

Lastly, it should be noted that, vasculature plays a major role in various diseases (e.g., heart disease, tumors, peripheral vascular disease, diabetes) [43, 33]. Therefore, the ability to characterize geometrical differences in vascular structures performing functionally different roles will also be useful for outlining differences within the same vascular structures, in, for example, different states of disease. Such a characterization would likely involve extending the analysis to the computation of local blood flow magnitudes, pressure distributions, and local shear stresses [70].

Chapter 7

Automated Segmentation Method for Separating Concomitant Arteries from Veins in 3D Micro-CT Images

7.1 INTRODUCTION

Tomographic images allow vasculature to be represented in three dimensions and therefore facilitate the diagnosis of various vascular conditions based on anatomy (e.g., local stenosis, tortuosity or dilation) and/or on fluid dynamic analysis of the vascular tree's impact on vascular resistance and flow distribution. These deduced parameters are quite sensitive to the accuracy of the dimensions derived from the image of the vascular tree. Moreover, due to the large amount of data generated, automated methods of vascular segmentation and characterization are needed for logistic as well as reproducibility reasons. An in-depth review of the many developed methods for the automated segmentation of vasculature was given by [122]. However, most developed methods are effective in delineating a single vascular tree from its background but not in separating concomitant vessels within the image.

Distinguishing the two concomitant vessels is complicated by blurring of the tomographic image data, resulting from the non-ideal modulation transfer function of the CT scanner's imaging system [76], as well as partial volume effects [123] due to the size of the detector pixels and of the CT image voxel size. Our proposed method utilizes a number of image parameters to facilitate separation of the concomitant vessels. These parameters utilize a priori knowledge regarding the contrast enhanced vessel gray scale values, as well as the differences in diameters of the arterial and venous systems.

The foundation of our method utilizes prior knowledge of the contrast enhanced vascular structures in order to distinguish what is, and what is not, vasculature within the volume data set. We further incorporate geometrical features, such as the generally larger diameter of the vein compared to its companion artery, in order to separate concomitant vessel systems. Use of local gray scale information, the approximate diameter of the segmented vasculature, the distance a particular vessel voxel is from the root segment, and a parameter to enhance vessels with more elliptical cross-sections (i.e., veins), all help facilitate this separation.

In this work we validate our segmentation method by comparing the vessel volume distribution of portal veins obtained by our segmentation approach with results obtained by selectively injecting contrast into only the portal vein vessel trees. Lastly, we apply our method to the vasculature of other organs to highlight the broader utility of our approach.

7.2 BACKGROUND

The ability to study concomitant vessel systems can lead to answering a number of basic physiological questions, such as: (i) in the liver, where do the lumens of hepatic arteries and portal veins meet, and (ii) in other organs, how do the arteries and veins communicate by virtue of their anatomic proximity (e.g., countercurrent exchange). We are particularly interested in studying the liver as it differs from other organs by having two vessel systems which deliver blood to it, the hepatic artery and the portal vein [33]. In addition, the single hepatic vein that drains the liver is not concomitant to the other vessels in the liver. Studies of the liver's dual blood supply generated two hypotheses: (i) the hepatic artery and portal vein's flows do not influence each other [34], or (ii)

that a reciprocal and compensatory relation exists between changes in their flow [35]. In 1965 a definite relation between the two was identified by observing that the hepatic arterial flow increased when portal vein flow was decreased [36]. More recently, a study by [38] suggested, but did not definitively demonstrate, that shunts between the hepatic artery and portal vein exist upstream to the hepatic lobule's sinusoids (capillaries). These hepatic arteriolar-portal venular shunts would offer a means of communication between the two vessel systems as evidenced by the "hepatic arterial buffer response" [37]. Therefore, to identify and detail the potential function of these shunts we need high-resolution 3D image data so as to eliminate the possibility of false 'shunts' due to image blurring. Although histology offers very high-resolution capabilities, the 2D data logistically limit our ability to identify the 3D interconnectivity of the vasculature. The investigation of the hepatic vasculature led to the development of the proposed segmentation method to delineate the hepatic artery and the portal vein from one another.

7.3 METHODS

For purposes of illustrating our method we focus on Micro-CT images of blood vessels highlighted by injection of a contrast agent containing polymer (Microfil).

7.3.1 Specimen preparation

The animal was anesthetized and the liver exposed [67]. The hepatic artery and portal vein were cannulated in order to flush these vessels with heparinized saline to prevent blood clotting. Next the vessels were infused with Microfil (a silicon polymer doped with lead) at physiological pressures. After the Microfil was allowed to set, the organ was harvested and then potted in paraffin for subsequent scanning.

7.3.2 Micro-CT Imaging

All Micro-CT scanners have three basic components: the X-ray source, the imaging array, and a method for rotating either the specimen within a stationary scanner or the scanner around the stationary specimen. Placing a sample within the system, the

specimen is then exposed to X-rays, at multiple angles of view around 360°. The X-rays that are transmitted through the specimen are collected on the imaging array, and various reconstruction methods can then be used to create a 3D volume data set derived from the X-ray attenuation properties of the organ along a line joining the x-ray focal spot to each of the detector array pixels [124].

In each of the scanner's multi-angular x-ray images, each point is represented discretely by a detector pixel in the image array. This process results in a non-linear partial volume effect depending on the detector pixel size, penumbral blurring caused by the finite size of the x-ray source focal spot, the blurring due to the x-ray to light converting crystal and due to the modulation transfer function (MTF) of the optical coupling between the fluorescent screen and the detector array. In our case the penumbral effect is minimized by placing the specimen very close to the detector array. The larger the detector pixels the greater the chances of the partial volume effect resulting from a high contrast edge (e.g., of a contrast filled vessel lumen) being partially within that pixel. The problem is that each pixel integrates the x-ray "intensity" (i.e., I) rather than the "density" (μ), where $I = I_0 e^{-\mu x}$. Here I_0 is the illuminating x-ray intensity and x is the path length of the x-ray beam through the specimen. Thus, the subsequent logarithmic transformation needed for computation of μ is corrupted. This effect becomes greater the larger the difference in μ values within the x-ray beam illuminating a pixel.

In this study we utilize image data from our in-house micro-CT scanners [13]. The impact of the blurring on the ability to define the vessel lumen surfaces is illustrated in Figure 7.1 where the blurring of vessel edges is presented. Line profiles of a number of vessel cross-sections (>500μm in diameter) were measured and averaged to give an approximation of the amount of blurring that takes place when a 20μm detector pixel is used. We generally perform the tomographic reconstruction so that the resulting cubic voxel has a side dimension equal to that of the detector pixel. The gray scale in our CT images is $1000 \times \mu$ (in 1/cm units).

7.3.3 Segmentation method

Our segmentation method utilizes a number of image-based features with the goal of distinguishing concomitant vessel systems. An initial threshold-based segmentation is first performed in order to distinguish vasculature from the background signal (i.e.,

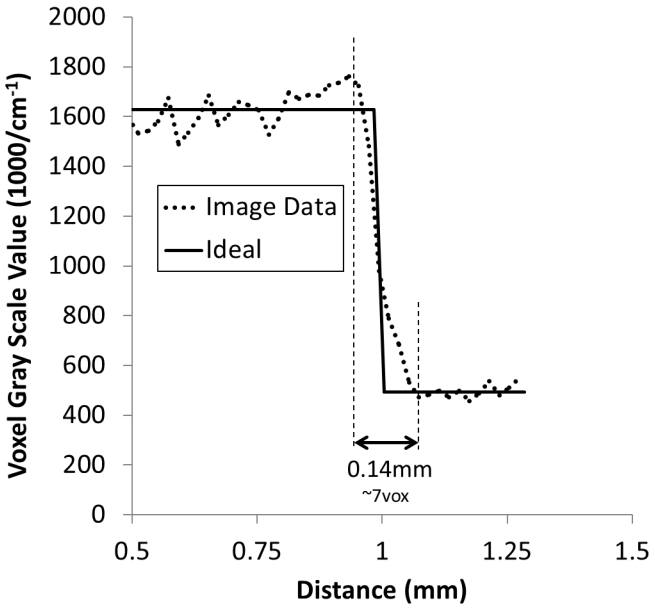

Figure 7.1: To illustrate how false connections between concomitant vessel systems are made, we considered the degree to which vessel edges are blurred in CT images made up of 20 μm on-a-side cubic voxels. Shown here is an average of 10 large vessel segments line profiles, which have been lined up with one another. When we compare these line profiles with the ideal square wave profile we can get a sense of how much of an effect blurring can have. In this case, it takes approximately 7 voxel distances for the high-contrast lumen to reach background levels at the edge of the vessel surface. Therefore, vessel systems lying in close proximity are difficult to distinguish; an effect our proposed segmentation method alleviates.

surrounding tissue). Shown in Figure 7.2 panel 'A' is a surface rendered display of the vasculature of a rat liver lobe, specimen $S1$. The hepatic artery, portal vein, and hepatic vein (which is typically not in as close proximity to the portal vein as the hepatic artery) are all present, and this volume data set will be used in this methods section to illustrate each step. The figure shows a surface rendering, showing only those voxels that are connected to the root segment through a 26-connected neighborhood. From this initial segmentation, three additional parameters are computed for each voxel as discussed in the following subsections.

Distance map

Calculation of the distance map is a common method used for image analysis processes. For example, morphological procedures such as thinning, thickening, and skeletonization use the distance map at their foundation, also pattern matching, robot collision, and path finding are among other areas the distance map has proved useful. In our case, the distance map represents the distance of a vessel-voxel, from that of its nearest non-vessel voxel. Therefore, innermost voxels (closer to a vessel cross-sections center) have higher values. Many efficient algorithms have been developed to facilitate quick calculation of the distance map and we refer the interested reader to the work of [125]. A maximum intensity projection view of the distance map computed for $S1$ is shown in Figure 7.2 panel 'B'.

Elliptical medialness measure

The external force known as gradient vector flow (GVF) has seen use in image segmentation methods, particularly related to active contours (snakes) [126, 127]. These active contours offer a means of extracting objects with variable intensities, while setting limitations on the curvature, or other parameters of the objects. We have modified this approach for our particular problem.

GVF is an edge-based static force that is defined by the vector field

$$f_{gvf}(x,y,z) = [u_{gvf}(x,y,z), v_{gvf}(x,y,z), w_{gvf}(x,y,z)]\,, \tag{7.1}$$

that minimizes the energy given by

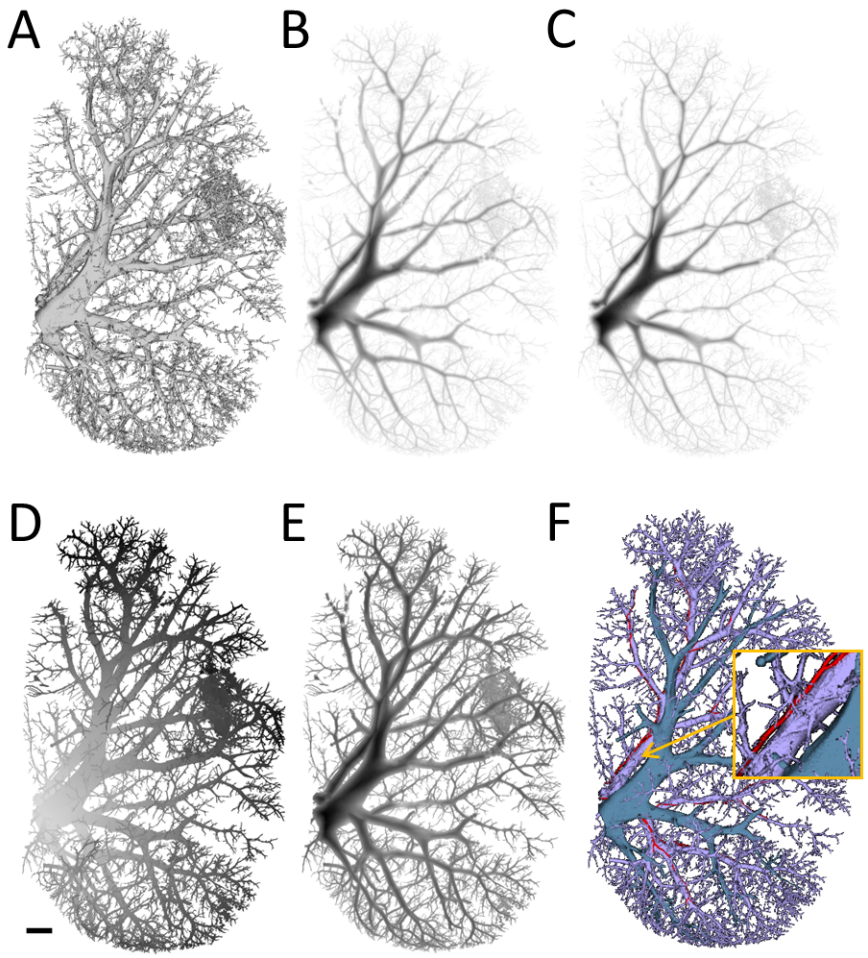

Figure 7.2: Snapshots of the various image parameters generated by our segmentation approach applied to a rat liver lobe, specimen $S1$. **Panel A**: region growing threshold segmentation, shown as a surface rendering display of all hepatic vessels which are blurred by the imaging process, the modulation transfer function of the scanner, as well as partial volume effects, all of which combine to cause difficulties in distinguishing the different vessel systems. **Panel B**: maximum intensity projection of the distance map. **Panel C**: elliptical medialness measure. **Panel D**: shortest path distance from each vessel voxel back to the hepatic vein's root segment. **Panel E**: final combined image, termed the concomitant enhanced image. This final image allows the extraction of individual vessel trees which lie in close proximity to one another. **Panel F**: segmented hepatic vein (blue), portal vein (purple), and hepatic artery (red). Insert shows image detail in region indicated by arrow. The scale bar in the bottom left corner is 1.0mm in length.

$$E_{gvf} = \int_V \left[\mu\left(\|\nabla u_{gvf}\|^2 + \|\nabla v_{gvf}\|^2 + \|w_{gvf}\|^2\right) + \|\nabla f\|^2 \|f_{gvf} - \nabla f|^2\right] dV, \qquad (7.2)$$

To compute the GVF we initialize to the image gradient and then iteratively solve for u, v, and w. The GVF is a gradient that points toward an objects edges. Since we are interested in an elliptical medialness measure, the new weighting function can be formulated from the GVF as

$$\lambda(x, y, z) = 1.0 - \left(\frac{\|f_{x,y,z}\| - min\|f\|}{\max\|f\| - \min\|f\|}\right)^q, 0 < q < 1. \qquad (7.3)$$

Within this framework, the computation of the medialness measure allows further localization of the centerline in the case of vessel structures deviating from circular (which is most often the case). Shown in Figure 7.3 is an example binary cross-section (idealized as a rectangle). For this binary cross-section ('A') both the distance map ('B') and the medialness measure ('C') were calculated. As can be seen, the medialness measure allows localization of the true center of the cross-section of anisotropic shapes. The medialness measure calculated for $S1$ is shown in Figure 7.2 panel 'C'.

Shortest path

To compute the distance each voxel was from the root location, the fast marching algorithm was utilized [103]. We initialized the algorithm with a potential function $F(x)$ that weighted vessel tree voxels equal to one another, and set all background voxels to zero. The fast marching method begins from a seed location and computes the time needed to reach each voxel. The seed was chosen as the root of the venous branch in all cases presented here. See Chapter 4 for details on the fast marching algorithm. The result of the algorithm gives each voxel a value equal to its geodesic distance from the root voxel. This component for the segmentation process aids in retaining small vessels by increasing their values (which are inherently lower in the original gray scale image due to blurring). The shortest path image computed for the hepatic vein of $S1$ is shown in Figure 7.2 panel 'D'.

Figure 7.3: Shown here is a schematic representation of a binary cross-section 'A'. This cross-section was subjected to both the distance map computation 'B', and calculation of the medialness function 'C'. The distance map will not distinguish an exact center for elliptical cross-sections as a number of voxels can have the same value along the long-axis. As illustrated, the medialness measure computed from the GVF field allows definition of an objects center for elliptical cross-sections. This is important as vessel cross-sections are most frequently elliptical in nature.

Concomitant enhanced image

The final concomitant enhanced image (Ξ) is found by the following relationship

$$\Xi = \theta\Theta + \phi\Phi + \psi\Psi + \omega\Omega \tag{7.4}$$

where Θ is the original gray scale image, Φ is the distance map generated image, Ψ is the gradient vector flow generated image, and Ω is the shortest path generated image. Also, θ, ϕ, ψ and ω are coefficients used to increase or decrease the relative importance of the different images. Empirically derived values were determined by considering the role each parameter plays. The original gray scale image allows separation of the vessels from the background. In this image small vessel segments values are greatly reduced compared to the lumen of large vessel segments. This is corrected for by the shortest path image. Separation of the different vessel trees is controlled by the distance map and medialness function as these weight the centerline of the vessel trees, thereby creating a means of eliminating concomitant vessel overlap caused by blurring.

By testing our approach on many different types of vascular structures, we determined the following to be ideal for our segmentation purposes: $\theta = 1$, ϕ =average vessel

gray scale/half the maximum distance map value, $\psi = \phi/10$, and $\omega = 1$. Therefore, the local gray scale and local distance map value are the strongest image weighting factors. The shortest path image increases the ability to retain distal small vessel segments (note: the values of Ω are related to the volume of the vascular bed), and the GVF medialness function allows weighting of elliptical vessel cross-sections. Note also that the GVF field medialness function is normalized to lie between 0 and 1 as discussed previously (whereas the distance map had values as high as 20 in the case of the rat liver lobes and is not normalized). Shown in Figure 7.2 panel 'E' is this combined image for $S1$. Viewing all these different images computed from one volume data set makes the different roles of the various image parameters evident.

After isolation of one of the vessel trees (by a simple region growing segmentation on the concomitant enhanced image), the segmented vessel can then be used as a mask to remove it from the volume data set and allow the other vascular tree to be segmented. Shown in Figure 7.4 panel 'A' is an example cross-section of $S1$. In panel 'B' the hepatic vein has already been removed, and the portal vein has been subtracted from the original image. The hepatic artery shows up as the small white vessel cross-sections. The portal vein mask image was first subjected to morphological dilation [86] in order to guarantee removal of the vessel's surface. This dilation step is performed because the calculated mask can only be as large (or less than) the original segmentation and acts as a means of approximating the vessel wall (this is shown by the black voxels, those voxels which are subtracted by the mask but not a part of the original segmentation). The final segmentation separating the hepatic artery, the portal vein, and the hepatic vein is shown in Figure 7.2 panel 'F'.

7.4 RESULTS

As a measure for the accuracy of our developed method we compared the vessel tree extracted from the image generated after both the concomitant vessels were injected with an image obtained when only one vessel tree was injected with contrast. In this case we compared the portal vein in the same rat liver lobe, of comparable size livers. Shown in Figure 7.5 is the isolated portal vein by image separation (applying our segmentation method), and contrast separation (injecting contrast and filling only the portal vein).

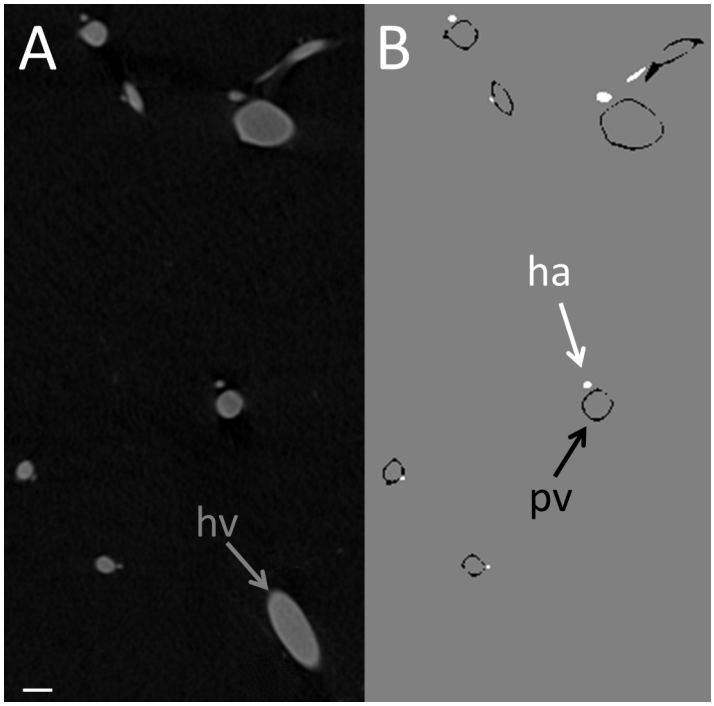

Figure 7.4: **Panel A:** cross-sectional tomographic slice of original gray scale CT image data set for $S1$. **Panel B:** the hepatic vein was removed by the segmentation method, and the portal vein mask subtracted. The scale bar in the bottom left corner is 0.3mm in length, and the hepatic artery (which follows alongside the portal vein throughout the liver) is clearly distinguished (solid white) from not only the background, but also its concomitant vessel system (the portal vein).

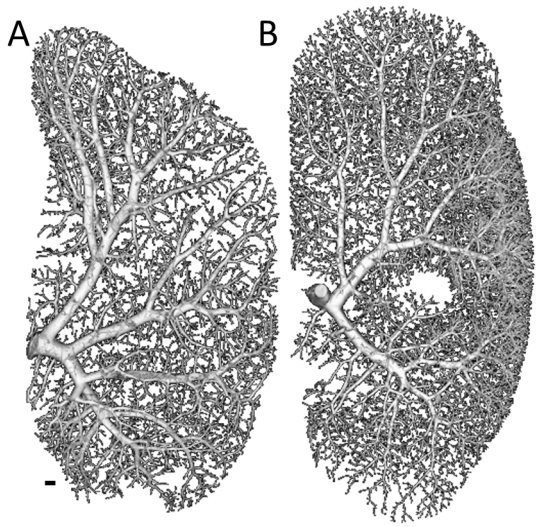

Figure 7.5: Image data sets used to compare dimensional analysis of the vascular trees. **Panel A**: isolation of portal vein from its concomitant hepatic artery by our segmentation approach ('image separated'). **Panel B**: isolation of portal vein by selective injection ('contrast separated'). The scale bar is 1mm in length.

We performed the erode/dilate method of vessel measurement [63] to determine the volume of the vessel interbranch segments at different diameters for both the isolated vessel tree obtained by our segmentation approach ('image separated'), as well as those obtained through the sample preparation method of injecting the contrast into one of the vessel systems ('contrast separated'). We applied the erode/dilate method to three portal vein trees, found in the left lateral lobe of three rat livers, for both groups. We then averaged these results for each group, and the comparison results are presented in Figure 7.6. Both vessel systems showed similar vessel volume to diameter relationships and a linear fit to the relationship is very close to the ideal 1:1.

To show the utility of the developed method, we applied it to the vasculature of the lung and kidney. Shown in Figure 7.7 are the results of applying our method to these additional data sets. Panels 'A' and 'B' were the segmentations created from two rat lung scans. The vasculature of the lung differs from that of the liver in the sense that there is a larger separation between the arterial and venous systems, and the diameter difference between the two systems is not as great (as compared to the

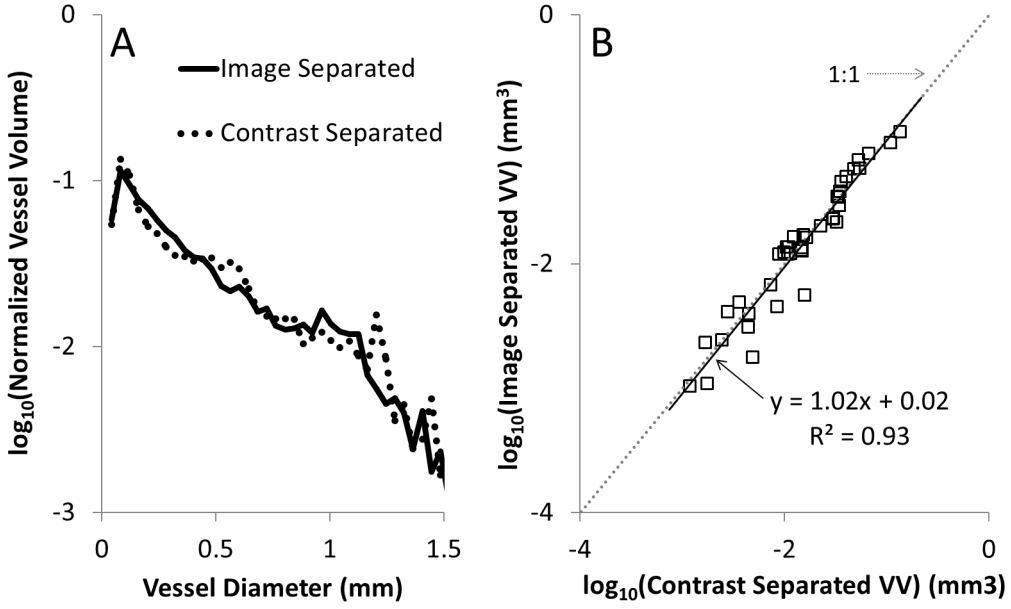

Figure 7.6: **Panel A**: plots of the total lumenal volume of all vessel segments within the selected lumen diameter range (i.e., in step sizes of 40μm). **Panel B**: compares those lumenal volume values obtained by the two specimen preparations. These results are the comparison between the 'contrast separated' data (where only one tree has contrast, thereby simplifying the subsequent image analysis problem), and the results obtained by separating the concomitant vessel tree when both vessel systems have contrast (i.e., 'image separated' by our automated segmentation method). Three vessel trees were used in each group (the portal vein in the left lateral lobe of rat livers) and averaged in order to account for normal variations between specimens.

hepatic artery and portal vein, and between the renal artery and vein). In panel 'C' and 'D' the segmentation method was applied to mouse kidney scans. As can be seen, our automated segmentation approach clearly distinguishes the two concomitant vessel systems, the renal artery and the renal vein which follow one another closely throughout the kidney.

7.5 DISCUSSION

Throughout development of our presented approach many additional methods were also tested. These included local adaptive thresholding based methods [128] which incorporate local information in order to account for contrast enhancement changes. These can result from decreased amounts of contrast in large vessels, as well as the known blurring that occurs for small vessels. Although this method helped in retaining small vessel structures, it also caused greater difficulties in overlap regions, essentially causing vessels to have much more complicated overlapping structures.

Vessel enhancement filters [129] were also considered as they use local information and scale dependent information to judge how well a particular voxel relates to that which would occur inside a contrast enhanced vessel. Again, small vessel segments could be retained, but difficulties with bifurcations and tortuous branch segments cause these methods to further complicate the issue; particularly when good contrast enhancement is already obtained.

Additionally, pre-processing methods such as filtering were investigated such as low-pass filters, and sigma-based filters. For purposes of the presentation here we chose to work with the most general case, but pre-processing filters could be optimized to further improve the method discussed in this work.

Allowing for separation of concomitant vessel systems will allow for much more detailed studies concerning vasculature. Prior works have been limited by the inability to distinguish close proximity vascular systems. In these cases simplifications are commonly made to extract meaningful data from the scans. These include looking at vascular density and spatial distributions of vasculature [130], the inability to characterize specific vessel systems (such as the hepatic artery), which were available in the scan data [67], or characterizing entire vascular beds where no knowledge of the relationship

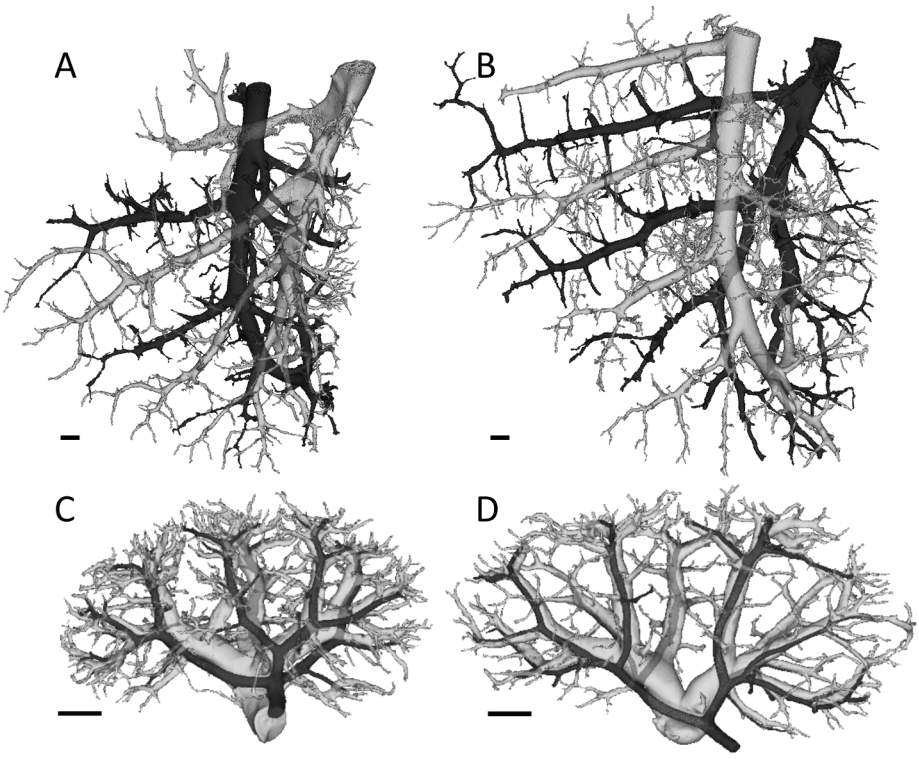

Figure 7.7: **Panels A,B:** segmentation method applied to micro-CT scans of two portions of different rat lungs. **Panels C,D:** segmentation method applied to micro-CT scans of two mouse kidneys. The automated segmentation method clearly distinguishes the two similarly sized vessel systems: the pulmonary artery (dark), and pulmonary vein (light). Also, the automated segmentation method distinguishes between the renal artery (dark), and renal vein (light), which follow each other closely throughout the kidneys. The scale bars are each 1.0mm in length. The visualizations utilize partial transparency on both vascular structures in order to follow branches that go behind one another.

and interconnectedness between the vessels is determined [131].

An area of research where automated concomitant vessel segmentation methods have been investigated, with some degree of success in automating artery-vein separation, is in magnetic resonance angiography [132]. However, the developed methods still have issues with artery-vein connectedness, and difficulties with distal regions (i.e., regions where the branches of the arteries and veins are small, and greater numbers of overlap regions typically occur).

7.6 CONCLUSIONS

The developed method discussed in the present work allows for accurate segmentation of concomitant vessel systems. This greatly helps in the analysis of vessel systems lying in close proximity to one another. We have applied the method to various vessel systems such as the hepatic artery, portal vein, and hepatic vein of the liver, the renal arteries and veins of the kidney, as well as the pulmonary artery and veins of the lung. Although our current work explored only micro-CT image data, the methods discussed should prove useful in many different areas of image analysis, across many image modalities.

Chapter 8

Anatomy of Hepatic Arteriolo-Portal Venular Shunts Evaluated by 3D Micro-CT Imaging

8.1 INTRODUCTION

The liver differs from other organs by having two vessel systems which deliver blood to it, the hepatic artery and the portal vein [33]. Early studies of the liver's dual blood supply proposed two different and contrasting hypotheses: (i) the hepatic artery and portal vein's flows do not influence each other [34], or (ii) that a reciprocal and compensatory relation exists between changes in their flow [35]. In 1965 a definite interrelationship between the two was identified by observing that the hepatic arterial flow increased when portal vein flow was decreased [36]. This mechanism was later termed the hepatic arterial buffer response [37].

More recently, a study by Richter et al. [38] offered not only further support for the hepatic arterial buffer response, but also evidence for the existence of shunts between the hepatic artery and portal vein. This was supported by noting that if portal vein flow was reduced to ∼10% its normal flow immediately downstream of the tourniquet, the

blood flow in the terminal venules had returned to nearly 70% of its normal value. Thus, these shunts would need to occur upstream to the hepatic lobule's sinusoids allowing flow from the hepatic artery into the portal vein. An implication is that these hepatic arteriolo-portal venular shunts could offer a means of communication between the two vessel systems where reduction in portal vein flow is compensated for by the hepatic artery.

Although histology offers very high-resolution capabilities, the use of serial sectioning logistically limits our ability to identify the 3D interconnectivity of the vasculature. We therefore used micro-CT to image contrast-enhanced vasculature of intact rat livers. Micro-CT offers an excellent method for studying the anatomy of the branching geometry of microvasculature by allowing high-resolution 3D images to be generated in intact specimens [54, 57, 133, 134]. These 3D images are also more conveniently susceptible to analysis of the intact, in situ, vasculature.

8.2 METHODS

8.2.1 Specimen preparation

These animal studies were approved by the Institutional Animal Care and Use Committee. Rats were anesthetized and the liver exposed by midline laparotomy. After the hepatic artery and portal vein were cannulated and flushed with heparinized saline to remove the blood and to prevent blood clotting, the rats were euthanized. Next, three different specimen preparation methods were utilized. (1) Both the hepatic artery and portal vein were infused with Microfil (a silicon polymer doped with lead) at physiological pressures (100mmHg for hepatic artery, 20mmHg for portal vein), or (2) either the hepatic artery or the portal vein alone was injected [67], or (3) the hepatic artery was injected with Microfil, and the portal vein was injected with a barium sulfate in gelatin suspension. The two contrast agents could be discriminated because the CT image gray scale of the Microfil was greater than the barium sulfate suspension. This was confirmed by scanning a phantom composed of a syringe tube filled with Microfil, and another filled with barium in order to measure the difference in gray scale between the two contrast agents. The barium contrast agent attenuates x-ray much less than the lead-based Microfil. After the contrast was allowed to set, the organ was harvested. A

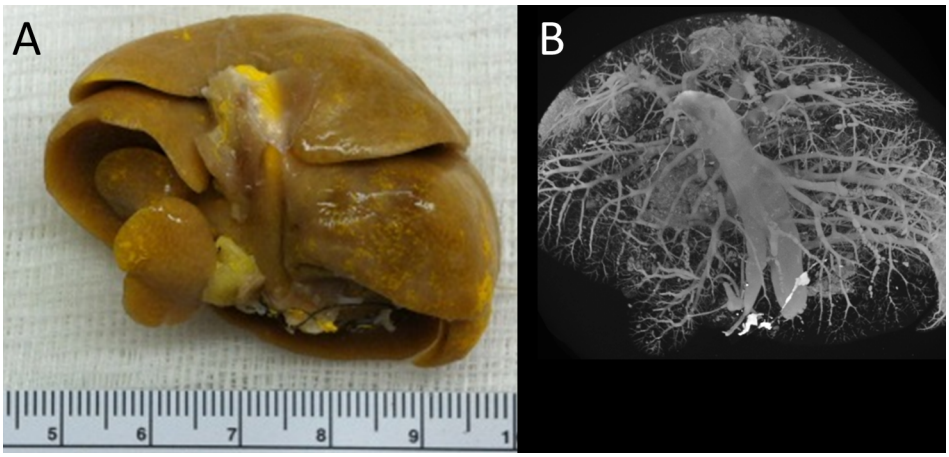

Figure 8.1: Overview of specimen preparation and subsequent micro-CT scanning. **Panel A:** A photograph of a rat liver after injection of yellow Microfil contrast polymer into the hepatic vasculature. The scale bar is in cm. **Panel B:** Rat liver scanned in its entirety (20μm cubic voxels).

photograph of an isolated liver is shown in **Panel A** of Figure 8.1 prepared by method 1. This demonstrated the uniformity of the contrast agent distribution within the liver vascular trees. Following a micro-CT scan at 20μm detector pixel resolution of the intact liver (shown in **Panel B**) of Figure 8.1, individual lobes were then isolated and individually potted in paraffin for subsequent scanning at higher 5μm detector pixel resolution. Shown in **Panel A** of Figure 8.2 is the caudate lobe from the same liver as shown in Figure 8.1. In **Panel B** a maximum intensity projection image at 20μm cubic voxel resolution is shown, and in **Panel C** a subvolume scanned at 5μm cubic voxel resolution is shown.

8.2.2 Micro-CT Imaging

In this study we utilize image data from our in-house micro-CT scanners [13]. All Micro-CT scanners have three basic components: the X-ray source, the imaging array, and a method for rotating either the specimen within a stationary scanner or the scanner around the stationary specimen [124]. Placing a sample within the system, the specimen is then exposed to X-rays, at multiple angles of view around 360°. The X-rays that are transmitted through the specimen are collected on the imaging array, and various

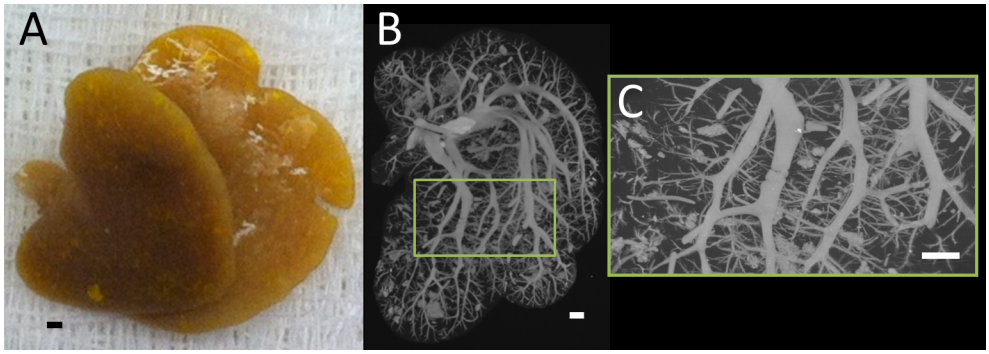

Figure 8.2: **Panel A:** A photograph of just the caudate lobe after injection of yellow Microfil contrast polymer into the hepatic vasculature. **Panel B:** Caudate lobe scanned in its entirety at 20μm cubic voxel size. **Panel C:** Subvolume of caudate lobe scanned at high-resolution (5μm cubic voxels). The scale bar in each is 1mm.

reconstruction methods can then be used to create a 3D volume data set derived from the X-ray attenuation properties of the organ along a line joining the x-ray focal spot to each of the detector array pixels. We used a modified Feldkamp cone-beam algorithm [60].

A limitation of computed tomography imaging is that there is blurring which, at the limits of resolution, can result in false connections between vessels lying in close proximity, or in apparent loss of vessels below a certain diameter. This blurring can result from the fact that the x-ray projection images are pixelized resulting in partial volume effects as well as from non-linear partial volume effects depending on the range of attenuation coefficient values along the x-ray beam illuminating a detector pixel, penumbral blurring caused by the finite size of the x-ray source focal spot, the blurring due to the thickness of the x-ray to light converting crystal and due to the modulation transfer function (MTF) of the optical coupling between that crystal (or fluorescent screen) and the electronic detector array. The 3D image itself is further blurred in proportion to the voxel size. In addition to the image-related causes, the tomographic reconstruction process also contributes to the blurring. In our case the penumbral effect is minimized by placing the specimen very close to the detector array. The larger the detector pixels the greater the chances of the partial volume effect resulting from a high contrast edge (e.g., of a contrast filled vessel lumen) being partially within that

detector pixel. The problem is that each pixel integrates the x-ray "intensity" (i.e., I) rather than the "density" (μ), where $I = I_0 e^{-\mu x}$. Here I_0 is the illuminating x-ray intensity and x is the path length of the x-ray beam through the specimen. Thus, the subsequent logarithmic transformation needed for computation of μ is corrupted. This effect becomes greater the larger the difference in μ values within the x-ray beam illuminating a single detector pixel.

The impact of image blurring on the ability to define the vessel lumen surfaces is illustrated in Figure 8.3 where the blurring of vessel edges is presented. We generally perform the tomographic reconstruction so that the resulting cubic voxel has a side dimension equal to that of the detector pixel. The gray scale in our CT images is $1000 \times \mu$ (in 1/cm units) and reconstruction size of 5μm to a side cubic voxels.

8.2.3 Blurring Simulation

In order to evaluate the impact of this image blurring on the generation of 'false' shunts between vessel lumens lying in close proximity (such as is the case between the hepatic artery and portal vein), we performed simulations utilizing the known modulation transfer function of our imaging system (at 20μm detector pixel MTF = 20 line pairs/mm and at 5μm MTF = 49/mm at 10% modulation), vessel diameters where shunts are observed. Simulations were performed for two cases, (i) the line profile obtained for a hepatic artery and portal vein lying in close proximity but without a shunt connection them, and (ii) the line profile obtained if the hepatic artery and portal vein were connected by a hepatic arteriolo-portal venular shunt. Our model assumes a square wave profile for the vessel cross-section that is blurred by a Gaussian function, as in

$$g(x) = e^{-(x^2)/(2\delta^2)}, \tag{8.1}$$

where δ is the standard deviation of the Gaussian blurring function (12μm in the case of 5μm voxel size). The Gaussian blurring function's area is set to unity.

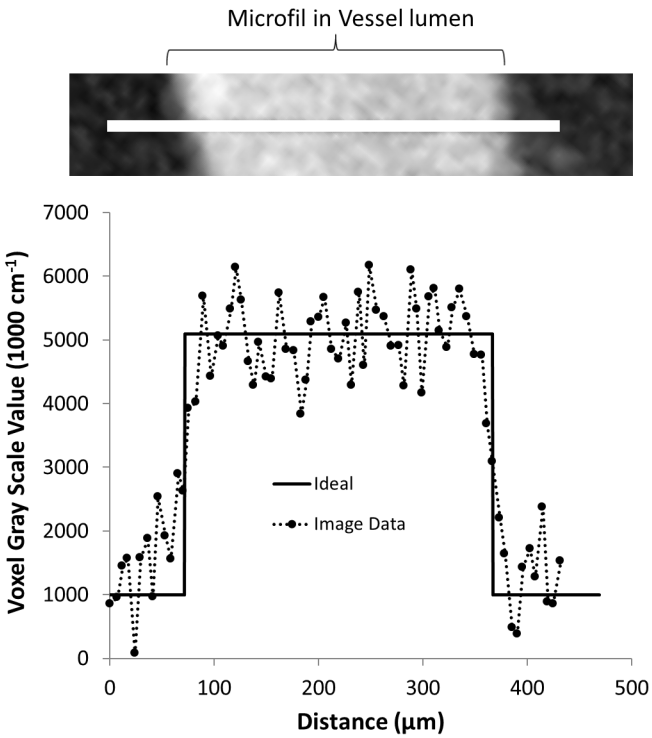

Figure 8.3: The degree to which vessel edges are blurred in CT images made up of 5 μm on-a-side cubic voxels. Shown here is a line profile of the CT image voxel gray scale values across a $\sim$0.3mm diameter vessel segment. Ideally the line profile is a square wave. The edges are not sharp, due to image blurring compounded by CT gray scale noise.

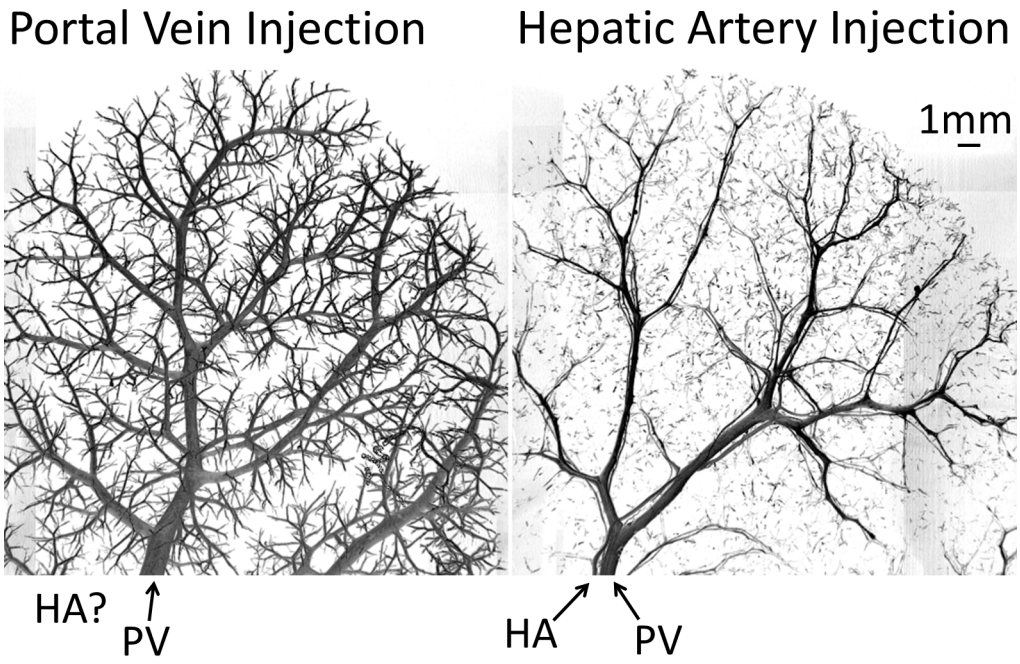

Figure 8.4: Observation of potential one-way valve-like mechanism of hepatic arteriolo-portal venular shunts. Left panel: portal vein injection results in only the portal vein contains contrast. Right panel: hepatic artery injection results in both the hepatic artery and portal vein being opacified.

8.3 RESULTS

In specimens where only the portal vein was injected, the hepatic artery did not fill with contrast. However, in the case where only the hepatic artery was injected, both the hepatic artery and portal vein were filled with the contrast medium. An example of these two cases is shown in Figure 8.4.

In addition, when Microfil was injected into the hepatic artery, and barium was injected into the portal vein, Microfil also showed up in the portal vein. This is shown in Figure 8.5.

These observations that (i) the hepatic artery does not show up when the portal vein is injected, but both vessel systems do show up when just the hepatic artery is injected, and (ii) that Microfil injected into the hepatic artery showed up in the portal vein are further evidence for a potential one-way valve-like mechanism. This concept is

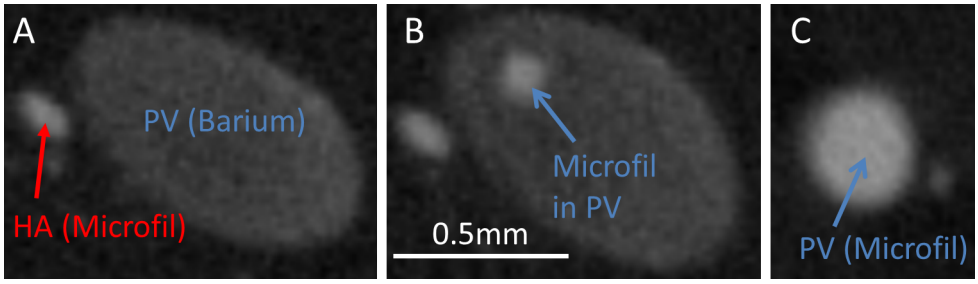

Figure 8.5: Further support of potential one-way valve-like mechanism of hepatic arteriolo-portal venular shunts. **Panel A**: hepatic artery injected with Microfil, and the portal vein injected with Barium (lower contrast). **Panel B:** evidence of Microfil contained in the portal vein. **Panel C:** portal vein cross-section completely filled with Microfil.

illustrated further in Figure 8.6.

The hepatic artery tree closely follows alongside the portal vein throughout the liver. We noted for vessels <0.5mm in diameter that the spacing between the two vessel lumens was generally ∼40μm. Shown in Figure 8.7 are four example tomographic cross-sections showing this spacing for a range of hepatic artery and portal vein diameters.

Figure 8.8 shows examples of hepatic arteriolo-portal venular shunts. These shunts were observed to frequently occur between hepatic artery and portal vein branch segments ∼50μm in diameter. In addition, Figure 8.9 relates a shunt cross-section back to the larger 3D volume from which the high-resolution image was generated.

To explore the possibility that these shunts were the result of image blurring (and therefore not real) we performed the simulations presented in the methods section. Shown in Figure 8.10 is a simulation of how a ∼65μm hepatic artery segment is blurred by the imaging process. For both the hepatic artery, and the portal vein, the blurred result (convolving the ideal square wave input with our known blurring function) match very well to the measured line profiles. Next, we simulated how the concomitant vessels blur together when they lie closer and closer to one another.

Shown in Figure 8.11 is the result of moving the simulated vessels from 40μm apart, down to their lumens being only 5μm apart. Here we also added image noise at the level found in large vessel segments (standard deviation of 400 [1000/cm]). If we then compare the blurred result to the line profile of what was taken to be a shunt, a dip in

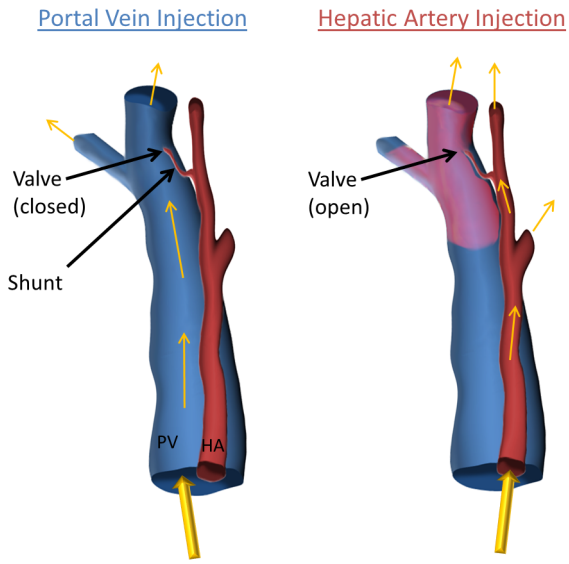

Figure 8.6: Illustration of one-way valve-like mechanism of hepatic arteriolo-portal venular shunts. In the case where contrast is only injected into the portal vein, only the portal vein is present since the shunt is closed and does not allow flow from the portal vein into the hepatic artery. In the case where contrast is only injected into the hepatic artery the valve is opened (as the portal vein is at low pressure due to no contrast being injected) and contrast fills both the hepatic artery and the portal vein. This illustration serves as an explanation for the results presented in both Figure 8.4 and Figure 8.5.

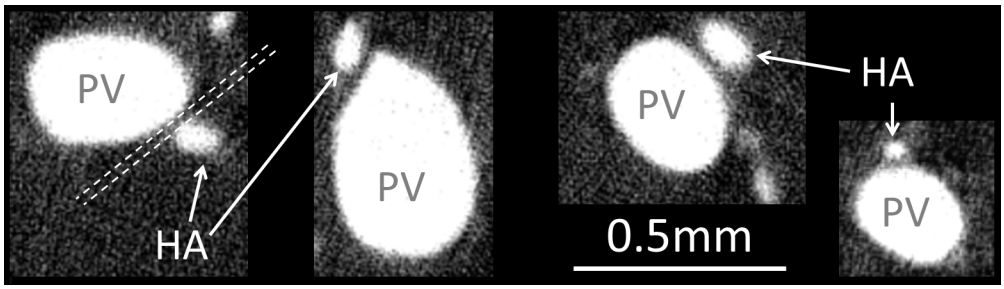

Figure 8.7: Examples of common spacing between the contrast enhanced vessel lumens of the hepatic artery and portal vein. For vessels <0.5mm in diameter, the hepatic artery and portal vein lumens stay constantly spaced at $\sim 40 \mu$m apart (represented by dashed white lines).

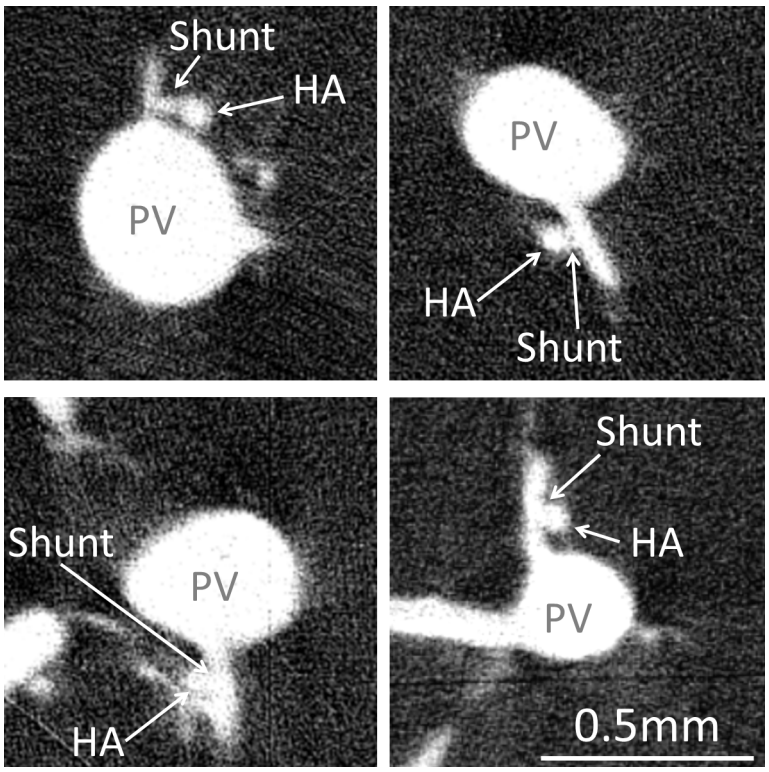

Figure 8.8: Examples of hepatic arteriolo-portal venular shunts. These most frequently occur when a small portal vein branch comes off of the main portal vein trunk nearby the concomitant hepatic artery vessel.

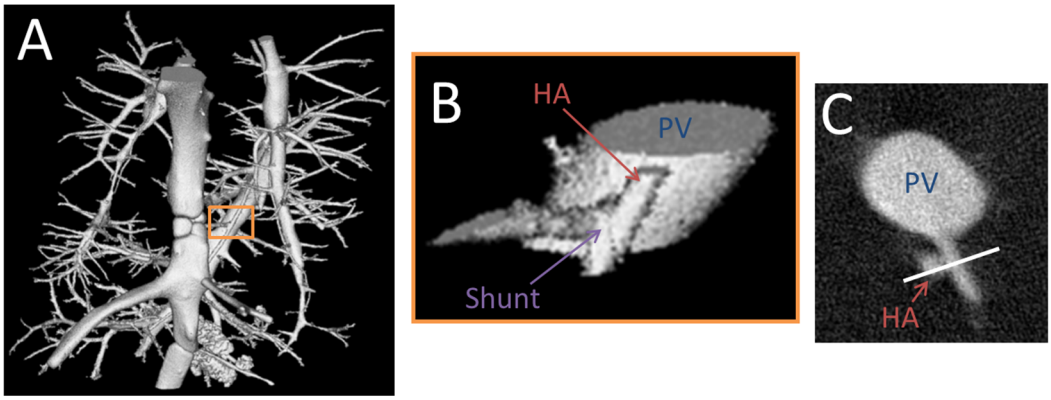

Figure 8.9: **Panel A:** 3D volume rendering of rat caudate lobe sub-volume. **Panel B:** Zoomed-in view of shunt. **Panel C:** 2D cross-section of shunt. White line is 0.3mm in length.

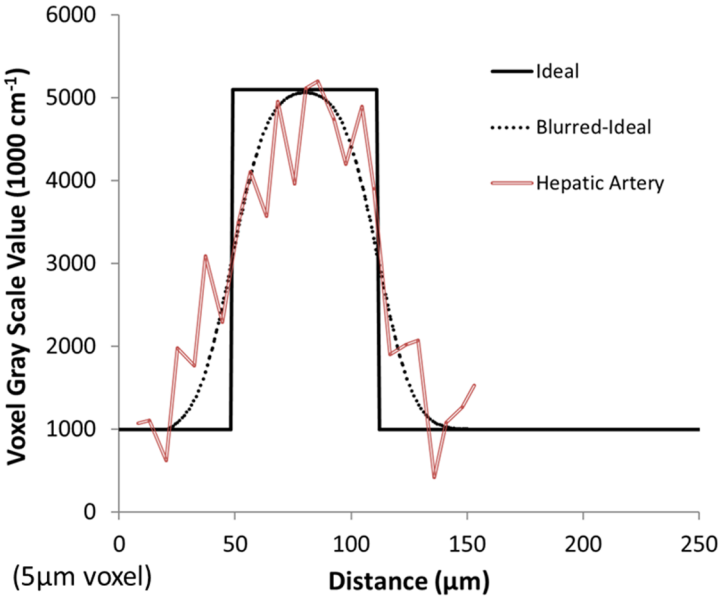

Figure 8.10: Comparison of simulated hepatic artery line profile with measured profile near shunt location. Utilizing our known blurring function closely predicts what is measured in the micro-CT image.

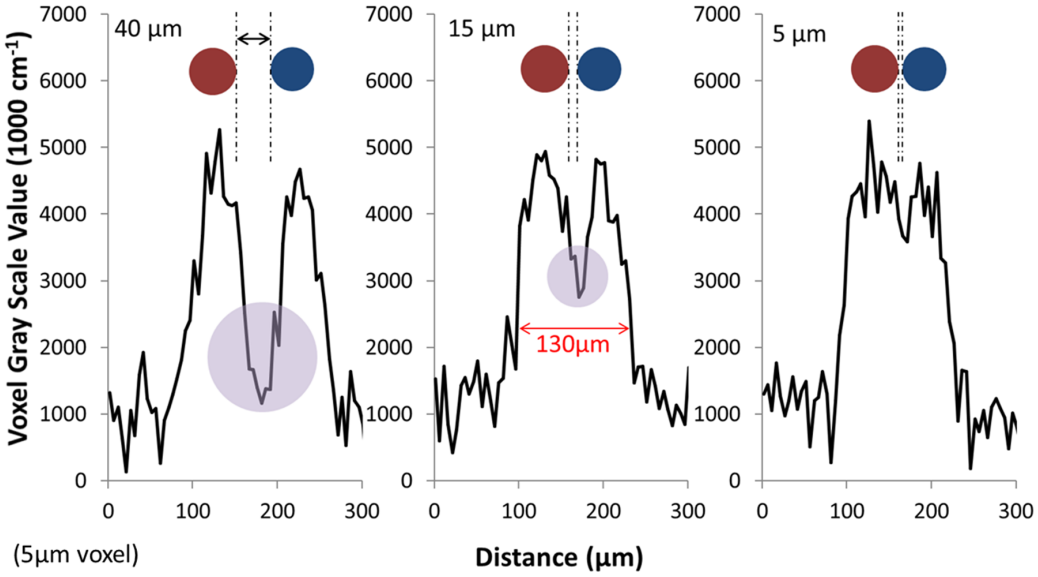

Figure 8.11: Simulation of varying spacing between hepatic artery and portal vein. The simulations show the line profiles generated between adjacent hepatic artery (65μm in diameter) and portal vein (50μm in diameter) separated by varying lumen distances of 40 (left), 15 (middle), and 5 μm (right). The 40μm result still retains much of the dip (purple circle) resulting from the spacing between the two lumens. Even at a separation of 15 μm a dip in gray scale is still evident (purple circle in middle plot). At about 5μm lumen distance (right) is when the vessels are indistinguishable. However, this separation does not represent the width of the measured shunt.

gray scale is retained up until the separation is $\sim$5μm (right panel). However, with this small of gap between the hepatic artery and portal vein, the total width of the blurred vessels does not relate to the overall width of the line profile measured at the shunt location.

Utilizing the measured diameters of the hepatic artery and portal vein, and including a 15μm shunt results in a close match to the line profile across the observed shunt, as shown in Figure 8.12.

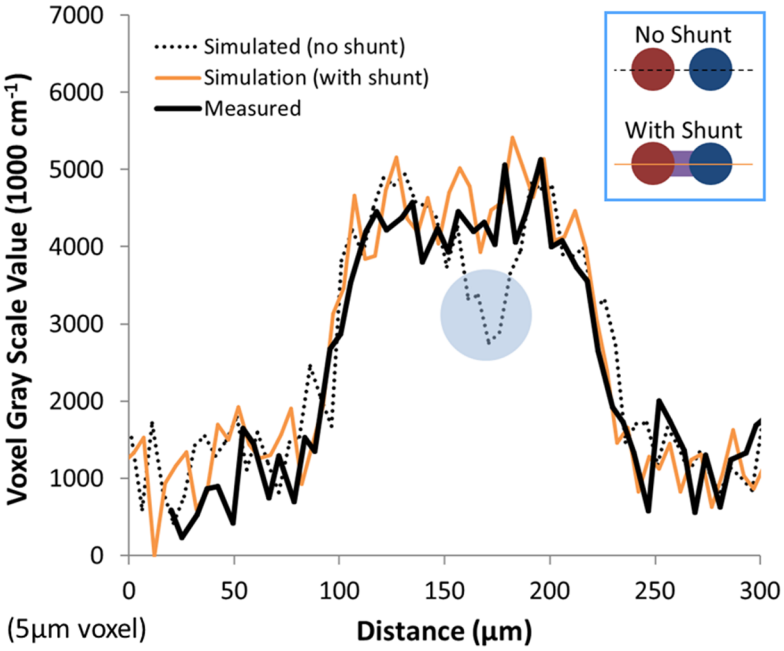

Figure 8.12: Comparing the line profile generated across a shunt, with what we would expect to see if the hepatic artery and portal vein lumens were either (i) not connected, or (ii) connected by the approximate shunt length from Figure 8.11 (15μm). Here a close fit to what we are seeing is evident when a connection exists. Thus, the observed hepatic arteriolo-portal venular shunts appear to be real connections, that could not be explained by image blurring between the hepatic artery and portal vein.

8.4 DISCUSSION

The frequently observed spacing between the lumens of the hepatic artery and portal vein ($\sim$40μm) will be useful for future studies as it sets a limit on the lower bound of image resolution required to separate the two vessel systems. This spacing led to difficulties distinguishing the two vessel systems in 20μm voxel resolution images and motivated the work presented in Chapter 7 where false connections caused by image blurring necessitated the development of an automated segmentation approach to separate the concomitant hepatic artery and portal vein.

The two observations that: (i) the hepatic artery does not show up when the portal vein is injected, but both vessel systems do show up when just the hepatic artery is injected, and (ii) that when different contrast is injected into the hepatic artery than is injected into the portal vein, the hepatic artery's contrast is observed within the portal vein are both further evidence for not only the existence of hepatic arteriolo-portal venular shunts, but also a potential one-way valve-like mechanism. The ability of the liver to compensate for reduced portal vein blood flow by increasing hepatic artery blood flow allows the organ to adapt. The extent to which this one-way shunting is dependent on the pressure differences between the hepatic artery and portal vein, or absolute pressures, is beyond the scope of these studies. If mixing occurred at the sinusoidal level, compensation would be possible, but it would seem that the pressure in the hepatic artery and portal vein would be more difficult to control in response to changes in blood flow in either vessel.

Finally, this research obtained 3D visual anatomic evidence for hepatic arteriolo-portal venular shunts. The shunts occurred between hepatic artery and portal vein branches each $\sim$50μm in diameter. Obtaining a definitive measurement of the length and diameter of the lumen and any smooth muscle component of the wall of the shunts would be of interest in order to further understand the role of these shunts, as the shunts likely undergo changes through dilation and contraction, the anatomic snap-shot (as is obtained by micro-CT) may not convey this quantitative information accurately.

8.5 CONCLUSION

By studying high-resolution 3D micro-CT images of the contrast-enhanced vasculature of rat livers, we observed that: (i) there exists a common spacing between the lumens of the hepatic artery and portal vein ($\sim$40μm), that (ii) in specimens where only the portal vein was injected, only the portal vein was contained in the image, whereas in hepatic artery injections, both the hepatic artery and portal vein were contained in the image, (iii) that the Microfil contrast injected into the hepatic artery showed up in the portal vein. Finally, we obtained 3D anatomic evidence for the existence of hepatic arteriolo-portal venular shunts as a plausible explanation for connections between the hepatic artery and portal vein proximal to the sinusoids of the liver. Thus, mixing of the hepatic artery and portal vein blood may occur upstream to the sinusoidal level, and hepatic arteriolo-portal venular shunts may function as a one-way valve like mechanism, allowing flow only from the hepatic artery to the portal vein.

Chapter 9

Conclusion

An important tool for providing information pertaining to a vascular tree's contribution to various diseases and organ malfunctions is the image analysis of microvasculature. In contrast to the imaging of organ tissues, which typically focuses on topology and variable intensity within that organ, the imaging of vasculature requires a focus on the interconnected vascular branching architecture. The goal of this work was to highlight some key difficulties in this area of analysis such as: imaging resolution, segmentation, centerline extraction, as well as the measurement strategy of individual branch segment's lengths and diameters. In terms of the accuracy of micro-CT measurements, the comparative results presented are positive and suggest that a method of characterizing microvasculature tree structures can be accomplished by micro-CT, which is beneficial since the time scale of such an analysis is far faster and less prone to reproducibility errors than a tedious manual method, such as the optical measurement of individual branch segments (i.e., the gold-standard used in **Chapter 4**).

This project also tested the method of erode/dilate in determining the volume distribution in a vascular bed under varied conditions of flow and/or disease (**Chapter 5**). The method was tested in comparison with direct measurements. It was observed that the erode/dilate method provided essentially the same information as those obtained by direct measurement, regarding vessel volume distribution with respect to vessel diameter, for the entire biopsy and an isolated tree within the biopsy. As expected, it was found that the microembolization volume in vessels with diameters smaller than the microsphere were selectively diminished. A 100μm microsphere appears to travel

further downstream than the arterial lumen diameter due to the flexibility of the vessel wall, affecting vessel segments 60μm and less, in diameter.

The automated segmentation method that was developed in this dissertation allows for accurate segmentation of concomitant vessel systems (**Chapter 7**). This greatly helps in the analysis of vessel systems lying in close proximity to one another. This dissertation applied the method to the hepatic artery, portal vein, and hepatic vein of rat livers, but also to the renal arteries and veins of mouse kidneys, as well as the pulmonary artery and veins of rat lungs.

Finally, by studying high-resolution 3D micro-CT images of the contrast-enhanced vasculature of rat livers, insights into the vascular geometry of the liver were obtained. In particular, evidence for hepatic arteriolo-portal venular shunts (**Chapter 8**). In the case that only the portal vein was injected, only the portal vein was apparent in the micro-CT image, whereas in hepatic artery injections, both the hepatic artery and portal vein were apparent in the image. Also, when a different contrast was injected into the hepatic artery (than was injected into the portal vein), the hepatic artery's contrast showed up in the portal vein. Finally, 3D anatomic evidence for the existence of hepatic arteriolo-portal venular shunts was presented. The possibility that the shunts were nothing more than blurring between the hepatic artery and portal vein was ruled out. Thus, mixing of the hepatic artery and portal vein may occur proximal to the sinusoidal level, and hepatic arteriolo-portal venular shunts may function as a one-way valve like mechanism, allowing flow only from the hepatic artery to the portal vein.

This dissertation utilized micro-CT to answer a physiological question. As different hurdles were presented, the project went down different paths to address each particular challenge. In light of all of this, still the largest drawback is that the micro-CT imaging techniques utilized are snapshots in time. Sample preparation, scanning, and analysis all attempt to draw a conclusion about the dynamic biological system in one particular state, at one moment in time. Although *in vivo* micro-CT imaging is still very much in its infancy, being able to study live specimens, at high-resolution, will allow future studies to paint a more complete picture.

In vivo studies of rat tibiae have been performed [135], as well as *in vivo* micro-CT imaging lung studies [59, 136, 137] and of rodent cerebral vasculature has been performed [15]. These previously developed methods have already had to work on

overcoming problems related to motion artifacts, which will be useful for future *in vivo* longitudinal microcirculation studies. As an example longitudinal study, the remodeling of microvasculature, as the dynamic process which it is, could be evaluated. Related to this dissertation, high-resolution perfusion imaging could be utilized to study hepatic arteriolo-portal venular shunts by restricting portal vein flow and injecting contrast into the hepatic artery. This would allow 3D visualization of how the vasculature of the liver responds and alters its blood flow in the face of altered physiological states.

In addition, methods for cardiac gating [59] could help answer the question of how well a micro-CT scan of a vascular tree (which is a snap shot in time), represents the 'true' dynamic tree geometry. For example, just how important is the diameter change caused by the contracting heart's pressure pulses? Many questions, like this one, can only be answered by doing *in vivo* scans at many time points within a single cardiac cycle.

Since physiological motion in a mouse (for instance) is 10x faster than in humans, special care is needed to reduce motion blur. For example, short exposure times with high x-ray fluency rates are needed, yet lethal dose (or LD50) radiation levels must be avoided [138] in longitudinal studies. Promising results were shown recently where perfusion measurements by micro-CT imaging were performed on an experimental phantom [139]. Clearly, *in vivo* micro-CT imaging is still developing, thus a great deal of room is available for future research investigations. One day, when fast, high spatial resolution, micro-CT scanners become available, direct analysis of dynamic vascular function will be possible.

References

[1] Kenneth D. Keele. Movement of the heart and blood in animals: An anatomical essay: by william harvey. translated from the original latin by kenneth j. franklin, and now published for the royal college of physicians of london. oxford: Blackwell scientific publications, 1957. pp. xii +209. portrait. 175. 6d. *Medical History*, 1:371–372, 9 1957.

[2] J. A. E. Spaan. *Coronary Blood Flow*. AA Dordrecht, The Netherlands: Kluwer Academic Publishers, 1991.

[3] A. Krogh. The number and distribution of capillaries in muscles with calculations of the oxygen pressure head necessary for supplying the tissue. *Journal of Physiology*, 52:409–415, 1919.

[4] T. F. Sherman, A. S. Popel, A. Koller, and P. C. Johnson. The cost of departure from optimal radii in microvascular networks. *J. Theor. Biol.*, 136(3):245–265, 1989.

[5] J. B. Bassingthwaighte, T. Ypintsoi, and R. B. Harvey. Microvasculature of the dog left ventricular myocardium. *Microvascular Research*, 7:229–249, 1974.

[6] N. M. Malyar, M. Gossl, P. E. Beighley, and E. L. Ritman. Relationship between arterial diameter and perfused tissue volume in myocardial microcirculation: a micro-CT-based analysis. *Am. J. Physiol. Heart Circ. Physiol.*, 286:H2386–H2392, 2004.

[7] M. S. Morrison, S. A. Ricketts, J. Barnett, A. Cuthbertson, J. Tessier, and S. R. Wedge. Use of a novel arg-gly-asp radioligand, 18f-ah111585, to determine changes in tumor vascularity after antitumor therapy. *J. Nucl. Med.*, 50(1):116–122, 2009.

[8] C. D. Murray. The physiological principle of minimum work i. the vascular system and the cost of blood volume. *Proc. Nat. Acad. Sci.*, 12(3):207–214, 1926.

[9] G. S. Kassab. Scaling laws of vascular trees: of form and function. *Am. J. Physiol. Heart Circ. Physiol.*, 290:H894–H903, 2006.

[10] M. Zamir. Tree structure and branching characteristics of the right coronary artery in a right-dominant human heart. *Can. J. Cardiol.*, 12(6):593–599, 1996.

[11] M. Zamir and H. Chee. Segment analysis of human coronary arteries. *Blood Vessels*, 24(1-2):76–84, 1987.

[12] R. F. Potter and A. C. Groom. Capillary diameter and geometry in cardiac and skeletal muscle studied by means of corrosion casts. *Microvascular Research*, 25:68–84, 1983.

[13] S. M. Jorgensen, O. Demirkaya, and E. L. Ritman. Three-dimensional imaging of vasculature and parenchyma in intact rodent organs with x-ray micro-CT. *Am. J. Physiol. Heart Circ. Physiol*, 275(3):H1103–H1114, 1998.

[14] M. J. Paulus, S. S. Gleason, S. J. Kennel, P. R. Hunsicker, and D. K. Johnson. High resolution x-ray computed tomography: an emerging tool for small animal cancer research. *Neoplasia*, 2(1-2):62–70, 2000.

[15] Y. Seo, T. Hashimoto, Y. Nuki, and B. H. Hasegawa. In vivo micro-CT imaging of rodent cerebral vasculature. *Phys. Med. Biol.*, 53(7):N99–N107, 2008.

[16] M. Kachelriess. Micro-CT. In W. Semmler and M. Schwaiger, editors, *Molecular Imaging I*, pages 23–52. Springer-Verlag Berlin Heidelberg, 2008.

[17] C. T. Badea, M. Drangova, D. W. Holdsworth, and G. A. Johnson. In vivo small-animal imaging using micro-CT and digital subtraction angiography. *Phys. Med. Biol.*, 53(19):R319–R350, 2008.

[18] L. Zagorchev, O. Pierre, Z. Zhen, M. Karen, M. K. Mary, S. Michael, and C. Thierry. Micro computed tomography for vascular exploration. *J. Angiogenesis Res.*, 2(7):1–11, 2010.

[19] M. Rodriquez-Porcel, A. Lerman, E. L. Ritman, S. H. Wilson, P. J. M. Best, and L. O. Lerman. Altered myocardial microvascular 3d architecture in experimental hypercholesterolemia. *Circulation*, 102:2028–2030, 2000.

[20] M. Gossl, N. M. Malyar, M. Rosol, P. E. Beighley, and E. L. Ritman. Impact of coronary vasa vasorum functional structure on coronary vessel wall perfusion distribution. *Am. J. Physiol. Heart Circ. Physiol*, 285:H2019–H2026, 2003.

[21] X. Y. Zhu, M. D. Bentely, A. R. Chade, E. L. Ritman, A. Lerman, and L. O. Lerman. Early changes in coronary artery wall structure detected by microcomputed tomography in experimental hypercholesterolemia. *Am. J. Physiol. Heart Circ. Physiol.*, 293:H1997–H2003, 2007.

[22] H. Le, J. T. Wong, and S. Molloi. Estimation of regional myocardial mass at risk based on distal arterial lumen volume and length using 3D micro-CT images. *Comp. Med. Im. Graph.*, 32(6):488–501, 2008.

[23] T. V. Masyuk, E. L. Ritman, and N. F. LaRusso. Hepatic artery and portal vein remodeling in rat liver vascular response to selective cholangiocyte proliferation. *Am. J. Pathol.*, 162(4):1175–1182, 2003.

[24] D. A. Nordsletten, S. Blackett, M. D. Bentley, E. L. Ritman, and N. P. Smith. Structural morphology of renal vasculature. *Am. J. Physiol. Heart Circ. Physiol.*, 291:H296–H309, 2006.

[25] J. Op Den Buijs, Z. Bajzer, and E. L. Ritman. Branching morphology of the rat hepatic portal vein tree: a micro-CT study. *Ann. Biomed. Eng.*, 34(9):1420–1428, 2006.

[26] A. Garcia-Sanz, A. Rodriquez-Barbero, M. D. Bentley, E. L. Ritman, and J. C. Romero. Three-dimensional microcomputed tomography of renal vasculature in rats. *Hypertension*, 31:440–444, 1998.

[27] G. S. Kassab and Y. C. B. Fung. Topology and dimensions of pig coronary capillary network. *American Journal of Physiology: Heart Circulatory Physiology*, 267:H319–H325, 1994.

[28] B. J. McGuire and T. W. Secomb. A theoretical model of oxygen transport in skeletal muscle under conditions of high oxygen demand. *J. Appl. Physiol.*, 91(5):2255–2265, 2001.

[29] D. Goldman. Theoretical models of microvascular oxygen transport to tissue. *Microcirculation*, 15:795–811, 2008.

[30] J. R. Henderson and P. M Daniel. Portal circulations and their relation to countercurrent systems. *Experimental Physiology*, 63:355–369, 1978.

[31] D. G. Welsh and S. S. Segal. Endothelial and smooth muscle cell conduction in arterioles controlling blood flow. *American Journal of Physiology: Heart Circulation Physiology*, 274(43):H178–H186, 1998.

[32] S. P. Sutera and R. Skalak. The history of poiseuille's law. *Annual Review of Fluid Mechanics*, 25:1–19, 1993.

[33] C. S. Sinnatamby. Last's anatomy: Regional and applied. page 584pp. Elsevier Health Sciences, 2006.

[34] J. L. Bollman, M. Khattab, R. Thors, and J. H. Grindlay. Experimentally produced alterations of hepatic blood flow. *Arch. Surg.*, 66:562–570, 1953.

[35] S. Soskin, H. E. Essex, J. F. Herrick, and F. C. Mann. The mechanism of regulation of the blood sugar by the liver. *Am. J. Physiol.*, 124:558–567, 1938.

[36] J. L. Ternberg and H. R. Butcher. Blood-flow relation between hepatic artery and portal vein. *Science*, 150(3699):1030–1031, 1965.

[37] W. W. Lautt. Relationship between hepatic blood flow and overall metabolism: the hepatic arterial buffer response. *Fed. Proc.*, 42:1662–1666, 1983.

[38] S. Richter, B. Vollmar, I. Mucke, S. Post, and M. D. Menger. Hepatic arteriolo-portal venular shunting quarantees maintenance of nutritional microvascular supply in hepatic arterial buffer response of rat livers. *J. Physiol*, 531.1:193–201, 2001.

[39] X. Li, I. S. Benjamin, R. Naftalin, and B. Alexander. Location and function of intrahepatic shunts in anaesthetised rats. *Gut*, 52:1339–1346, 2003.

[40] I. Kassissia, A. Brault, and P. M. Huet. Hepatic artery and portal vein vascularization of normal and cirrhotic rat liver. *Hepatol.*, 19(5):1189–1197, 1994.

[41] O. Matsui, I. Kawamura, and T. Takashima. Occurrence of an intrahepatic porto-arterial shunt after hepatic artery embolization with gelfoam powder in rats and rabbits. *Acta Radiol. Diagn.*, 27(1):119–122, 1986.

[42] B. Alexander, H. Cottam, and R. Naftalin. Hepatic arterial perfusion regulates portal venous flow between hepatic sinusoids and intrahepatic shunts in the normal rat liver in vitro. *Eur. J. Physiol.*, 443:257–264, 2001.

[43] S. Standring and H. Gray. *Gray's anatomy: the anatomical basis of clinical practice*. Elsevier Health Sciences, 2008.

[44] J. H. Birnie and J. Grayson. Observations on temperature distribution and liver blood flow in the rat. *J. Physiol.*, 116:189–201, 1952.

[45] T. L. Kline, M. Zamir, and E. L. Ritman. Relating function to branching geometry: A micro-CT study of the hepatic artery, portal vein, and biliary tree. *Cells Tissues Organs*, in Press, 2011.

[46] R. Savai, A. C. Langheinrich, R. T. Schermuly, S. S. Pullamsetti, R. Dumitrascu, H. Traupe, W. S. Rau, W. Seeger, F. Grimminger, and G. A. Banat. Evaluation of angiogenesis using micro-computed tomography in a xenograft mouse model of lung cancer. *Neoplasia*, 11(1):48–56, 2009.

[47] L. Zagorchev and M. J. Mulligan-Kehoe. Molecular imaging of vessels in mouse models of disease. *Eur. J. Radiol.*, 70(2):305–311, 2009.

[48] M. Stauber and R. Muller. Micro-computed tomography: A method for the non-destructive evaluation of the three-dimensional sructure of biological specimens. In J. J. Westendorf, editor, *Osteoporosis: Methods and Protocols*, volume 455 of *Methods in Molecular Biology*, pages 273–292. Humana Press, 2008.

[49] J. Radon. On the determination of functions from their integral values along certain manifolds. *IEEE Trans. Med. Im.*, MI-5(4):170–175, 1986.

[50] A. M. Cormack. Representation of a function by its line integrals, with some radiological application. *J. App. Phys.*, 34(9):2722–2727, 1963.

[51] G. N. Hounsfield. A method of and apparatus for examination of a body by radiation such as x-ray or gamma radiation. *Patent Specification*, 1972.

[52] G. N. Hounsfield. Computerized transverse axial scanning (tomography). 1. description of system. *Br. J. Radiol.*, 46:1016–1022, 1973.

[53] G. N. Hounsfield. Emi scanner. *Proc. Roy. Soc. London Series B Biol. Sci.*, 195:281–289, 1977.

[54] T. L. Kline and E. L. Ritman. Studying microcirculation with micro-CT. In M. Leahy, editor, *Microcirculation Imaging*, chapter 14, pages 313–348. Wiley-VCH, 2012.

[55] L. A. Feldkamp, S. A. Goldstein, M. A. Parfitt, G. Jesion, and M. Kleerekoper. The direct examination of three-dimensional bone architecture in vitro by computed tomography. *J. Bone and Mineral Res.*, 4(1):3–11, 1989.

[56] C. Sensen and B. Hallgremsson, editors. *Micro-Computed Tomography*, pages 301–318. Springer-Verlag Berlin Heidelberg, Berlin, Germany, 2009.

[57] M. Marxen, M. M. Thornton, C. B. Chiarot, G. Klement, J. Koprivnikar, J. G. Sled, and R. M. Henkelman. Micro-CT scanner performance and considerations for vascular specimen imaging. *Med. Phys.*, 31(2):305–313, 2004.

[58] S. J. Schambach, S. Bag, L. Scholling, C. Groden, and M. A. Brockmann. Application of micro-CT in small animal imaging. *Methods*, 50(1):2–13, 2010.

[59] C. Badea, L. W. Hedlund, and G. A. Johnson. Micro-CT with respiratory and cardiac gating. *Med. Phys.*, 31(12):3324–3329, 2004.

[60] L. A. Feldkamp, L. C. Davis, and J. W. Kress. Practical cone-beam algorithm. *J. Opt. Soc. Am. A*, 1(6):612–619, 1984.

[61] J. S. Kole and F. J. Beekman. Evaluation of accelerated iterative x-ray CT image reconstruction using floating point graphics hardware. *Phys. Med. Biol.*, 51(4):875–889, 2006.

[62] C. L. Duvall, W. Robert Taylor, D. Weiss, and R. E. Guldberg. Quantitative microcomputed tomography analysis of collateral vessel development after ischemic injury. *Am. J. Physiol. Heart Circ. Physiol.*, 287:H302–H310, 2004.

[63] T. L. Kline, Y. Dong, M. Zamir, and E. L. Ritman. Erode/dilate analysis of micro-CT images of porcine myocardial microvasculature. *Proc. SPIE. Med. Imaging 2010*, 7626:762620(1)–762620(9), 2010.

[64] A. C. Langheinrich, A. Michniewicz, D. G. Sedding, G. Walker, P. E. Beighley, W. S. Rau, R. M. Bohle, and E. L. Ritman. Correlation of vasa vasorum neovascularization and plaque progression in aortas of apolipoprotein e-/-/low-density lipoprotein-/-double knockout mice. *Arteriosclerosis, Thrombosis, and Vascular Biology*, 26:347–352, 2006.

[65] T. V. Masyuk, E. L. Ritman, and N. F. LaRusso. Quantitative assessment of the rat intrahepatic biliary system by three-dimensional reconstruction. *Am. J. Path.*, 158:2079–2088, 2001.

[66] X. Y. Zhu, M. Rodriquez-Porcel, M. D. Bentley, A. R. Chade, V. Sica, C. Napoli, N. Caplice, E. L. Ritman, A. Lerman, and L. O. Lerman. Antioxidant intervention attenuates myocardial neovascularization in hypercholesterolemia. *Circulation*, 109:2109–2115, 2004.

[67] S. D. Murad, V. A. L. Dom, E. L. Ritman, P. C. de Groen, P. E. Beighley, S. C. Abraham, P. E. Zondervan, and H. L. A. Janssen. Early changes of the portal tract on microcomputed tomography images in a newly-developed rat model for budd-chiari syndrome. *J. Gastroenterol. Hepatol.*, 23(10):1561–1566, 2008.

[68] B. J. Gannon. Vascular casting. In M. A. Hayat, editor, *Principles and Techniques of Scanning Electron Microscopy*, volume 6, pages 170–193. Van Nostrand Reinhold Company, New York, 1978.

[69] W. L. Mondy, D. Cameron, J.-P. Timmermans, N. D. Clerck, A. Sasov, C. Casteleyn, and L. A Piegl. Micro-CT of corrosion casts for use in the computer-aided design of microvasculature. *Tissue Eng. Part C: Methods*, 15(4):729–738, 2009.

[70] J. Yang, L. X. Yu, M. Y. Rennie, J. G. Sled, and R. M. Henkelman. Comparative structural and hemodynamic analysis of vascular trees. *Am. J. Physiol. Heart Circ. Physiol.*, 298:H1249–H1259, 2010.

[71] S. Mukundan, Jr., K. B. Ghaghada, C. T. Badea, C. Y. Kao, L. W. Hedlund, J. M. Provenzale, G. A. Johnson, E. Chen, R. V. Bellamkonda, and A. Annapraganda. A liposomal nanoscale contrast agent for preclinical CT in mice. *AJR*, 286:300–307, 2006.

[72] W. H. Kong, W. J. Lee, Z. Y. Cui, K. H. Bae, T. G. Park, J. H. Kim, K. Park, and S. W. Seo. Nanoparticulate carrier containing water-insoluble iodinated oil as a multifunctional contrast agent for computed tomography imaging. *Biomaterials*, 28(36):5555–5561, 2007.

[73] R. A. Robb, D. P. Hanson, and M. C. Stacy. Analyze: a comprehensive, operator-interactive software package for multidimensional medical image display and analysis. *Comput. Med. Im. Graph.*, 13(6):433–454, 1989.

[74] J. Lee, P. Beighley, E. Ritman, and N. Smith. Automatic segmentation of 3D micro-CT coronary vascular images. *Med. Image Anal.*, 11(6):630–647, 2007.

[75] S. D. Olabarriaga, M. Breeuwer, and W. J. Niessen. Evaluation of hessian-based filters to enhance the axis of coronary arteries in CT images. *Int. Cong. Series*, 1256:1191–1196, 2003.

[76] T. L. Kline, M. Zamir, and E. L. Ritman. Accuracy of microvascular measurements obtained from micro-CT images. *Ann. Biomed. Eng.*, 38(9):2851–2864, 2010.

[77] M. Marxen, J. G. Sled, L. X. Yu, C. Paget, and R. M. Henkelman. Comparing microsphere deposition and flow modeling in 3d vascular trees. *Am. J. Physiol. Heart Circ. Physiol.*, 291:H2136–H2141, 2006.

[78] T. F. Chan and L. A. Vese. Active contours without edges. *IEEE Trans. Im. Proc.*, 10(2):266–277, 2001.

[79] L. Lam and S. W. Lee. Thinning methodologies – a comprehensive survey. *Patt. Analy. Mach. Int.*, 14:869–885, 1992.

[80] H. Schirmacher, M. Zockler, D. Stalling, and H. C. Hege. Boundary surface shrinking – a continuous approach to 3d center line extraction. In *Im. Multidim. Dig. Sig. Proc.*, pages 25–28. IEEE, 1998.

[81] T. Deschamps and L. D. Cohen. Minimal path in 3d images and application to virtual endoscopy. *ECCV 2000*, 184:543–547, 2000.

[82] R. van Uitert and I. Bitter. Subvoxel precise skeletons of volumetric data based on fast marching methods. *Med. Phys.*, 34:627–637, 2007.

[83] M. Zamir. Mechanics of blood supply to the heart: wave reflection effects in a right coronary artery. *Proc. Biol. Soc.*, 265(1394):439–444, 1998.

[84] H. M. Schaefer, P. E. Beighley, D. R. Eaker, A. J. Vercnocke, and E. L. Ritman. Micro-CT analysis of myocardial blood supply in young and adult rats. *Proc. SPIE*, 7262:726225–1 – 726225–6, 2009.

[85] A. S. Plath, T. L. Kline, D. R. Eaker, P. E. Beighley, A. J. Vercnocke, and E. L. Ritman. Micro-CT analysis of sea sponge pore architecture as a model of a cell-populated synthetic tissue scaffold. *Proc. SPIE*, 7262:72622K–1 – 72622K–5, 2009.

[86] R. C. Gonzalez and R. E. Woods. *Digital Image Processing.* Prentice Hall, New Jersey, 2nd edition, 2002.

[87] R. M. Haralick, S. R. Sternberg, and X. Zhuang. Image analysis using mathematical morphology. *IEEE Trans. Patt. Anal. Mach. Intell.*, PAMI-9:532–550, 1987.

[88] D. Eberly and J. Lancaster. On gray scale image measurements. *CVGIP: Graph. Mod. Im. Proc.*, 53:538–549, 1991.

[89] H. Soltanian-Zadeh, A. Shahrokni, and R. A. Zoroofi. Voxel-coding method for quantification of vascular structure from 3d images. *Proc. SPIE*, 4321:263–270, 2001.

[90] K. R. Hoffman, D. P. Nazareth, L. Miskolczi, A. Gopal, Z. Wang, S. Rudin, and D. R. Bednarek. Vessel size measurements in angiograms: a comparison of techniques. *Med. Phys.*, 29:1622–1633, 2002.

[91] J. B. Bassingthwaighte, J. H. G. M. Van Beek, and R. B. King. Fractal branchings: the basis of myocardial flow heterogeneities. *Ann. NY Acad. Sci.*, 591:392–401, 1990.

[92] A. R. Pries, T. W. Secomb, and P. Gaehtgens. Relationship between structural and hemodynamic heterogeneity in microvascular networks. *Am. J. Physiol. Heart Circ. Physiol.*, 270:H545–H553, 1996.

[93] N. Suwa, T. Takahashi, H. Fukasawa, and Y. Sasaki. Estimation of intravascular blood pressure gradient by mathematical analysis of arterial casts. *Tohoku J. Exp. Med.*, 79:168–198, 1963.

[94] G. Kalsho and G. S. Kassab. Bifurcation asymmetry of the porcine coronary vasculature and its implications on coronary flow heterogeneity. *Am. J. Physiol. Heart. Circ. Physiol*, 287:H2493–H2500, 2004.

[95] G. H. Glover and N. J. Pelc. Nonlinear partial volume artifacts in x-ray computed tomography. *Medical Physics*, 7(3):238–248, 1980.

[96] G. T. Herman. *Image reconstruction from projections : the fundamentals of computerized tomography.* Academic Press, New York, 1980.

[97] M. S. Hassouna and A. A. Farag. On the extraction of curve skeletons using gradient vector flow. *11th IEEE Int. Conf. Comp. Vis.*, 2136:1–8, 2007.

[98] K. C. Yu, E. L. Ritman, and W. E. Higgins. System for the analysis and visualization of large 3d anatomical trees. *Comp. Bio. Med.*, 37:1802–1820, 2007.

[99] T. Wischgoll, J. S. Choy, E. L. Ritman, and G. S. Kassab. Validation of image-based method of extraction of coronary morphometry. *Ann. Biomed. Eng.*, 36:356–358, 2008.

[100] M. Zamir. *The Physics of Coronary Blood Flow*. Springer Science+Business Media Inc., New York, NY, 1st edition, 2005.

[101] M. Zamir and N. Brown. Arterial branching in various parts of the cardiovascular system. *Am. J. Anat.*, 163:295–307, 1982.

[102] V. Megalooikonomou, M. Barnathan, D¿ Kontos, P. R. Bakic, and A. D. A. Maidment. A representation and classification scheme for tree-like structures in medical images: analyszing the branching pattern of ductal trees in x-ray galactograms. *IEEE Trans. Med. Im.*, 28:487–493, 2009.

[103] J. Sethian. *Level Set Methods and Fast Marching Methods: Evolving Interfaces in Computational Geometry, Fluid Mechanics, Computer Vision and Materials Science*. New York, NY: Cambridge University Press, 1999.

[104] G. Peyré and L. Cohen. Landmark-based geodesic computation for heuristically driven path planning. *Proc. IEEE Comp. Vis. Patt. Recogn.*, pages 2229–2236, 2006.

[105] S. Osher and J. Sethian. Fronts propagating with curvature speed: algorithms based on hamilton-jacobi formulations. *J. Comput. Phys.*, 79:12–49, 1988.

[106] E. Rouy and A. Tourin. A viscosity solutions approach to shape-from-shading. *SIAM J. Numer. Anal.*, 29:867–884, 1992.

[107] R. Sedgewick. *Algorithms*. Reading, MA: Addison - Wesley Publishing Company, 1988.

[108] L. D. Cohen and R. Kimmel. Global minimum for active contour models: a minimal path approach. *Int. J. Comp. Vis.*, 24:57–78, 1997.

[109] H. Soltanian-Zadeh, A. Shahrokni, and R. A. Zoroofi. Voxel-coding method for quantification of vascular structure from 3d images. *Proc. SPIE*, 4321:263–270, 2001.

[110] A. S. Popel. Network models of peripheral circulation. chapter 20, pages 20.1–20.24. New York: McGraw-Hill Inc., 1987.

[111] S. T. Witt, C. H. Riedel, M. Goessl, M. S. Chmelik, and E. L. Ritman. Point spread function deconvolution in 3d micro-CT angiography for multiscale vascular tree separation. *Proc. SPIE*, 5030:720–727, 2003.

[112] D. G. Altman and J. M. Bland. Measurement in medicine: the analysis of method comparison studies. *Statistician*, 32:307–313, 1983.

[113] R. Hoogeveen, C. Bakker, and M. Viergever. Limits to the accuracy of vessel diameter measurement in mr angiography. *J. Mag. Res. Im.*, 8:1228–1235, 1998.

[114] Y. Sato, S. Yamamoto, and S. Tamura. Accurate quantification of small-diameter tubular structures in isotropic CT volume data based on multiscale line filter responses. *Proc. MICCAI 04*, 3216:508–515, 2004.

[115] W. B. Lindquist, S. M. Lee, D. A. Coker, K. W. Jones, and P. Spanne. Medial axis analysis of three dimensional tomographic images of drill core samples. *J. Geophys. Res.*, 101B:8297, 1996.

[116] L. Kuo, M. J. Davis, and W. M. Chilian. Endothelial modulation of arteriolar tone. *News Physiol. Sci.*, 7:5–9, 1992.

[117] E. L. Ritman, S. M. Jorgensen, P. E. Lund, P. J. Thomas, and J. H. Dunsmuir. Synchrotron-based micro-CT of in situ biological basic functional units and their integration. *Proc. SPIE Dev. X-Ray Tomogr.*, 3149:13–24, 1997.

[118] T. L. Kline and E. L. Ritman. Paths of least flow-resistance: characterization for the optimization of synthetic tissue scaffold design. *Proc. ISBI 2009*, pages 606–609, 2009.

[119] M. Zamir, P. Sinclair, and T. H. Wannacott. Relation between diameter and flow in major branches of the arch of the aorta. *J. Biomechanics*, 25(11):1303–1310, 1992.

[120] M. Labarbera. The design of fluid transport systems: a comparative perspective. In G. Kaley J.A. Bevan and G.M. Rubanyi, editors, *Flow Dependent Regulation of Vascular Function*, pages 3–27. Oxford University Press, Oxford, 1995.

[121] Alpini, G.D. Heterogeneity of the intrahepatic biliary epithelium. *W. J. Gastroent.*, 12(22):3523–3536, 2006.

[122] D. Lesage, E. D. Angelini, I. Bloch, and G. Funka-Lea. A review of 3d vessel lumen segmentation techniques: Models, features and extraction schemes. *Med. Image Anal.*, 13(6):819–845, 2009.

[123] A. C. Langheinrich, M. Kampschulte, C. Cromann, R. Moritz, W. S. Rau, R. M. Bohle, and E. L. Ritman. Role of computed tomography voxel size in detection and discrimination of calcium and iron deposits in atherosclerotic human coronary artery specimens. *J. Comput. Assist. Tomogr.*, 33(4):517–522, 2009.

[124] E. L. Ritman. Current status of developments and applications of micro-CT. *Annu. Rev. Biomed. Eng.*, 13:531–552, 2011.

[125] C. R. Maurer, R. Qi, and V. Raghavan. A linear time algorithm for computing exact euclidean distance transforms of binary images in arbitrary dimensions. *IEEE Trans. Pattern Anal. Mach. Intell.*, 25(2):265–270, 2003.

[126] C. Xu and J. L. Prince. Snakes, shapes, and gradient vector flow. *IEEE Trans. Image Process.*, 7(3):359–369, 1998.

[127] B. Li and S. T. Acton. Active contour external force using vector field convolution for image segmentation. *IEEE Trans. Image Process.*, 16(8):2096–2007, 2007.

[128] D. Y. Kim and J. W. Park. Connectivity-based local adaptive thresholding for carotid artery segmentation using mra images. *Im. Vis. Comput.*, 23:1277–1287, 2005.

[129] A. F. Frangi, W. J. Niessen, K. L. Vincken, and M. A. Viergever. Multiscale vessel enhancement filtering. *In: Proc. Med. Image Comput. Assist. Interv.*, 1496:130–137, 1998.

[130] X.-Y Zhu, V. Urbieta-Caceres, J. D. Krier, S. C. Textor, A. Lerman, and L. O. Lerman. Mesenchymal stem cells and endothelial progenitor cells decrease renal injury in experimental swine renal artery stenosis through different mechanisms. *Stem Cells*, 31:117–125, 2013.

[131] H. M. Schaefer, P. E. Beighley, D. R. Eaker, A. J. Vercnocke, and E. L. Ritman. Micro-ct analysis of myocardial blood supply in young and adult rats. *Proc. SPIE*, 7262:726225(1)–726225(6), 2009.

[132] X. Tizon and O. Smedby. Segmentation with gray-scale connectedness can separate arteries and veins in mra. *J. Magn. Reson. Imaging*, 15:438–445, 2002.

[133] S. J. Schambach, S. Bag, C. Groden, L. Scholling, and M. A. Brockmann. Vascular imaging in small rodents using micro-CT. *Methods*, 50(1):26–35, 2010.

[134] S. Y. Wan, A. P. Kiraly, E. L. Ritman, and W. E. Higgins. Extraction of the hepatic vasculature in rats using 3d micro-CT images. *IEEE Trans. Med. Imaging*, 19(9):964–971, 2000.

[135] J. H. Waarsing, J. S. Day, J. C. van der Linden, A. G. Ederveen, C. Spanjers, N. De Clerck, A. Sasov, J. A. N. Verhaar, and H. Weinans. Detecting and tracking local changes in the tibiae of individual rats: a novel method to analyse longitudinal in vivo micro-CT data. *Bone*, 34(1):163–169, 2004.

[136] D. Cavanaugh, E. Johnson, R. E. Price, J. Kurie, E. L. Travis, and D. D. Cody. In vivo respiratory-gated micro-CT imaging in small-animal oncology models. *Mol. Im.*, 3(1):55–62, 2004.

[137] E. Namati, D. Chon, J. Thiesse, E. A. Hoffman, J. de Ryk, A. Ross, and G. McLennan. In vivo micro-CT lung imaging via a computer-controlled intermittent iso-pressure breath hold (iibh) technique. *Phys. Med. Biol.*, 51(23):6061–6075, 2006.

[138] N. L. Ford, M. M. Thornton, and D. W. Holdsworth. Fundamental image quality limits for microcomputed tomography in small animals. *Med. Phys.*, 30(11):2869–2877, 2003.

[139] B. E. Nett, R. Brauweiler, W. Kalendar, H. Rowley, and G. H. Chen. Perfusion measurements by micro-CT using prior image constrained compressed sensing (piccs): initial phantom results. *Phys. Med. Biol.*, 55(8):2333–2350, 2010.

Appendix A

Permissions

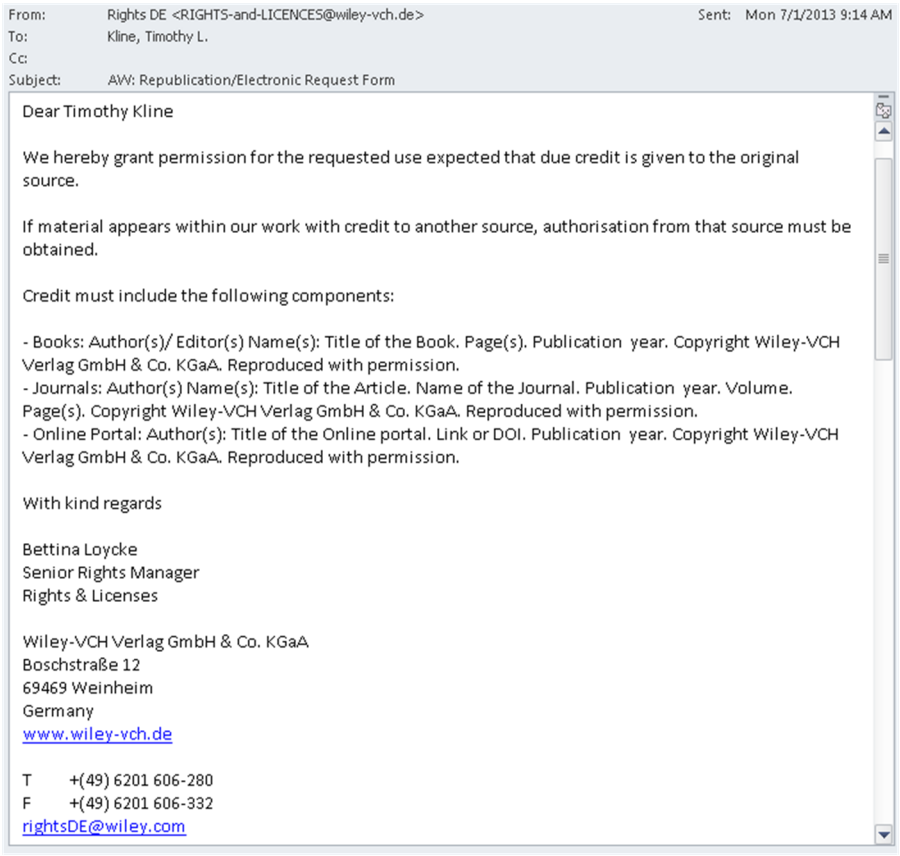

From: Rights DE <RIGHTS-and-LICENCES@wiley-vch.de> Sent: Mon 7/1/2013 9:14 AM
To: Kline, Timothy L.
Cc:
Subject: AW: Republication/Electronic Request Form

Dear Timothy Kline

We hereby grant permission for the requested use expected that due credit is given to the original source.

If material appears within our work with credit to another source, authorisation from that source must be obtained.

Credit must include the following components:

- Books: Author(s)/ Editor(s) Name(s): Title of the Book. Page(s). Publication year. Copyright Wiley-VCH Verlag GmbH & Co. KGaA. Reproduced with permission.
- Journals: Author(s) Name(s): Title of the Article. Name of the Journal. Publication year. Volume. Page(s). Copyright Wiley-VCH Verlag GmbH & Co. KGaA. Reproduced with permission.
- Online Portal: Author(s): Title of the Online portal. Link or DOI. Publication year. Copyright Wiley-VCH Verlag GmbH & Co. KGaA. Reproduced with permission.

With kind regards

Bettina Loycke
Senior Rights Manager
Rights & Licenses

Wiley-VCH Verlag GmbH & Co. KGaA
Boschstraße 12
69469 Weinheim
Germany
www.wiley-vch.de

T +(49) 6201 606-280
F +(49) 6201 606-332
rightsDE@wiley.com

Figure A.1: Permission to reproduce *Microcirculation Imaging* book chapter.

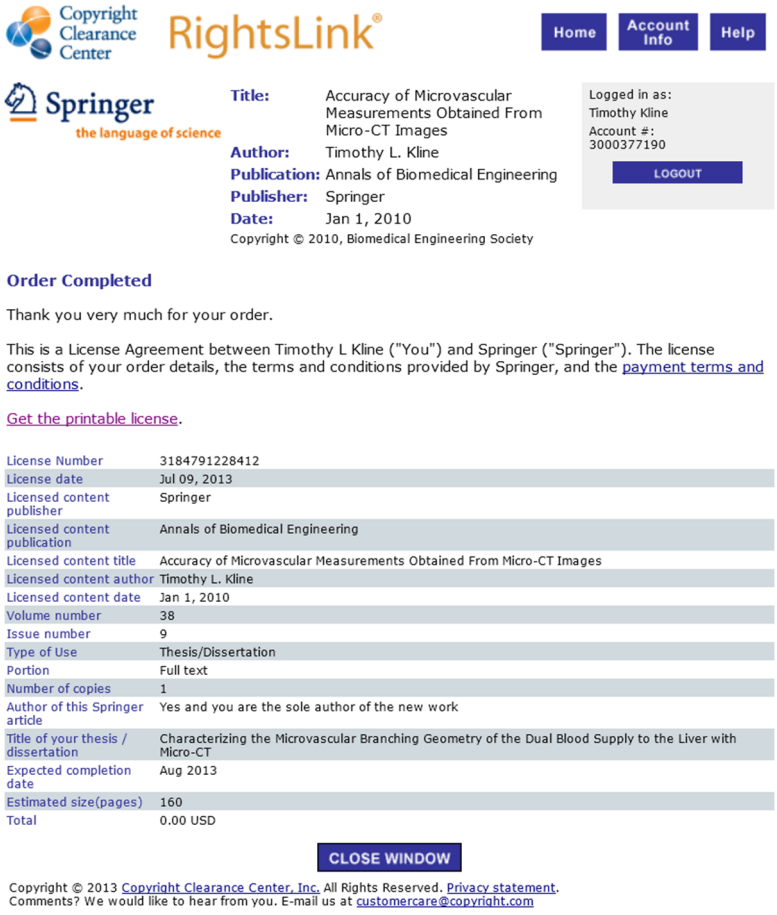

Copyright Clearance Center RightsLink®

Home | Account Info | Help

Springer — the language of science

Title:	Accuracy of Microvascular Measurements Obtained From Micro-CT Images
Author:	Timothy L. Kline
Publication:	Annals of Biomedical Engineering
Publisher:	Springer
Date:	Jan 1, 2010

Copyright © 2010, Biomedical Engineering Society

Logged in as:
Timothy Kline
Account #:
3000377190
LOGOUT

Order Completed

Thank you very much for your order.

This is a License Agreement between Timothy L Kline ("You") and Springer ("Springer"). The license consists of your order details, the terms and conditions provided by Springer, and the payment terms and conditions.

Get the printable license.

License Number	3184791228412
License date	Jul 09, 2013
Licensed content publisher	Springer
Licensed content publication	Annals of Biomedical Engineering
Licensed content title	Accuracy of Microvascular Measurements Obtained From Micro-CT Images
Licensed content author	Timothy L. Kline
Licensed content date	Jan 1, 2010
Volume number	38
Issue number	9
Type of Use	Thesis/Dissertation
Portion	Full text
Number of copies	1
Author of this Springer article	Yes and you are the sole author of the new work
Title of your thesis / dissertation	Characterizing the Microvascular Branching Geometry of the Dual Blood Supply to the Liver with Micro-CT
Expected completion date	Aug 2013
Estimated size(pages)	160
Total	0.00 USD

CLOSE WINDOW

Figure A.2: Permission to reproduce *Annals of Biomedical Engineering* manuscript.

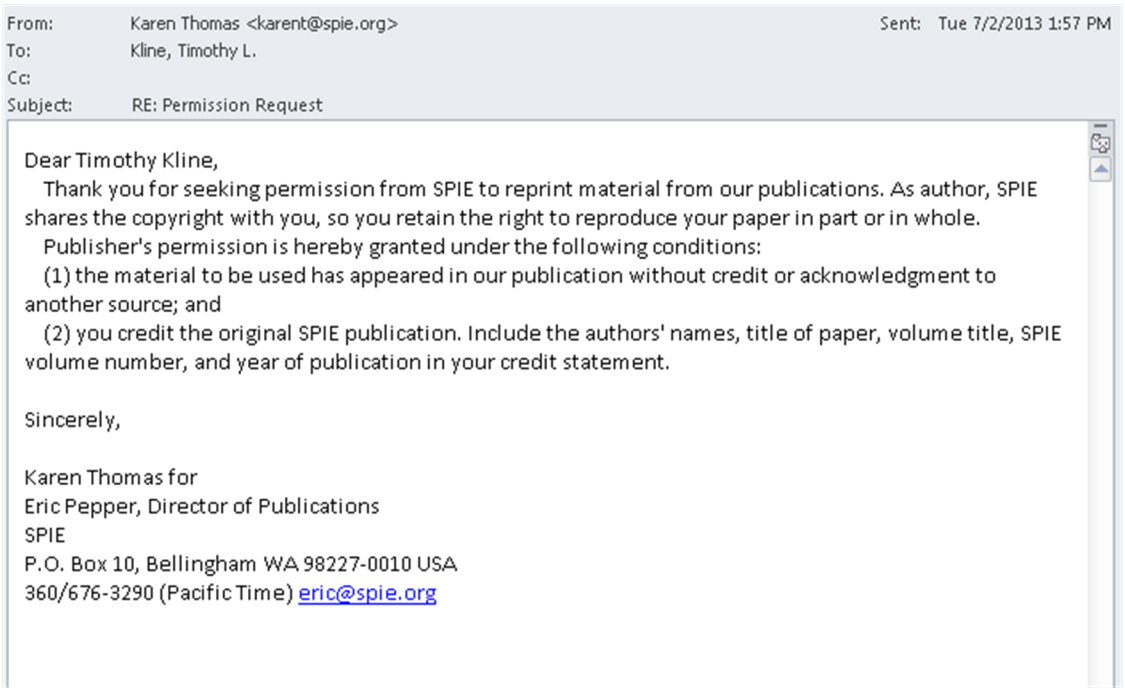

From: Karen Thomas <karent@spie.org> Sent: Tue 7/2/2013 1:57 PM
To: Kline, Timothy L.
Cc:
Subject: RE: Permission Request

Dear Timothy Kline,
Thank you for seeking permission from SPIE to reprint material from our publications. As author, SPIE shares the copyright with you, so you retain the right to reproduce your paper in part or in whole.
Publisher's permission is hereby granted under the following conditions:
(1) the material to be used has appeared in our publication without credit or acknowledgment to another source; and
(2) you credit the original SPIE publication. Include the authors' names, title of paper, volume title, SPIE volume number, and year of publication in your credit statement.

Sincerely,

Karen Thomas for
Eric Pepper, Director of Publications
SPIE
P.O. Box 10, Bellingham WA 98227-0010 USA
360/676-3290 (Pacific Time) eric@spie.org

Figure A.3: Permission to reproduce *SPIE* manuscript.

Customer Information

Customer: Timothy Kline
Account Number: 3000377190
Organization: Timothy Kline
Email: kline.timothy@mayo.edu
Phone: +1 (507)2554199

Search order details by: Choose One Go

Order Details

Cells, tissues, organs

Billing Status: **N/A**

Order detail ID:	63809190
Article Title:	Relating Function to Branching Geometry: A Micro-CT Study of the Hepatic Artery, Portal Vein, and Biliary Tree
Author(s):	Kline, Timothy L. ; Zamir, Mair ; Ritman, Erik L.
DOI:	10.1159/000323482
Date:	Jan 01, 2011
ISSN:	1422-6405
Publication Type:	Journal
Volume:	194
Issue:	5
Start page:	431
Publisher:	S./KARGER AG

Permission Status: **Granted**

Permission type: Republish or display content
Type of use: reuse in a thesis/dissertation
Order License Id: 3178360614441

Hide details

Licensed copyright line	Copyright © 2011, Copyright © 2011, Karger Publishers
Requestor type	author of requested content
Format	Print, Electronic
Portion	figures/tables/illustrations
Number of figures/tables/illustrations	7
Include Image file	no
Rights for	Main product
Duration of use	Life of current edition/presentation
Creation of copies for the disabled	no
With minor editing privileges	yes
For distribution to	Worldwide
Lifetime unit quantity of new product	1
The requesting person/organization	Timothy Lee Kline
Order reference number	
Title of your thesis / dissertation	Characterizing the Microvascular Branching Geometry of the Dual Blood Supply to the Liver with Micro-CT
Expected completion date	Aug 2013
Estimated size (number of pages)	160

Figure A.4: Permission to reproduce *Cells Tissues Organs* manuscript.